

Activity, stability, and degradation mechanisms of platinum and platinum alloy nanoparticle PEM fuel cell electrocatalysts

vorgelegt von
Diplom - Chemiker Frédéric Hasché
aus Berlin

Von der Fakultät II - Mathematik und Naturwissenschaften
der Technischen Universität Berlin
zum Erlangen des akademischen Grades

Doktor der Naturwissenschaften
Dr. rer. nat.

genehmigte Dissertation

Promotionsausschuss:

Vorsitzender:	Prof. Dr. R. Süßmuth	(TU Berlin)
Berichter:	Prof. Dr. P. Strasser	(TU Berlin)
Berichter:	Prof. Dr. T. J. Schmidt	(ETH Zürich)

Tag der wissenschaftlichen Aussprache: 08. Februar 2012

Berlin 2012

D 83

Table of Contents

Table of Contents	2
Table captions	5
Figure captions	7
1 Introduction	17
1.1 Hydrogen PEM fuel cell.....	17
1.2 Hydrogen PEM fuel cell electrocatalyst research targets.....	20
1.2.1 Catalyst activity	20
1.2.2 Catalyst stability	22
1.2.3 Catalyst cost.....	24
1.3 Research goals and strategy.....	25
2 Experimental Part	28
2.1 Synthesis of Pt/MWCNT.....	28
2.2 Synthesis of Pt/meso-BMP	30
2.3 Synthesis of PtCu ₃ /HSAC and PtCo ₃ /HSAC	31
2.4 Synthesis of PtNi ₃ /Vulcan XC 72R	32
2.5 Structure and composition characterization	33
2.5.1 X-Ray diffraction (XRD) measurement in Bragg-Brentano geometry	33
2.5.2 In situ high temperature X-ray diffraction (HT-XRD) measurements in parallel beam geometry	34
2.5.3 Transmission electron microscopy (TEM) measurements.....	38
2.5.4 Energy dispersion X-ray spectroscopy (EDS) measurements.....	39
2.5.5 Brunauer-Emmett-Teller (BET) surface area measurements	40
2.6 Electrochemical characterization using rotating disk electrode (RDE)	41
2.6.1 Preparation of catalytic active thin film electrodes.....	41
2.6.2 Rotating disk electrode (RDE) setup	42
2.6.3 Activity for the oxygen reduction reaction (ORR) using linear sweep voltammetry (LSV).....	43

2.6.4	Platinum electrochemical active surface area (ECSA) using cyclic voltammetry (CV)	44
2.6.5	Electrochemical long-term durability experiments	45
2.6.6	Electrochemical dealloying procedure	46
3	Activity, stability, and degradation of Pt fuel cell electrocatalysts: support effects	47
3.1	Multi walled carbon nanotube (MWCNT) supported Pt fuel cell electrocatalyst	48
3.1.1	Structural characterization of carbon supported Pt nanoparticles	49
3.1.2	Stability of Pt/MWCNT in the „lifetime“ and „start-up“ potential cycling regimes.....	51
3.1.3	Activity of Pt/MWCNT in „lifetime“ and „start-up“ potential regimes.....	53
3.1.4	Correlation of particle growth and ECSA loss mechanisms.....	56
3.1.5	Conclusions.....	62
3.2	Mesoporous nitrogen doped carbon (meso-BMP) supported Pt fuel cell electrocatalyst	63
3.2.1	Synthesis and structural characterization of Pt/meso-BMP	64
3.2.2	Activity and selectivity of Pt/meso-BMP for oxygen reduction	66
3.2.3	Stability of Pt/meso-BMP during voltage cycling	69
3.2.4	Conclusions.....	71
3.3	Silicon carbide derived carbon (CDC) supported Pt fuel cell electrocatalyst	72
3.3.1	Structural characterization of Pt/CDC.....	73
3.3.2	Activity and selectivity of Pt/CDC for oxygen reduction	75
3.3.3	Conclusions.....	79
3.4	Overview – support effects.....	80
4	Activity, stability, and degradation of Pt alloy fuel cell electrocatalysts: catalytically active component	83
4.1	Activity, stability, and degradation mechanisms of dealloyed PtCu₃ and PtCo₃ nanoparticle fuel cell catalysts	84
4.1.1	Structural characterization of PtCu ₃ , PtCo ₃ and Pt nanoparticles.....	85

4.1.2	Activity and stability of Pt and Pt alloy nanoparticle catalysts in “lifetime” and “start-up” voltage cycling regimes.....	87
4.1.3	Particle growth and platinum ECSA loss mechanisms	91
4.1.4	Conclusions.....	101
4.2	Activity, structure and degradation of dealloyed PtNi₃ nanoparticle fuel cell electrocatalyst.....	103
4.2.1	Structural and compositional characterization of as synthesized PtNi ₃ alloy catalyst.....	104
4.2.2	Electrochemical characterization of dealloyed PtNi ₃ nanoparticle catalyst	105
4.2.3	ORR activities of dealloyed PtNi ₃ nanoparticle catalyst.....	109
4.2.4	Durability of dealloyed PtNi ₃ nanoparticle catalyst	111
4.2.5	Conclusions.....	119
5	Thermal stability of supported platinum nanoparticle catalysts: in situ studies.....	120
5.1	Crystallite growth rate in dependence on BET surface area and treatment temperature	122
5.2	Crystallite growth rate in dependence on the platinum loading	129
5.3	Effects of the temperature and the interparticle distance	130
5.4	Crystallite growth rate in dependence on the gas phase environment.....	133
5.5	Conclusions.....	135
6	Conclusions and Perspectives	136
7	Appendix	141
7.1	Materials and chemicals	141
7.2	Abbreviations and symbols.....	142
7.3	Model for the calculation of the interparticle distance (λ)	144
7.4	Criteria of fit for XRD profiles.....	145
8	References	146

Table captions

Table 1 Catalyst mixture recipes for thin film electrode preparation.....	41
Table 2 Catalyst performance – 10,000 voltage cycles from 0.5 to 1.0 V vs. RHE. Reproduced from reference ⁵² by permission of The Royal Society of Chemistry.	53
Table 3 Catalyst performance – 2000 voltage cycles from 0.5 to 1.5 V vs. RHE. Reproduced from reference ⁵² by permission of The Royal Society of Chemistry.	53
Table 4 Comparison of as synthesized mean particle size, Pt mass and Pt surface area specific based ORR activities for Pt/meso-BMP and Pt/HSAC nanoparticle catalysts. Reproduced from reference ⁶⁴ by permission of John Wiley and Sons.	68
Table 5 ORR catalyst performance. Reproduced from reference ⁶² by permission of Elsevier.	76
Table 6 Overview of supported Pt nanoparticle catalysts: Pt loading, Pt mass based (j_{mass}) and Pt surface area specific (j_{specific}) based ORR activities, Pt electrochemical active surface area (ECSA) and mean particle size determined by TEM.	81
Table 7 Overview: Pt loading, ECSA loss and final particle size of supported Pt nanoparticle catalysts after „lifetime“ stability testing.....	82
Table 8 Mean particle size and chemical composition for Pt/HSAC, PtCu ₃ /HSAC and PtCo ₃ /HSAC catalysts before and after electrochemical stability testing. Reproduced from reference ³⁶ by permission of John Wiley and Sons.	86
Table 9 ORR activities for Pt/HSAC, PtCu ₃ /HSAC and PtCo ₃ /HSAC catalysts before and after electrochemical stability testing. Reproduced from reference ³⁶ by permission of John Wiley and Sons.	88
Table 10 Platinum electrochemical active surface area (ECSA) for Pt/HSAC, PtCu ₃ /HSAC and PtCo ₃ /HSAC catalysts before and after electrochemical stability testing. Reproduced from reference ³⁶ by permission of John Wiley and Sons.	94

Table captions

- Table 11 Comparison of mean particle size of the as synthesized and the ORR activities of dealloyed PtNi₃/Vulcan XC 72R, Pt/Vulcan XC 72R (HT) and Pt/Vulcan XC 72R nanoparticle catalysts. Reproduced from reference ¹⁰⁴ by permission of ECS – The Electrochemical Society... 110
- Table 12 Correlation of mean particle size and Pt electrochemical active surface area (ECSA) for PtNi₃/Vulcan XC 72 R, commercial pure Pt/Vulcan XC 72R, and heat treated Pt/Vulcan XC 72R (HT) after dealloying, “lifetime” (10000 voltage cycles, 0.5 – 1.0 V vs. RHE, 50 mV s⁻¹), and “start-up” (2000 voltage cycles, 0.5 – 1.5 V vs. RHE, 50 mV s⁻¹) stability testings. Reproduced from reference ¹⁰⁴ by permission of ECS – The Electrochemical Society. 114
- Table 13 Various Pt loadings and BET surface areas of Pt nanoparticle catalysts. Reproduced from reference ¹²⁶ by permission of John Wiley and Sons. 121
- Table 14 Mean crystallite size of platinum for different Pt/C materials before and after thermal treatment at 80°C and 160°C for 155 hours under N₂ atmosphere and the interparticle distances (λ). Reproduced from reference ¹²⁶ by permission of John Wiley and Sons..... 129
- Table 15 Criteria of fit using TOPAS. The observed and calculated data at data point are denoted with $Y_{o,m}$ and $Y_{c,m}$ respectively. M is the number of data points and P the number of parameters. w_m the weighting given to data point m which for counting statistics is given by $w_m = 1/\sigma(Y_{o,m})^2$ where $\sigma(Y_{o,m})$ is the error in $Y_{o,m}$ and $I_{o,k}$ and $I_{c,k}$ the “observed” and calculated intensities of the kth reflection. 145

Figure captions

Figure 1 Schematic of a single cell (membrane electrode assembly, MEA) hydrogen / oxygen PEM fuel cell.....	17
Figure 2 Reaction mechanism of oxygen on Pt or Pt alloy nanoparticle catalysts.	18
Figure 3 Hydrogen PEM fuel cell research goals.* = 6	20
Figure 4 Degradation processes of Pt nanoparticles on carbon support.....	22
Figure 5 Material cost reducing by core – shell structure, a) global view, b) detail view.	24
Figure 6 PEM fuel cell catalyst testing and development: topics and agenda...	25
Figure 7 Synthesis strategy – wet impregnation / freeze-drying / furnace reduction.	28
Figure 8 Overview tube furnace setup.	29
Figure 9 Temperature – time profile for the synthesis of Pt/MWCNT. RT: room temperature, H ₂ /Ar: 6 Vol.% H ₂ (5.0) / 94 Vol.% Ar (5.0), O ₂ /N ₂ : 1 Vol.% O ₂ (4.5) / 99 Vol.% N ₂ (5.0).....	29
Figure 10 X-ray diffractometer setup in Bragg-Brentano geometry.....	33
Figure 11 High temperature X-ray diffractometer (HT-XRD) setup in parallel beam geometry, a) overview, b) detail view heating chamber, c) Al ₂ O ₃ crucible with sample.....	34
Figure 12 Alignment of the HT-XRD. Left side: Schematic sketch of the “Z drive”. Right side: Series of XRD patterns at various values of Z height recorded by a direct beam and PSD fix scan. The optimal Z height is only achieved, when the intensity is the half of the maximum intensity. XRD parameters: $\Theta = -0.5$ to $+0.5^\circ$ for the X-ray tube, step size of 0.02° and holding time 1 s.....	36
Figure 13 Calibration of the thermocouple by temperature-dependent XRD measurements from α -quartz (trigonal) to β -quartz (hexagonal). a) Series of XRD patterns at various temperatures in the range of 552 °C to 595 °C. b) Three-dimension representation of the phase transformation of α -quartz to β -quartz. XRD parameters: $2\Theta = 25.5$ to 28° , step size of 0.01° and holding time of 2 s.	37

Figure captions

Figure 14 Transmission electron microscope (TEM) setup, a) overview TEM, b) sample holder, c-d) TEM grid with holey carbon film, e) sample suspension.....	38
Figure 15 BET sample cell.....	40
Figure 16 Preparation of the working electrode.	41
Figure 17 Rotating disk electrode (RDE) setup, a) detail view, b) overview.....	42
Figure 18 Analysis of a linear sweep voltammogram (Pt/C, 0.06 – 1.00 V vs. RHE, 5 mV s ⁻¹ , 1600 rpm, sat. O ₂ , 0.1 M HClO ₄ , room temperature).	43
Figure 19 Analysis of a cyclic voltammogram (Pt/C, 0.06 – 1.00 V vs. RHE, 100 mV s ⁻¹ , sat. N ₂ , 0.1 M HClO ₄ , room temperature).....	44
Figure 20 Voltage cycling in the “lifetime” stability test regime.....	45
Figure 21 Voltage cycling in the “start-up” stability test regime.	45
Figure 22 XRD for commercial Pt/Vulcan XC 72R and self made Pt/MWCNT. PDF(Pt)#00-004-0802, PDF(Graphite)#01-075-1621. Reproduced from reference ⁵² by permission of The Royal Society of Chemistry. .	49
Figure 23 TEM images for Pt/MWCNT after synthesis, a) 100 nm scale, b) 5 nm scale and commercial Pt/Vulcan XC 72R, c) 100 nm scale, d) 10 nm scale. Reproduced from reference ⁵² by permission of The Royal Society of Chemistry.	51
Figure 24 Normalized ECSA loss due to voltage cycling from 0.5 - 1.0 V vs. RHE (solid symbols) and 0.5 - 1.5 V vs. RHE (hollow symbols) with 50 mV s ⁻¹ for Pt/MWCNT (square) and commercial Pt/Vulcan XC 72R (circular). Reproduced from reference ⁵² by permission of The Royal Society of Chemistry.	52
Figure 25 CV for a) Pt/MWCNT, c) Pt/Vulcan XC 72R and LSV for b) Pt/MWCNT, d) Pt/Vulcan XC 72R, 10,000 cycles from 0.5 - 1.0 V vs. RHE with 50 mV s ⁻¹ (initial – black, final – red). Reproduced from reference ⁵² by permission of The Royal Society of Chemistry.	54
Figure 26 Tafel Plot before (solid symbols) and after (hollow symbols) 10,000 cycles from 0.5 - 1.0 V vs. RHE with 50 mV s ⁻¹ for Pt/MWCNT (square) and commercial Pt/Vulcan XC 72R (circular). Reproduced from reference ⁵² by permission of The Royal Society of Chemistry.	54

Figure 27 CV for a) Pt/MWCNT, c) Pt/Vulcan XC 72R and LSV for b) Pt/MWCNT, d) Pt/Vulcan XC 72R, 2000 cycles from 0.5 - 1.5 V vs. RHE with 50 mV s^{-1} (initial – black, final – red). Reproduced from reference ⁵² by permission of The Royal Society of Chemistry.55

Figure 28 Tafel Plot before (solid symbols) and after (hollow symbols) 2000 cycles from 0.5 - 1.5 V vs. RHE with 50 mV s^{-1} for Pt/MWCNT (square) and commercial Pt/Vulcan XC 72R (circular). Reproduced from reference ⁵² by permission of The Royal Society of Chemistry.56

Figure 29 Histograms of particle size distribution for Pt/Vulcan XC 72R before and after electrochemical stability testing (2000 cycles from 0.5 - 1.5 V vs. RHE with 50 mV s^{-1} , 10,000 cycles from 0.5 - 1.0 V vs. RHE with 50 mV s^{-1}). The bar charts are shown with x-offset. Reproduced from reference ⁵² by permission of The Royal Society of Chemistry.57

Figure 30 Histograms of particle size distribution for Pt/MWCNT before and after electrochemical stability testing (2000 cycles from 0.5 - 1.5 V vs. RHE with 50 mV s^{-1} , 10,000 cycles from 0.5 - 1.0 V vs. RHE with 50 mV s^{-1}). The bar charts are shown with x-offset. Reproduced from reference ⁵² by permission of The Royal Society of Chemistry.58

Figure 31 Pt migration within multi walled carbon nanotube – TEM image for Pt/MWCNT after electrochemical “lifetime” potential cycling (0.5 - 1.0 V vs. RHE, 10,000 cycles). a) bright field TEM (10 nm scale), b) dark field TEM (20 nm scale). Reproduced from reference ⁵² by permission of The Royal Society of Chemistry.59

Figure 32 TEM image for commercial Pt/Vulcan XC 72R after electrochemical a) “lifetime” potential cycling (0.5 - 1.0 V vs. RHE, 10,000 cycles, 10 nm scale) and b) “start-up” potential cycling (0.5 - 1.5 V vs. RHE, 2000 cycles, 10 nm scale). Reproduced from reference ⁵² by permission of The Royal Society of Chemistry.60

Figure 33 Synthesis route for mesoporous nitrogen doped carbon supported platinum nanoparticle catalyst. Reproduced from reference ⁶⁴ by permission of John Wiley and Sons.64

Figure 34 XRD profiles of the meso-BMP support material (top) and Pt/meso-BMP catalyst (bottom) with a Rietveld refinement fit (thin red line). Vertical dotted lines denote reference powder diffraction patterns of pure fcc Pt, PDF(Pt)#00-004-0802⁸⁷. Reproduced from reference ⁶⁴ by permission of John Wiley and Sons.65

Figure 35 TEM images for the as synthesized Pt/meso-BMP, a) 0.2 μm bar scale, b) 10 nm bar scale. Reproduced from reference ⁶⁴ by permission of John Wiley and Sons.66

Figure 36 Electrochemical characterization of Pt/meso-BMP, a) polarization curves at various rotation speeds in oxygenated 0.1 M HClO₄, b) Koutecky – Levich plot for oxygen reduction at various voltages. Reproduced from reference ⁶⁴ by permission of John Wiley and Sons.68

Figure 37 Evolution of the platinum electrochemical active surface area (ECSA) (inset: normalized ECSA trend) for Pt/meso-BMP (red squares) and Pt/HSAC (black circles) during voltage cycling from 0.5 to 1.0 V vs. RHE with 50 mV s⁻¹ in deaerated 0.1 M HClO₄ electrolyte at room temperature. Reproduced from reference ⁶⁴ by permission of John Wiley and Sons.69

Figure 38 TEM image for Pt/CDC catalyst (a) 50 nm scale, (c) 10 nm scale and commercial Pt/Vulcan XC 72R catalyst (b) 50 nm scale, (d) 10 nm scale. Reproduced from reference ⁶² by permission of Elsevier.....74

Figure 39 Electrochemical characterization for Pt/CDC catalyst, linear sweep voltammetry (LSV) with different rotating speeds performed anodically from 0.06 - 1.03 V vs. RHE with 5 mV s⁻¹ in oxygen saturated 0.1 M HClO₄ at room temperature, inset) cyclic voltammetry (CV) conducted from 0.06 - 1.00 V vs. RHE with 100 mV s⁻¹ in deaerated 0.1 M HClO₄ at room temperature. Reproduced from reference ⁶² by permission of Elsevier.75

Figure 40 Koutecky - Levich plot for Pt/CDC catalyst at various potentials, data taken from Figure 39. Reproduced from reference ⁶² by permission of Elsevier.77

Figure 41 Overview of TEM images of supported Pt nanoparticle catalysts.80

Figure 42 Overview of XRD profiles of supported Pt nanoparticle catalysts.81

Figure 43 XRD profiles for (a) PtCo₃/HSAC catalyst, (b) PtCu₃/HSAC catalyst and (c) pure Pt/HSAC catalyst. Vertical dotted lines denote reference powder diffraction patterns (PDF) of pure fcc Pt (black), Cu (red) and Co (blue). PDF(Pt)#00-004-0802, PDF(Cu)#00-004-0836, PDF(Co)#00-015-0806⁸⁷. Reproduced from reference ³⁶ by permission of John Wiley and Sons.85

Figure 44 Platinum surface area specific activity based Tafel Plot for PtCo₃/HSAC (blue square), PtCu₃/HSAC (red circular) and Pt/HSAC (black triangle) catalysts before (solid symbols) and after (hollow symbols) 10,000 voltage cycles from 0.5 – 1.0 V vs. RHE with 50 mV s⁻¹ in 0.1 M HClO₄. Reproduced from reference ³⁶ by permission of John Wiley and Sons.88

Figure 45 Platinum surface area specific activity based Tafel Plot for PtCo₃/HSAC (blue square), PtCu₃/HSAC (red circular) and Pt/HSAC (black triangle) catalysts before (solid symbols) and after (hollow symbols) 2,000 voltage cycles from 0.5 – 1.5 V vs. RHE with 50 mV s⁻¹ in 0.1 M HClO₄. Reproduced from reference ³⁶ by permission of John Wiley and Sons.90

Figure 46 Evolution of the particle size distributions and the according TEM images (scale bar of 10 nm) for Pt/HSAC nanoparticle catalyst (a) as synthesized, (b) after 2,000 voltage cycles from 0.5 – 1.5 V vs. RHE and (c) after 10,000 voltage cycles from 0.5 – 1.0 V vs. RHE with 50 mV s⁻¹ in 0.1 M HClO₄. The bar charts are shown with x-offset. Reproduced from reference ³⁶ by permission of John Wiley and Sons.92

Figure 47 Evolution of the particle size distributions and the according TEM images (scale bar of 10 nm) for PtCu₃/HSAC nanoparticle catalyst (a) as synthesized, (b) after 2,000 voltage cycles from 0.5 – 1.5 V vs. RHE and (c) after 10,000 voltage cycles from 0.5 – 1.0 V vs. RHE with 50 mV s⁻¹ in 0.1 M HClO₄. The bar charts are shown with x-offset. Reproduced from reference ³⁶ by permission of John Wiley and Sons.93

- Figure 48 Evolution of the particle size distributions and the according TEM images (scale bar of 10 nm) for PtCo₃/HSAC nanoparticle catalyst (a) as synthesized, (b) after 2,000 voltage cycles from 0.5 – 1.5 V vs. RHE and (c) after 10,000 voltage cycles from 0.5 – 1.0 V vs. RHE with 50 mV s⁻¹ in 0.1 M HClO₄. The bar charts are shown with x-offset. Reproduced from reference ³⁶ by permission of John Wiley and Sons.93
- Figure 49 Evolution of the normalized platinum electrochemical active surface area (N-ECSA) loss for PtCo₃/HSAC (blue square), PtCu₃/HSAC (red circular) and Pt/HSAC (black triangle) catalysts due to the voltage cycling from 0.5 – 1.0 V vs. RHE (solid symbols) and from 0.5 – 1.5 V vs. RHE (hollow symbols) with 50 mV s⁻¹ in 0.1 M HClO₄. N-ECSA (cycle#) = ECSA (cycle#) / ECSA (initial) * 100%. Reproduced from reference ³⁶ by permission of John Wiley and Sons.....96
- Figure 50 Illustration of dominant ECSA loss mechanisms along the life cycle of carbon supported Pt, Pt-Cu and Pt-Co alloy catalysts. Particle growth up to a quasi-stable critical diameter, D_{critical}, is followed by a degradation regime dominated by support corrosion associated with particle detachment. Continued metal dissolution is likely at the extremely corrosive upper electrode voltages of the “start-up” regime. Reproduced from reference ³⁶ by permission of John Wiley and Sons.99
- Figure 51 XRD profiles of the as synthesized PtNi₃/Vulcan XC 72R catalyst and pure Pt/Vulcan XC 72R catalyst, shown with y-offset. The thin black line indicates the Rietveld refinement fit of PtNi₃/Vulcan XC 72R (R_{wp} = 3.50, R_{exp} = 0.55, GOF = 6.33). Vertical lines denote reference powder diffraction patterns of pure fcc Pt (black, dashed lines) and Ni (blue, dotted points). PDF(Pt)#00-004-0802, PDF(Ni)#00-004-0850⁸⁷. Reproduced from reference ¹⁰⁴ by permission of ECS – The Electrochemical Society. 104

- Figure 52 Cyclic voltammogram profiles of (a) PtNi₃/Vulcan XC 72R for the first scan (red), second scan (blue) and after dealloying (black); (b) comparison of dealloyed PtNi₃/Vulcan XC 72R (black) with Pt/Vulcan XC 72R (HT) (red). CV: 0.06 – 1.00 V vs. RHE, 100 mV s⁻¹ in deaerated 0.1 M HClO₄ at room temperature. Reproduced from reference ¹⁰⁴ by permission of ECS – The Electrochemical Society. 106
- Figure 53 TEM images (scale bar of 10 nm) of PtNi₃/Vulcan XC 72R, (a) as synthesized and (b) after electrochemical dealloying procedure. Reproduced from reference ¹⁰⁴ by permission of ECS – The Electrochemical Society. 108
- Figure 54 Evolution of the particle size distributions for PtNi₃/Vulcan XC 72R, as synthesized and after dealloying. The bar charts are shown with x-offset. Reproduced from reference ¹⁰⁴ by permission of ECS – The Electrochemical Society. 108
- Figure 55 Polarization curves of dealloyed PtNi₃/Vulcan XC 72R at various rotating speeds in oxygenated 0.1 M HClO₄ at room temperature; inset: Koutecky – Levich Plot at various electrode voltages. Reproduced from reference ¹⁰⁴ by permission of ECS – The Electrochemical Society. 109
- Figure 56 Comparison of the Pt surface area specific based activities (*j*_{specific}) at 0.9 V vs. RHE for dealloyed PtNi₃/Vulcan XC 72R, Pt/Vulcan XC 72R (HT), and Pt/Vulcan XC 72R after dealloying, after 10000 voltage cycles (0.5 – 1.0 V vs. RHE, 50 mV s⁻¹), and after 2000 voltage cycles (0.5 – 1.5 v vs. RHE, 50 mV s⁻¹). Reproduced from reference ¹⁰⁴ by permission of ECS – The Electrochemical Society. 112
- Figure 57 Comparison of Pt electrochemical active surface area (ECSA) for dealloyed PtNi₃/Vulcan XC 72 R (red squares), commercial pure Pt/Vulcan XC 72R (blue circulars), and heat treated Pt/Vulcan XC 72R (HT) (black triangles) combined with the initial (left side) and final (right side) mean particle sizes during the “lifetime” voltage cycling (0.5 – 1.0 V vs. RHE, 50 mV s⁻¹, 0.1 M HClO₄, room temperature). Reproduced from reference ¹⁰⁴ by permission of ECS – The Electrochemical Society. 113

- Figure 58 Comparison of Pt electrochemical active surface area (ECSA) for dealloyed PtNi₃/Vulcan XC 72 R (red squares), commercial pure Pt/Vulcan XC 72R (blue circulars), and heat treated Pt/Vulcan XC 72R (HT) (black triangles) combined with the initial (left side) and final (right side) mean particle sizes during the “start-up” voltage cycling (0.5 – 1.5 V vs. RHE, 50 mV s⁻¹, 0.1 M HClO₄, room temperature). Reproduced from reference ¹⁰⁴ by permission of ECS – The Electrochemical Society. 115
- Figure 59 Evolution of the particle size distributions for PtNi₃/Vulcan XC 72R, commercial pure Pt/Vulcan XC 72R, and heat treated Pt/Vulcan XC 72R (HT) as synthesized, after 10000 “lifetime” voltage cycles (0.5 – 1.0 V vs. RHE, 50 mV s⁻¹), and after 2000 “start-up” voltage cycles (0.5 – 1.5 V vs. RHE, 50 mV s⁻¹) experiments. The bar charts are shown with x-offset. Reproduced from reference ¹⁰⁴ by permission of ECS – The Electrochemical Society..... 118
- Figure 60 Series of time resolved XRD profiles for Pt(46 wt.)/Vulcan XC 72R nanoparticle catalyst during the thermal treatment at 160 °C for 155 hours in N₂ atmosphere. Scan #1 was measured at 30 °C and the scan numbers correlate with Figure 2. Vertical dotted lines denote reference powder diffraction pattern (PDF) of pure fcc Pt, PDF(Pt)#00-004-0802⁸⁷. Reproduced from reference ¹²⁶ by permission of John Wiley and Sons. 122
- Figure 61 Mean crystallite size of platinum versus holding time at 80 °C (black squares) and 160 °C (red circles) for Pt(46 wt.)/Vulcan XC 72R nanoparticle catalyst in N₂ atmosphere. The initial mean crystallite size was determined at 30 °C. The scan numbers correlate with XRD profiles in Figure 60. Reproduced from reference ¹²⁶ by permission of John Wiley and Sons. 123
- Figure 62 Mean crystallite size of platinum versus holding time at 80 °C (black squares) and 160 °C (red circles) for Pt(46 wt.)/HSAC nanoparticle catalyst under N₂ atmosphere. The initial mean crystallite size was determined at 30 °C. Reproduced from reference ¹²⁶ by permission of John Wiley and Sons. 124

- Figure 63 Mean crystallite size of platinum versus holding time at 160 °C for Pt(46 wt. %)/Vulcan XC 72R (red circles) and Pt(46 wt. %)/HSAC (black squares) nanoparticle catalysts under N₂ atmosphere. The initial mean crystallite size was determined at 30 °C. Reproduced from reference ¹²⁶ by permission of John Wiley and Sons. 125
- Figure 64 Top: TEM grid versus catalyst sample setup. Bottom: HT-XRD heating chamber setup with Al₂O₃ crucible with catalyst sample (left side) and TEM grid (right side). Reproduced from reference ¹²⁶ by permission of John Wiley and Sons. 126
- Figure 65 TEM images and mean particle sizes ($d_{avg.}$) for Pt(46wt. %)/Vulcan XC 72R (scale bar of 5 nm) nanoparticle catalyst after thermal treatment at 160 °C in N₂ atmosphere, corresponding to Figure 66. Reproduced from reference ¹²⁶ by permission of John Wiley and Sons. 127
- Figure 66 Evolution of the normalized size growth versus holding time at 160 °C for Pt(46 wt. %)/Vulcan XC 72R established by in situ HT-XRD (black squares) and ex situ TEM (red circles) experiments. Reproduced from reference ¹²⁶ by permission of John Wiley and Sons. 128
- Figure 67 Dependence of the Pt loading with 46 wt. % (red circles), 20 wt. % (black squares), and 10 wt. % (blue, triangles) for Pt/Vulcan XC 72R on the mean crystallite size growth during the holding time at 160 °C under N₂ atmosphere. The initial mean crystallite size for each catalyst was determined at 30 °C. Reproduced from reference ¹²⁶ by permission of John Wiley and Sons. 129
- Figure 68 Model for the calculation of the interparticle distance (λ) between two particles. Spherical particles are assumed to be distributed homogeneously on carbon support. Reproduced from reference ¹²⁶ by permission of John Wiley and Sons. 130

Figure 69 Relative change in crystallite size after thermal treatment at 160 °C in nitrogen atmosphere after 155 hours versus the interparticle distance (λ) for various carbon supported Pt nanoparticle materials. λ represents the ideal distance between the nanoparticles on the support surface. Reproduced from reference ¹²⁶ by permission of John Wiley and Sons. 131

Figure 70 Illustration of Pt particle growth in dependence on BET surface area with similar metal loading and initial size. (a) lower and (b) higher BET surface area. The interparticle distance of the nanoparticles (λ) increases with increasing BET surface area. Reproduced from reference ¹²⁶ by permission of John Wiley and Sons. 132

Figure 71 Mean crystallite size of platinum versus thermal treatment time under pure N₂ (red circles) and synthetic air (black squares) atmosphere at 160 °C for Pt(46 wt.)/Vulcan XC 72R. The initial mean crystallite size was determined at 30 °C. Reproduced from reference ¹²⁶ by permission of John Wiley and Sons. 133

Figure 72 Histograms of particle size distributions for Pt(46 wt.)/HSAC nanoparticle catalyst with x-offset. Black solid bar – initial, red hollow dashed bar – after thermal treatment at 160 °C for 190 hours under N₂ atmosphere and blue hollow crossed bar – after thermal treatment at 160 °C for 190 hours under synthetic air atmosphere. Reproduced from reference ¹²⁶ by permission of John Wiley and Sons. 134

1 Introduction

1.1 Hydrogen PEM fuel cell

The development of highly active oxygen reduction electrocatalysts with enhanced durability remains still to be a critical challenge for a wider commercialization of hydrogen proton exchange membrane fuel cells (PEMFCs). The hydrogen proton exchange membrane fuel cell converts chemical Gibbs free energy directly into electrical energy with the single product of water. It is one of the promising technologies for low emission and noise energy production in different fields, for example in automotive or portable applications. The overall reaction of a hydrogen / oxygen PEM fuel cell is



Figure 1 shows a schematic of a single cell (membrane electrode assembly, MEA) hydrogen / oxygen PEM fuel cell.

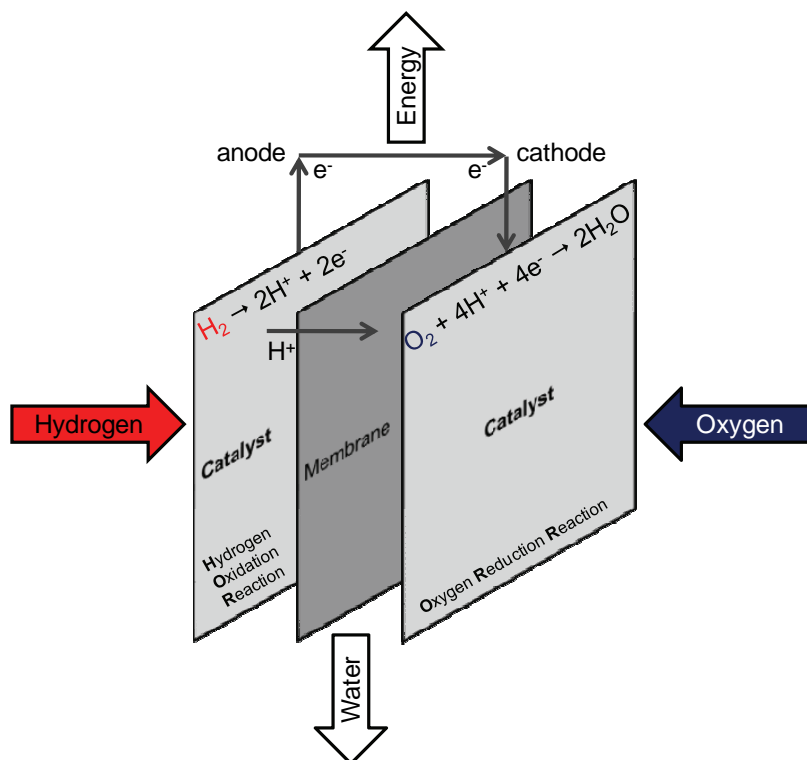


Figure 1 Schematic of a single cell (membrane electrode assembly, MEA) hydrogen / oxygen PEM fuel cell.

The oxygen reacts on the cathode side of the PEMFC with protons and electrons to form water according to the half-cell redox process



where the protons are supplied by the hydrogen splitting on the anodic side via membrane crossing^{1, 2}. This oxygen reduction reaction (ORR) on the cathodic side is a sluggish rate limiting reaction and therefore leads to significant cell voltage and overall efficiency losses in a PEMFC^{3, 4}.

The reaction mechanism of oxygen on Pt or Pt alloy nanoparticle catalysts is shown in Figure 2¹.

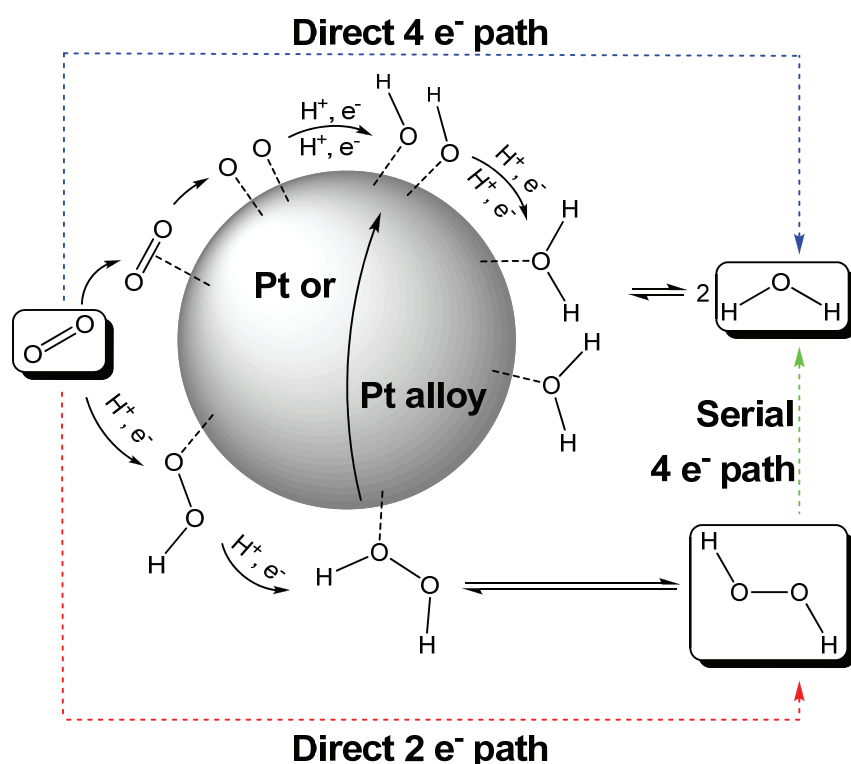
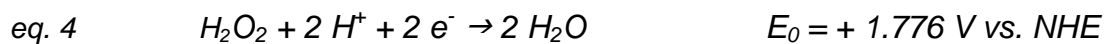


Figure 2 Reaction mechanism of oxygen on Pt or Pt alloy nanoparticle catalysts.

The direct four electron process of oxygen reduction to form water is the preferred and desired reaction pathway (see eq. 2). Hydrogen peroxide formation via direct two electron process according to the half-cell redox process



is the competitive reaction and leads to significant voltage reducing. The following reaction of hydrogen peroxide to water in a two electron process, so called serial four electron process is according to the half-cell redox process



Further, hydrogen peroxide caused to losses in durability of the proton exchange membrane due to the destruction of the polymer⁵. So, new developed and designed PEM fuel cell cathode catalysts need a maximum reducing of the hydrogen peroxide formation.

1.2 Hydrogen PEM fuel cell electrocatalyst research targets

The required targets for a technical application of PEMFCs is the reducing overpotential for the oxygen reduction reaction (ORR) at the fuel cell cathode side⁴ combined with the reducing of the high material cost for the noble metal platinum (more accurately platinum group metals) and the gradual platinum degradation. Figure 3 shows the advised aims of the U.S. Department of Energy for hydrogen PEM fuel cell research and some opportunities to achieve this desired targets⁶.

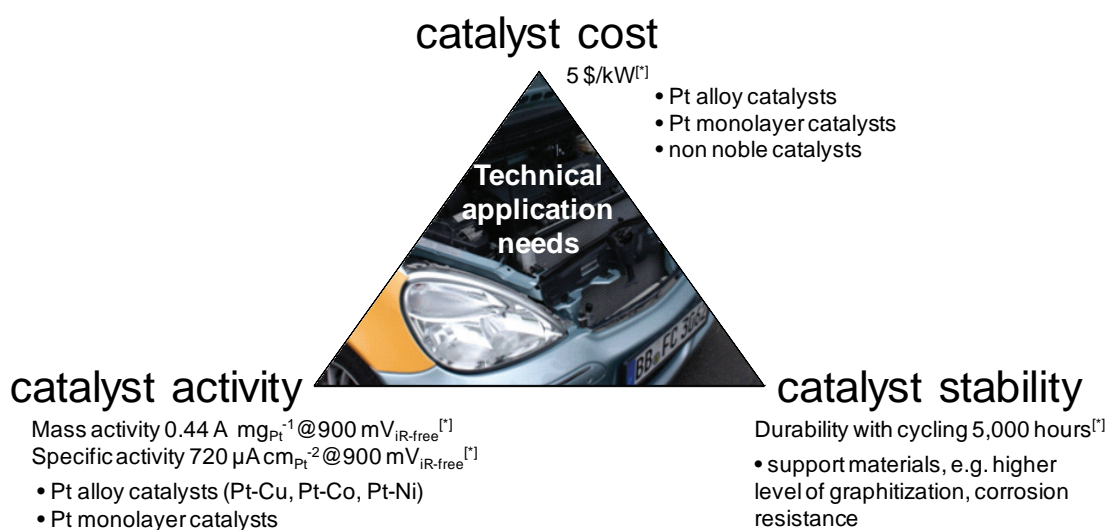


Figure 3 Hydrogen PEM fuel cell research goals. * = ⁶

1.2.1 Catalyst activity

One goal is to increase the catalytic platinum mass based activity from currently 0.12 A mg_{Pt}⁻¹ to at least 0.44 A mg_{Pt}⁻¹ at 900 mV (iR-free) cell voltage and platinum surface area specific based activity of 720 μA cm_{Pt}⁻² at 900 mV (iR-free) cell voltage⁶. To overcome activity limitation a number of different Pt based catalyst concepts, such as Pt monolayer catalysts^{7, 8}, Pt skin catalysts⁹⁻¹¹ and dealloyed Pt multimetallic nanoparticles¹²⁻¹⁹ have been developed in the last decade. All these catalyst concepts show increased catalytic activity for oxygen reduction compared to pure Pt associating with a drop of the Pt amount per unit power in the catalyst and reduce the cost gap for a commercial application.

In particular, Pt-M bimetallic alloys, such as Pt-Co, Pt-Ni and Pt-Cu systems, have received great attention as active electrocatalysts^{15, 16, 20-27}.

More specifically, a well-defined single crystalline Pt₃Ni (111) skin surface showed a 10 times higher mass based and specific ORR activity compared to a comparable pure Pt (111) surface²⁸. Attempts to synthesize stable nanoparticles exhibiting exclusively skin type (111) facets, however, has remained unsuccessful to date²⁹. Furthermore, Pt monolayer catalyst has shown Pt mass based activity improvements in the 10 – 20 times range^{30, 31} due to their tiny amount of Pt, yet are comparable in specific activity enhancements to conventional Pt alloy ORR electrocatalysts.

Dealloyed Pt-M alloy core – shell nanoparticles, obtained from the selective electrochemical leaching of the less noble metal M from the particle surface, have exhibited promising ORR performance in the rotating disk electrode (RDE) as well as membrane electrode assembly (MEA) experiments^{13, 32, 33}. Generally, the dealloyed Pt-Cu system shows higher platinum mass based and surface area specific based activities than the dealloyed Pt-Co system (see chapter 4.1 *Activity, stability, and degradation mechanisms of dealloyed PtCu₃ and PtCo₃ nanoparticle fuel cell catalysts*)^{15, 16, 34-36}. Recently, spurred by a report by 3M^{37, 38} on highly ORR active dealloyed Pt-Ni films, the dealloyed Pt-Ni system is now receiving more interest in the format of alloy films and nanoparticles. So, a lot of Pt-Ni alloy nanoparticles with the variation of Ni amount and synthesis strategies were examined³⁹⁻⁴¹ in the light of the improved ORR activities for extended, well-defined surfaces^{10, 28, 42} to develop functional highly active and practicable fuel cell catalysts (see chapter 4.2 *Activity, structure and degradation of dealloyed PtNi₃ nanoparticle fuel cell electrocatalyst*). Theoretical studies of the electrochemical processes continuously support and predict the catalyst behavior and show attracted interest due to their potentially improved stability at high activity for Pt-Ni catalysts^{19, 43-46}.

1.2.2 Catalyst stability

Another goal is the durability of fuel cell cathode electrocatalysts with performance losses less than 40 % (electrochemical area) of beginning-of-life activities for over 5000 hours⁶.

On the macroscopic scale, catalyst degradation is associated with a loss of electrochemical active surface area (ECSA) at the fuel cell cathode during the voltage cycling. On the microscopic scale, the loss of surface area has been linked to (i) metal coarsening⁴⁷⁻⁴⁹, that is, particle growth based on a free energy driven dissolution / precipitation process (Ostwald ripening), (ii) metal cluster migration and coalescence (Smoluchowski ripening⁵⁰), (iii) metal loss by dissolution into the electrolyte⁴⁹ and (iv) support corrosion associated with a loss of electrical contact of metal nanoparticle^{48, 51, 52}. Figure 4 summarized the various degradation processes of Pt nanoparticles on a carbon surface.

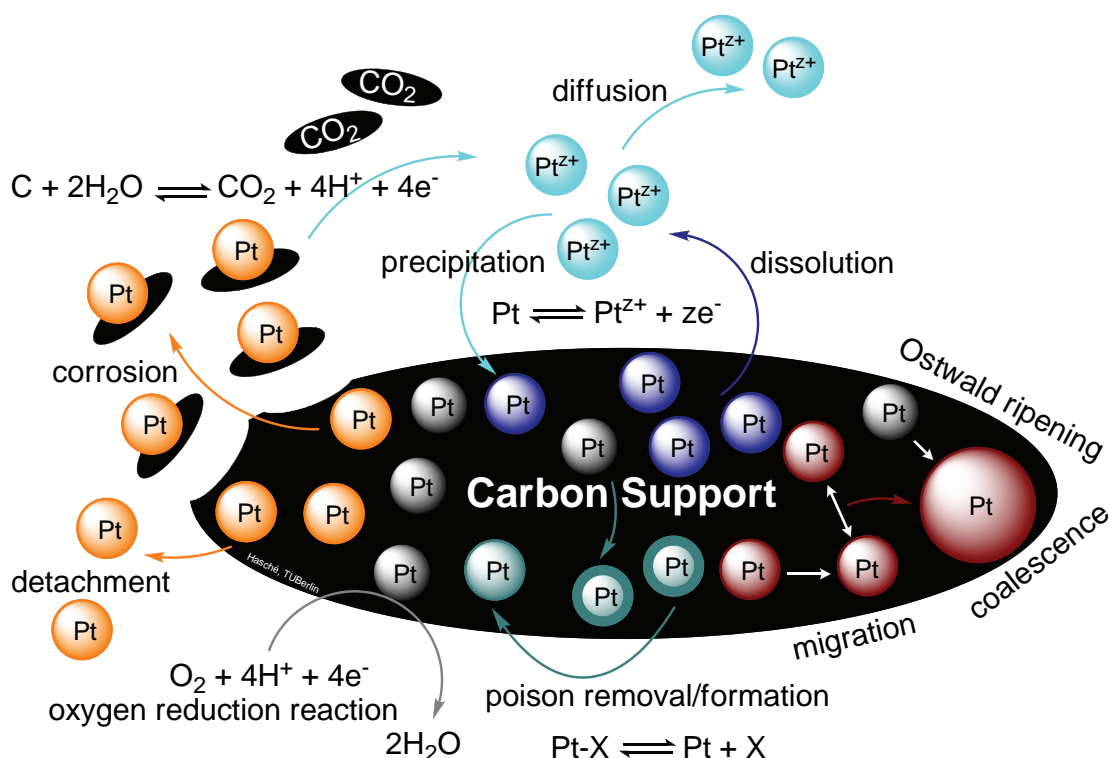


Figure 4 Degradation processes of Pt nanoparticles on carbon support.

Particle coalescence degradation is the growth of nanoparticles upon coalescence while moving along the support surface. This depends on the mobility of the metal particles and their mutual distance. Particle dissolution based degradation (possibly with subsequent redeposition, that is, Ostwald

ripening) depends on electrode potential and particle morphology^{49, 53, 54}. The relation of particle size and dissolution potential is given in the combination of Nernst and Gibbs-Thomson equation (eq. 5)^{49, 55}.

$$\text{eq. 5} \quad E = E(0) - (R T)/(n F) \ln K - (2 \gamma \Omega)/(r n F)$$

With E denoting the particle dissolution potential, E(0) the dissolution potential of flat metal surface, and n, Ω, γ, r being number of transferred electrons, the molar volume, the surface energy, particle radius, and T, F and R having their usual meaning. Based on eq. 5, ECSA loss due to Pt dissolution/redeposition should be significant at large electrode potentials and very small particles.

Carbon corrosion degradation, finally, is facilitated by undersaturated ‘dangling’ carbon bonds. Amorphous carbon blacks exhibit much dangling sp³ bonds and are hence more prone to corrosion degradation than ordered sp² carbon structure elements⁵⁶. As a result of this, lower surface area graphitized carbons and carbon nanotubes (CNT)⁵⁷ promise enhanced corrosion stability (see chapter 3.1 *Multi walled carbon nanotube (MWCNT) supported Pt fuel cell electrocatalyst*)⁵⁸⁻⁶⁰.

Despite their importance for the stability of the active catalyst/support couple^{48, 51, 52}, few new viable support materials concepts have emerged conventional carbon blacks and graphitized carbons continue to be the most popular materials, such as Vulcan XC 72R for catalyst supports. This corroborates the need to more intense search for alternative support materials. Oxidation resistance for the support material is one point of concern⁶¹. Alternatives were evaluated for the oxygen reduction, such as carbon nanotubes^{52, 59} (see chapter 3.1 *Multi walled carbon nanotube (MWCNT) supported Pt fuel cell electrocatalyst*), silicon carbide derived carbons⁶² (see chapter 3.3 *Silicon carbide derived carbon (CDC) supported Pt fuel cell electrocatalyst*), hollow spherical carbons⁶³, nitrogen modified carbons^{64, 65} (see chapter 3.2 *Mesoporous nitrogen doped carbon (meso-BMP) supported Pt fuel cell electrocatalyst*) or titan based materials⁶⁶⁻⁶⁸. Especially nitrogen doped carbons show interesting properties like high conductivity⁶⁹, mesoporosity⁷⁰ and the opportunity to adjust the nitrogen content⁷¹ in the support material.

1.2.3 Catalyst cost

Finally, the reducing of the material cost for the noble metal platinum (more accurately platinum group metals) down to 5 \$ kW⁻¹ is although essential for a commercial technical application⁶. Non-noble metal catalyst concepts⁷²⁻⁷⁷ reduce the cost extremely by absence of a noble metal component but do not meet the activity targets⁶ for commercial fuel cell electrocatalyst up to now. However, Pt alloy nanoparticle concepts are associated with a drop of the Pt amount per unit power in the catalyst and reduce the cost gap for a commercial application. Especially, dealloyed core – shell nanoparticle catalysts can reduce the Pt amount by more than 80%¹⁴. This can be addressed to the fact that the chemical reaction occur only on the nanoparticle surface, so called “shell”. The “core” of the nanoparticle is not involved into the reaction. Here, the noble metal Pt is substituted with a less noble metal (Me) like copper, cobalt or nickel. Figure 5 show the principle of material cost reducing by core – shell structure.

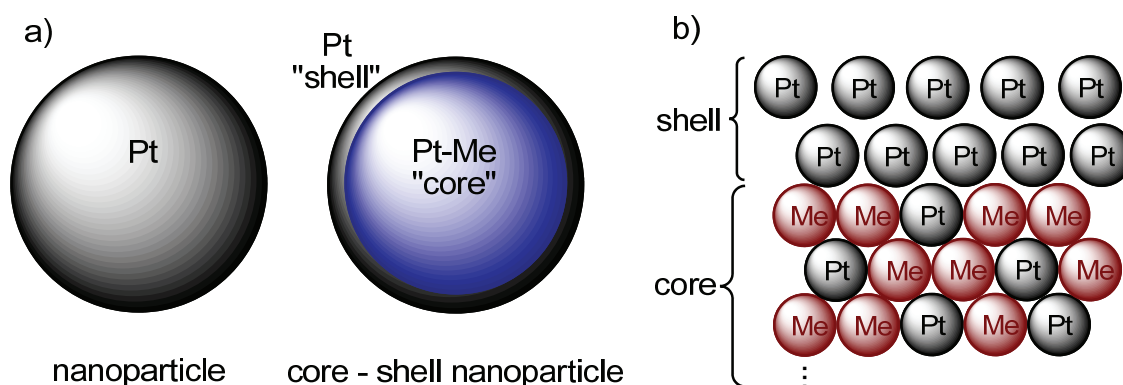


Figure 5 Material cost reducing by core – shell structure, a) global view, b) detail view.

1.3 Research goals and strategy

The goal of this thesis is to improve the understanding of the structure – activity – stability relationship for platinum and platinum alloy nanoparticle PEM fuel cell electrocatalysts. Therefore, the complexity related to the coupled interaction between the support material and catalytically active component has to be reduced. Here, experiments were designed to reduce the complexity by a separation of the effects from the support material and catalytically active component. Thereby, a clearer picture of the structure – activity – stability relationship can be achieved. Figure 6 illustrates the separate research areas and point out the investigated topics of this thesis. The effects of the support material, the effects of the catalytically active component and the thermal stability of Pt nanoparticles were addressed in this thesis work.

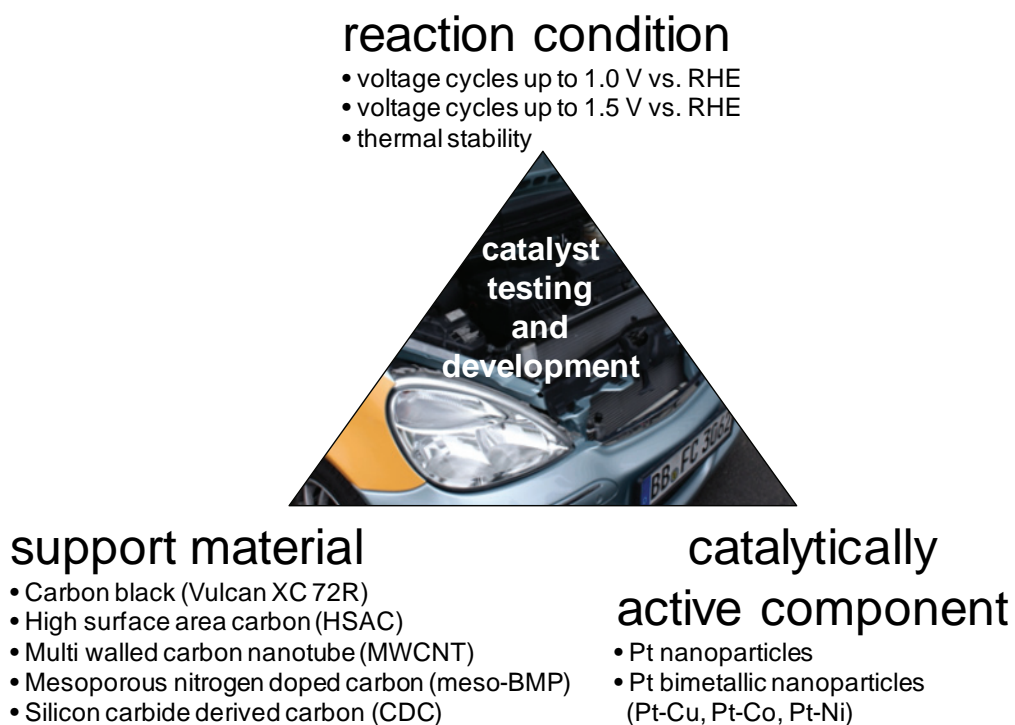


Figure 6 PEM fuel cell catalyst testing and development: topics and agenda.

In the following, a brief overview of important challenges of the three research directions is provided. The reaction conditions influence drastically the activity and stability of PEM fuel cell cathode catalysts. Firstly, the operating voltage range is to mention. The common operating voltage range for cathode electrocatalysts can be split into two regimes. A “lifetime” regime, which represents a normal, general operation range for a fuel cell with voltage potential at and below 1.0 V vs. RHE and a “start-up” regime, which represents voltage potentials rising up to 1.5 V vs. RHE during start-up and shut-down or partial fuel starvation⁶⁰. In particular, the voltage potentials up to 1.5 V vs. RHE dramatically decrease the efficiency of the electrocatalyst because of carbon support corrosion and particle dissolution^{5, 49, 55, 78-81}. The operating temperature of a PEMFC has also effect of the catalyst activity and stability. Generally, an increase of the reaction (operating) temperature causes an increasing kinetic rate of the reaction⁸². So, a typical low temperature PEMFC is operated at 80 °C in contrast to high temperature PEMFC, where operation temperature of 160 °C is desired^{1, 2, 60, 83}.

A PEM fuel cell catalyst as well as generally most heterogeneous catalysts can be split in two parts, the support material and the catalytically active component. The support material is normally a powder and can be characterized by BET surface area, graphitization, porosity and conductivity. On the surface of the support material the catalytically active component is deposited, for example as nanoparticles. The reaction proceeds on its surface. The widely used catalytically active component for PEMFC cathode electrocatalysts is platinum or platinum alloy nanoparticles. Carbon blacks and graphitized carbons such as Vulcan XC 72R and high surface area carbon (HSAC) are the typical support materials for metal nanoparticles.

Finally, derived from the research directions experimental studies were performed to improve the understanding and the open questions are

- How does the support material influence the stability and activity of PEM fuel cell cathode catalysts?

Therefore, platinum nanoparticles of identical structural characterization were evaluated on carbon or carbon based supported catalysts (see chapter 3 *Activity, stability, and degradation of Pt fuel cell electrocatalysts*).

- How does the catalytically active component influence the stability and activity of PEM fuel cell cathode catalysts?

Accordingly, several Pt alloy nanoparticle catalysts were investigated and compared with commercial benchmark pure Pt nanoparticle catalysts (see chapter 4 *Activity, stability, and degradation of Pt alloy fuel cell electrocatalysts*).

- Which are the main factors that affect the thermal stability of PEM fuel cell cathode nanoparticle catalysts?

Here, time-resolved in situ X-ray diffractometry was performed to determine the thermal stability of carbon supported platinum nanoparticle catalysts in absence of an electric field and electrolyte (see chapter 5 *Thermal stability of supported platinum nanoparticle catalysts: in situ studies*).

2 Experimental Part

2.1 Synthesis of Pt/MWCNT

The synthesis of 20 wt. % Pt/MWCNT was prepared via a wet impregnation - freeze drying route followed by annealing step (see Figure 7). A commercial multi walled carbon nanotube (MWCNT) powder (202 mg, Baytubes C150HP, Lot#E0006AAD08, BET surface area of $193 \text{ m}^2 \text{ g}^{-1}$) provided by Bayer Material Science was impregnated with H_2PtCl_6 Hexachloroplatinic acid (255 mg, 20 wt. % platinum, Alfa Aesar, CAS#16941-12-1; Lot#G19S028) precursor and deionized water (1 g, 18 MOhm at room temperature, Sartorius, Germany).



Figure 7 Synthesis strategy – wet impregnation / freeze-drying / furnace reduction.

After the sonification (5 min, output 8 – 5, Branson Sonifier 150, Germany), the well dispersed suspension was frozen in liquid N_2 (>15 min) and freeze-dried under vacuum (4 days, 0.035 mbar, $-52 \text{ }^\circ\text{C}$, Labconco FreeZone6, Germany). After freeze drying the treated powder was annealed in a tube furnace (Carbolite, Germany, see Figure 8) under reductive H_2 atmosphere (6 Vol. % H_2 , 94 Vol. % Ar, quality 5.0, flow rate 100 ml min^{-1} , AirLiquide, Germany). The temperature program (see Figure 9) sequences started with two hours at $250 \text{ }^\circ\text{C}$ for precursor decomposition followed by 7 hours at $300 \text{ }^\circ\text{C}$ for platinum reduction with a heating rate of 10 K min^{-1} . After thermal annealing, the gas was switched to 1 Vol. % O_2 (4.5), 99 Vol. % N_2 (5.0) (flow rate 128 ml min^{-1} , AirLiquide, Germany) for 2 hours to prevent the carbon burning.

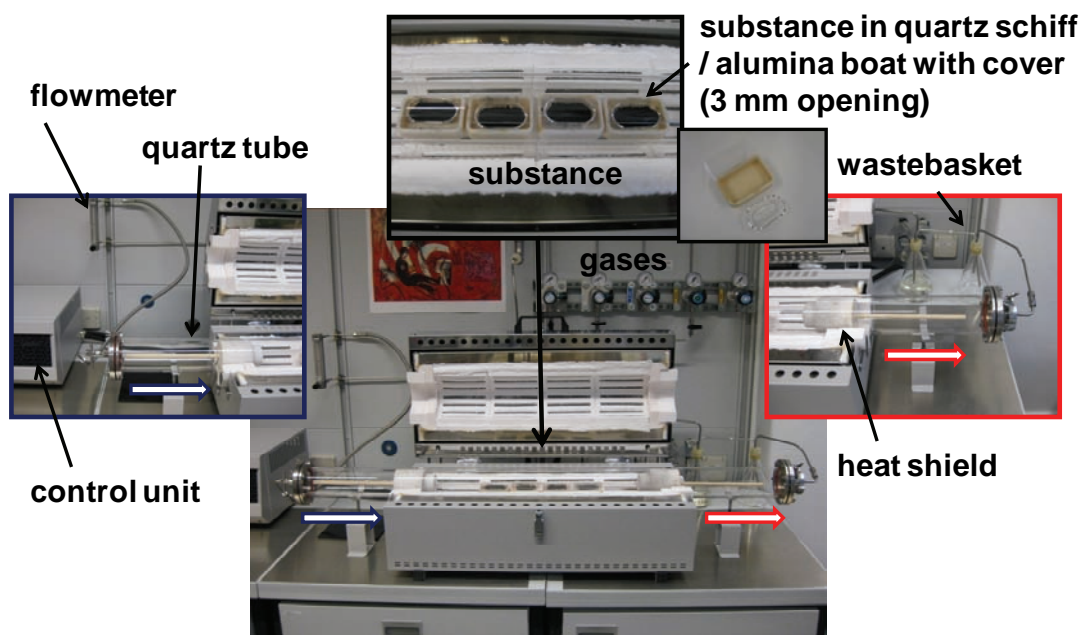


Figure 8 Overview tube furnace setup.

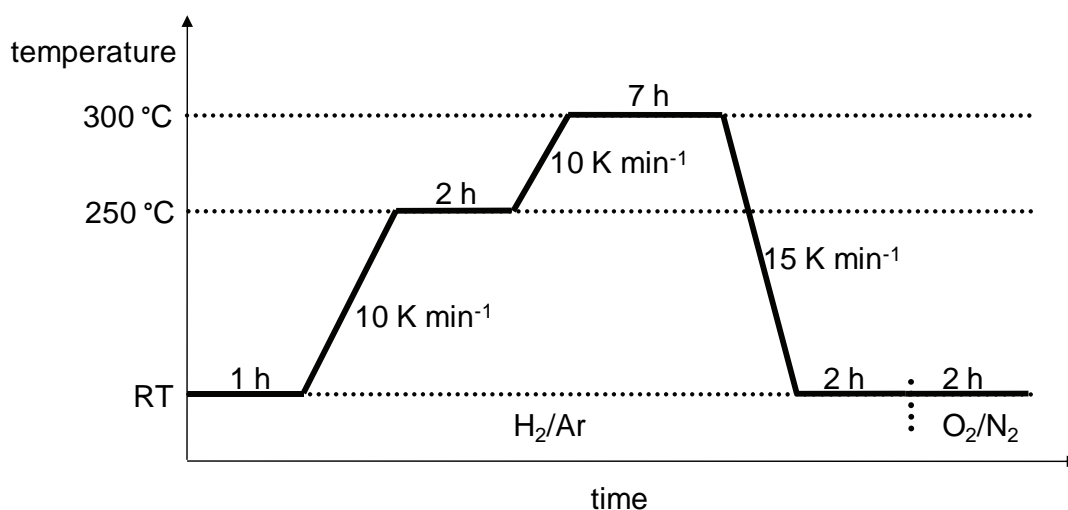


Figure 9 Temperature – time profile for the synthesis of Pt/MWCNT. RT: room temperature, H_2/Ar : 6 Vol.% H_2 (5.0) / 94 Vol.% Ar (5.0), O_2/N_2 : 1 Vol.% O_2 (4.5) / 99 Vol.% N_2 (5.0).

In the following electrochemical experiments of this self made Pt/MWCNT catalyst (BET surface area of $153 \text{ m}^2 \text{ g}^{-1}$) was compared with a commercial Pt/Vulcan XC 72R catalyst (BET surface area of $151 \text{ m}^2 \text{ g}^{-1}$, pure Vulcan XC 72R as support $205 \text{ m}^2 \text{ g}^{-1}$) provided by BASF Fuel Cell Inc.. All chemicals weren't pretreated and stored according to manufacturer's data from delivery companies.

2.2 Synthesis of Pt/meso-BMP

2 g of the ionic liquid N-butyl-3-methylpyridinedicyanamide (BMP-dca, Ionic liquid Technologie GmbH) were mixed with 5 g Ludox HS-40 solution (40 wt.%, aqueous dispersion of SiO₂ nanoparticles, Aldrich, #420816) and carbonized at 800 °C with a heating rate of 10 K min⁻¹ and subsequently an isothermal period at 800 °C for 1 hour in nitrogen. The resulted black powder was triturated in a mortar and the SiO₂ template was removed with 4 M NH₄HF₂ solution (40 ml per gram). After washing with water and drying, the black, fine mesoporous nitrogen doped carbon powder (meso-BMP, 91 mg) was then wet impregnated with a H₂PtCl₆ hexachloroplatinic acid precursor solution (123 mg, 20 wt.% Pt, Alfa Aesar, #040177) and deionized water (2 g, 18 MOhm at room temperature, Sartorius, Germany). The impregnated powder (sonification, 5 min, output 5, Branson Sonifier 150, Germany) was freeze dried under vacuum (4 days, 0.035 mbar, -52 °C, Labconco FreeZone6, Germany). The dried powder was annealed by 250 °C for 2 hours and subsequently 300 °C for 7 hours in a tube furnace (Carbolite, Germany, see Figure 8) under reductive atmosphere (4 Vol. % H₂, 96 Vol. % Ar, quality of 5.0, AirLiquide, Germany). After thermal annealing, the gas was switched to 1 Vol. % O₂ (4.5), 99 Vol. % N₂ (5.0) (flow rate 128 ml min⁻¹, AirLiquide, Germany) for 2 hours to prevent the carbon burning. The Pt/meso-BMP catalyst exhibited a calculated Pt loading of 21.4 wt.%. A benchmark, commercial high surface area carbon (HSAC) supported Pt nanoparticle catalyst (28.2 wt.% Pt, TEC10E30E, Lot#108-0331, TKK) was taken for the comparison of ORR activities and ECSA. All chemicals were used as received from the delivery companies.

2.3 Synthesis of PtCu₃/HSAC and PtCo₃/HSAC

PtCu₃/HSAC (21.9 wt.% Pt, BET surface area $\approx 330 \text{ m}^2 \text{ g}^{-1}$) and PtCo₃/HSAC (22.1 wt.% Pt, BET surface area $\approx 246 \text{ m}^2 \text{ g}^{-1}$) alloy nanoparticle precursor electrocatalysts supported on high surface area carbon (HSAC) were synthesized via wet impregnation and freeze-drying route followed by annealing in a tube furnace under reductive atmosphere (see Figure 7)^{15, 16}. A commercial 28.2 wt.% Pt/HSAC nanoparticle electrocatalyst (250 mg, TEC10E30E, Lot#108-0331, TKK, BET surface area $\approx 400 \text{ m}^2 \text{ g}^{-1}$) was impregnated with an aqueous precursor solution of (251 mg, Cu(NO₃)₂ · 2.5 H₂O, Sigma-Aldrich, #467855 or 316 mg, Co(NO₃)₂ · 6 H₂O, Alfa Aesar, #010694) and deionized water (3 – 4 ml, 18 MOhm at room temperature, Sartorius, Germany). After sonification (5 min, output 7 – 8, Branson Sonifier 150, Germany) the well dispersed suspension was frozen in liquid N₂ (>15 min) and subsequently freeze-dried under vacuum (2 – 3 days, 0.035 mbar, -52 °C, Labconco FreeZone6, Germany). The resulting dried powder was annealed by 800 °C for 7 hours in a tube furnace (Carbolite, Germany, see Figure 8) under reductive atmosphere (4 Vol. % H₂, 96 Vol. % Ar, quality 5.0, flow rate 100 ml min⁻¹, AirLiquide, Germany). Before the maximum temperature has been reached, the sample was thermally pretreated at 250 °C for 2 hours to decompose the precursor anion. After thermal annealing, the gas was switched to 1 Vol. % O₂ (4.5), 99 Vol. % N₂ (5.0) (flow rate 128 ml min⁻¹, AirLiquide, Germany) for 2 hours to prevent the carbon burning. All chemicals were used as received from the delivery companies.

2.4 Synthesis of PtNi₃/Vulcan XC 72R

Carbon (Vulcan XC 72R) supported PtNi₃ alloy nanoparticle catalyst with a Pt loading of 32.9 wt.% was prepared via wet impregnation, freeze-drying method and followed by annealing in a reductive atmosphere (see Figure 7)^{15, 16}. A commercial 46.7 wt.% Pt/Vulcan XC 72R catalyst (1 g, TEC10V50E, Lot#106-2731, TKK) was impregnated with a Ni precursor solution (2 g, Ni(NO₃)₂ · 6 H₂O, AlfaAesar, #010816) and deionized water (67 ml, 18 MOhm at room temperature, Sartorius, Germany). The used metal contents corresponded to the formation of Pt-Ni alloy with an atomic ratio of 1:3 by a complete conversion. The suspension was sonicated (20 min, output 8, Branson Sonifier 150, Germany) and then frozen in liquid N₂ (>20 min) for the freeze-drying process. After freeze-drying (more than a week, 0.035 mbar, -52 °C, Labconco FreeZone6, Germany), the dried impregnated powder was annealed in a tube furnace (Carbolite, Germany, see Figure 8) by 800 °C for 7 hours in a reductive atmosphere (4 Vol.% H₂, 96 Vol.% Ar, quality 5.0, flow rate 100 ml min⁻¹, AirLiquide, Germany). Before the maximum temperature was achieved, the Pt-Ni precursor powder had been pretreated at 250 °C for 2 hours to decompose the precursor anions. After thermal annealing, the gas was switched to 1 Vol. % O₂ (4.5), 99 Vol. % N₂ (5.0) (flow rate 128 ml min⁻¹, AirLiquide, Germany) for 2 hours to prevent the carbon burning. All chemicals were used as received without further purification.

To compare the dealloyed PtNi₃ nanoparticle catalyst with a pure Pt catalyst by similar mean particle size, a commercial, pure 46.7 wt.% Pt/Vulcan XC 72R catalyst (TEC10V50E, Lot#106-2731, TKK) was heat treated (denoted as Pt/Vulcan XC 72R (HT) or Pt (HT)) with the same annealing protocol which was used earlier for the Pt-Ni alloy formation.

2.5 Structure and composition characterization

2.5.1 X-Ray diffraction (XRD) measurement in Bragg-Brentano geometry

The characterization of electrocatalysts was carried out with a D8 Advanced X-ray Diffractometer from Bruker AXS equipped with a position sensitive LynxEye detector (PSD) (see Figure 10). The Cu K α tube is operated at a voltage of 40 kV and current of 40 mA. Followed scanning parameters were used: 2θ range from 15° to 80°, step size of 0.01°, holding time of 7 second per step, variable divergence slit of 4 mm, PSD Iris from 13 and sample rotation of 15 rpm. The X-ray diffraction (XRD) sample holder was a custom made plexiglas disk. In the center of the disk is a 1 mm depth well with a diameter of 1 cm to position the catalyst powder sample. The catalyst powder was given into the well and carefully flattened and flushed to form a smooth surface. All XRD profiles were analyzed with using TOPAS (Bruker AXS, Version 4-2).

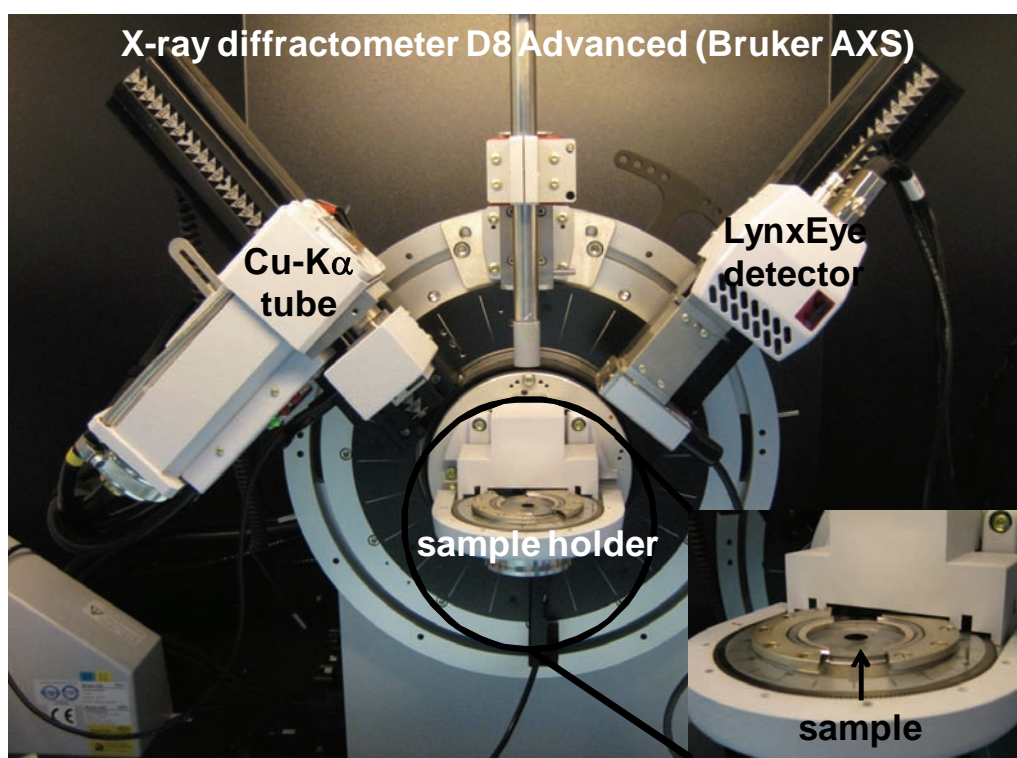


Figure 10 X-ray diffractometer setup in Bragg-Brentano geometry.

2.5.2 In situ high temperature X-ray diffraction (HT-XRD) measurements in parallel beam geometry

Figure 11 show the high temperature diffractometer setup. The in situ HT-XRD measurements in parallel beam geometry were recorded using a Bruker AXS D8 Advanced X-ray Diffractometer equipped with a Goebel mirror (1), a position sensitive LynxEye detector (PSD) (2), and an external radiation heating chamber (MRI Physikalische Geraete GmbH, Germany) (3). The heating chamber was positioned on the goniometer of the diffractometer. It consisted of an AlCr foil as heater (4), rotatable Al_2O_3 crucible as sample holder (5) and a thermocouple (6).

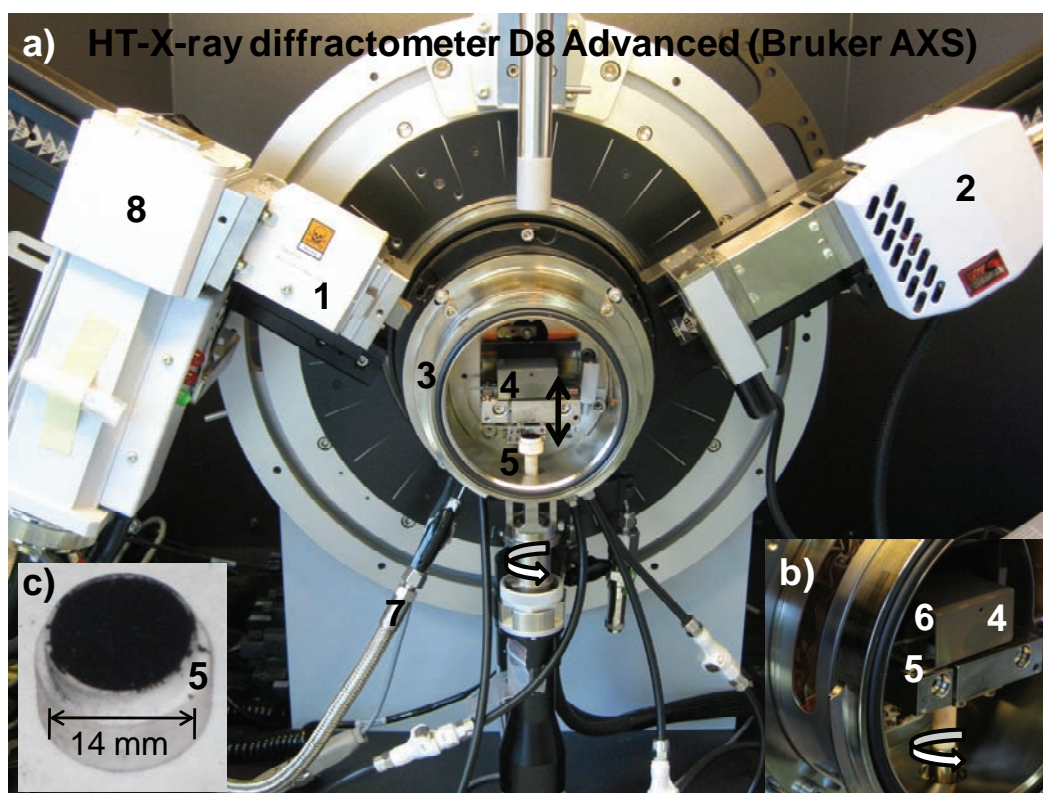


Figure 11 High temperature X-ray diffractometer (HT-XRD) setup in parallel beam geometry, a) overview, b) detail view heating chamber, c) Al_2O_3 crucible with sample.

The heater was fixed above the sample and the thermocouple was very close to the crucible. The chamber was heated up to 80 °C or 160 °C under nitrogen or synthetic air (20.5 % O_2 in N_2 , hydrocarbon free, quality 5.0, AirLiquide) atmosphere with a flow rate of 75 ml min^{-1} (7). The Cu $K\alpha$ tube (8) was operated at a voltage of 40 kV and current of 40 mA. For the sample preparation the Al_2O_3 crucible was filled with Pt/C (5 – 10 mg).

The sample powder was subsequently flattened to form a smooth surface (see Figure 11c). The temperature time protocol started with an initial XRD scan at 30 °C and then heated up with 1 °C s⁻¹ to the maximum temperature (80 °C or 160 °C). At 80 °C / 160 °C the XRD profiles were acquired each 2 hours at the beginning, after the holding time of 10 hours then only each 5 hours. The followed XRD scanning parameters were used: 2 Θ range from 33° to 53°, step size of 0.03°, holding time of 3 second per step, fix divergence slit of 2 mm, PSD Iris antiscattering slit of 13 and sample rotation. The mean crystallite size was estimated using the integral breath method⁸⁴ (TOPAS, Version 4-2, Bruker AXS) from the (111) and (200) reflections of the fcc pure platinum.

“Z drive” test. The alignment of the HT-XRD is to describe in the following way: The prepared Al₂O₃ crucible sample holder (Figure 11c) is positioned on the automatic driven rotator of the radiation heating chamber (Figure 11a, 5). The X-ray source and the detector are positioned at 2 $\Theta = 0^\circ$. This adjustment is referred to as a direct alignment. Due to the very high intensity of X-ray source during the direct alignment, a slit of 1 mm and a Cu absorber filter are used at the primary (Figure 11a (1), X-ray tube and Goebel mirror) and secondary (Figure 11a (2), PSD detector) optics of the diffractometer, respectively. The chosen scan type is a PSD fix scan, where the X-ray source is only moved at a fix position of the PSD detector. The used parameters are $\Theta = - 0.5^\circ$ and $+ 0.5^\circ$ for the X-ray tube, step size of 0.02°, Z = 3 to 6 and holding time 1 s. A *“Z drive”* test for each sample powder is essential to find out the optimal sample height for accurate $\Theta - \Theta$ XRD measurements (see Figure 12, left side). Therefore, the height of the sample holder is automatically changed using the Bruker software WIZARD, referred to as a *“Z drive”*. The series of XRD profiles are recorded by various Z heights (use the function “loop” in WIZARD) at a rotating sample to establish the course of the intensity in dependence on the Z position. Figure 12 (right side) illustrates a *“Z drive”* testing for the alignment on the HT-XRD. If the Z height of the sample is too low or too high, the detector records the full intensity or no intensity of the X-ray source, respectively. The optimal Z height is only achieved, when the intensity is the half of the maximum intensity.

The effects of displacement can be neglected by an optimal Z height and parallel beam geometry.

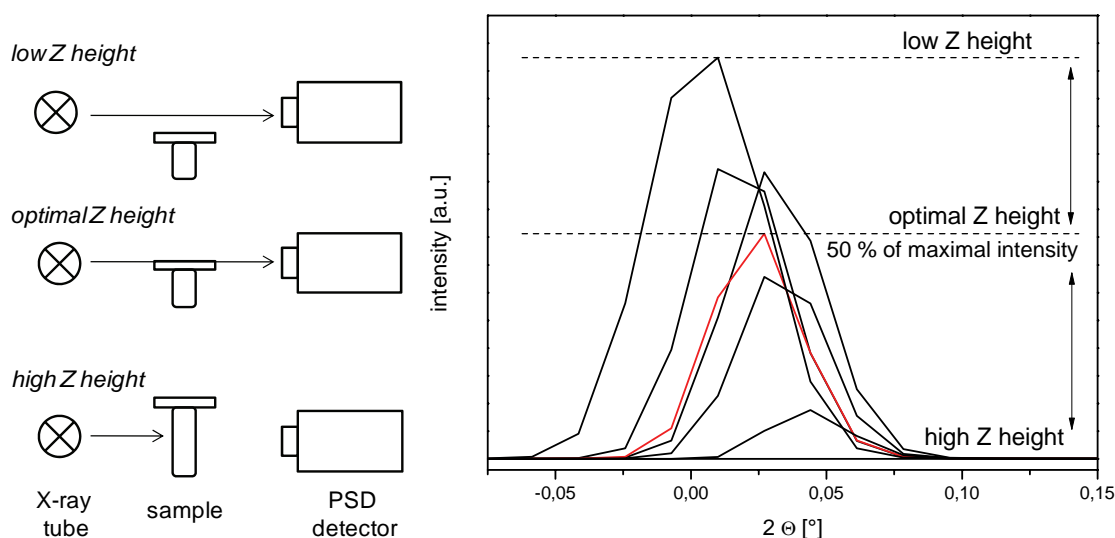


Figure 12 Alignment of the HT-XRD. Left side: Schematic sketch of the “Z drive”. Right side: Series of XRD patterns at various values of Z height recorded by a direct beam and PSD fix scan. The optimal Z height is only achieved, when the intensity is the half of the maximum intensity. XRD parameters: $\theta = -0.5$ to $+0.5^\circ$ for the X-ray tube, step size of 0.02° and holding time 1 s.

Calibration of the thermocouple. The calibration of the HT-XRD and the optimal distance between the thermocouple (Figure 11a, 6) and sample occur by measuring of standard materials. The accurate temperature is to establish by standards to eliminate errors during the HT-XRD experiments. The important property of standard materials is the clear change of crystal structure (by melting or phase transformation) at a distinctly elevated temperature, which can be traced by recording of series of XRD profiles. The thermal phase transformation of α -quartz (trigonal) to β -quartz (hexagonal) in a 2θ range of 25° to 27° at 573°C , as an example, is shown in Figure 13. The shift of the reflection at various temperatures is clearly to observe in Figure 13a. Figure 13b illustrates the three-dimension illustration of the phase transformation of α -quartz (trigonal) to β -quartz (hexagonal) displayed using the Bruker EVA software. The experimentally observed difference of the temperature, where the phase transformation proceeds, can be reduced by the position change of the thermocouple. The value of ΔT should be in the range of $5 - 10^\circ\text{C}$.

Further standard materials are aluminum (melting point of 660 °C), copper (melting point of 1085 °C), KNO₃ (phase transformation from orthorhombic to trigonal at 128 °C).

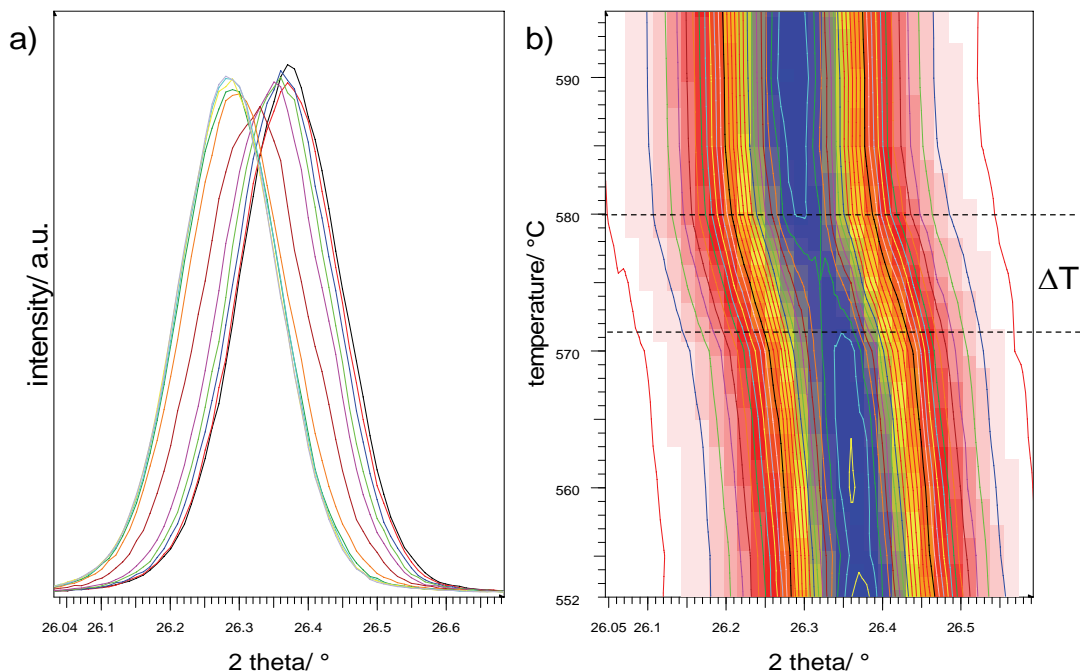


Figure 13 Calibration of the thermocouple by temperature-dependent XRD measurements from α -quartz (trigonal) to β -quartz (hexagonal). a) Series of XRD patterns at various temperatures in the range of 552 °C to 595 °C. b) Three-dimension representation of the phase transformation of α -quartz to β -quartz. XRD parameters: $2\theta = 25.5$ to 28° , step size of 0.01° and holding time of 2 s.

2.5.3 Transmission electron microscopy (TEM) measurements

The morphology of platinum or platinum alloy nanoparticles was observed through the transmission electron microscopy (TEM), FEI TECNAI G² 20 S-TWIN equipped with energy dispersive X-ray spectroscopy (EDS) and GATAN MS794 P CCD-Camera (see Figure 14a).

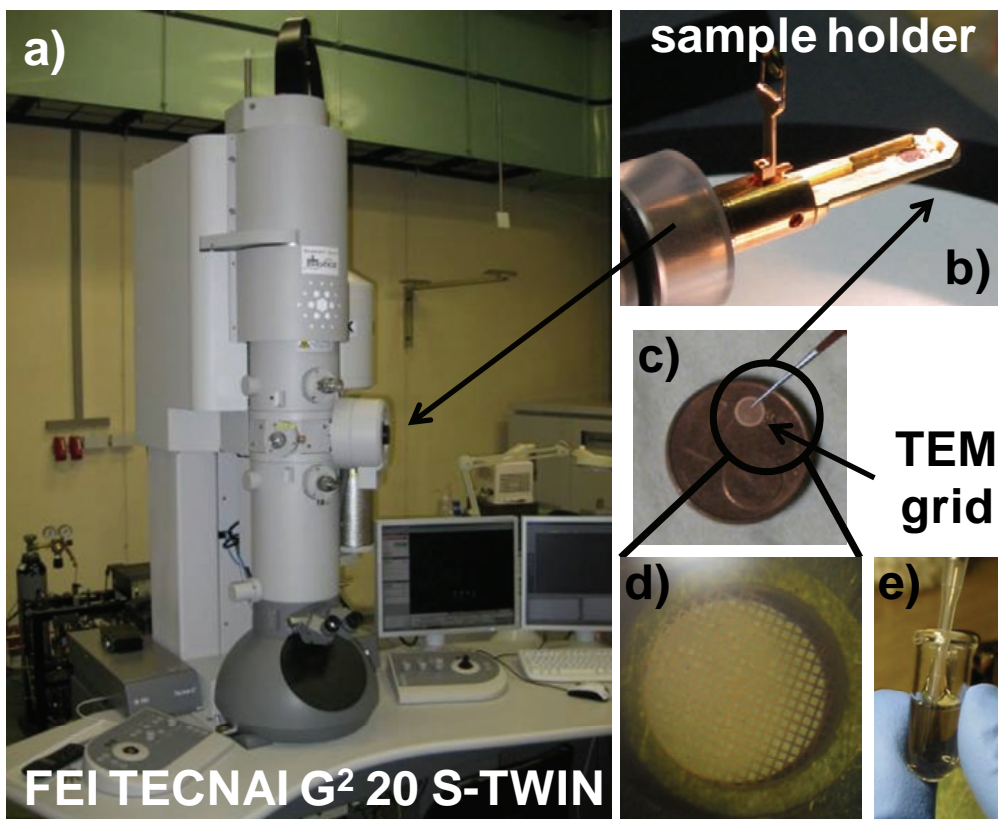


Figure 14 Transmission electron microscope (TEM) setup, a) overview TEM, b) sample holder, c-d) TEM grid with holey carbon film, e) sample suspension.

TEM was operated by the accelerating voltage of 200 kV. The optimal resolution of this microscopy is 0.24 nm in Bright field. Further, the initial catalyst powders and saved catalyst film after the electrochemical testing were sonicated in a mixture of isopropanol and water (see Figure 14e). An aliquot was pipette on a Cu, Al or Au grid with holey carbon film (PLANO, Germany) and dried in air (see Figure 14c-d). The analysis of the TEM images was occurred with analySIS FIVE software (SIS, Soft Imaging Systems, Olympus) to determine the particle size distribution by counting of more than 400 particles of carbon supported platinum and platinum alloy nanoparticles.

2.5.4 Energy dispersion X-ray spectroscopy (EDS) measurements

The chemical composition of Pt alloy nanoparticle precursor catalysts before and after electrochemical testing was determined using a high resolution Hitachi S-4000 Scanning Electron Microscope equipped with a cold field emitter and an energy dispersive X-ray spectroscopy (EDS). EDS was operated at an accelerating voltage of 20 kV, a beam current of 0.4 nA and a working distance of 20 mm. The sample was prepared on a carbon tab (PLANO, Germany). The EDS scans for each sample were analyzed and averaged about a large range on different sample positions.

2.5.5 Brunauer-Emmett-Teller (BET) surface area measurements

The Brunauer-Emmett-Teller (BET) method was used to determine the surface area of the supported nanoparticle catalysts. A known amount of sample is filled in the BET sample cell (Figure 15). To get accurate results a minimum area of 10 m^2 is required for a measurement.

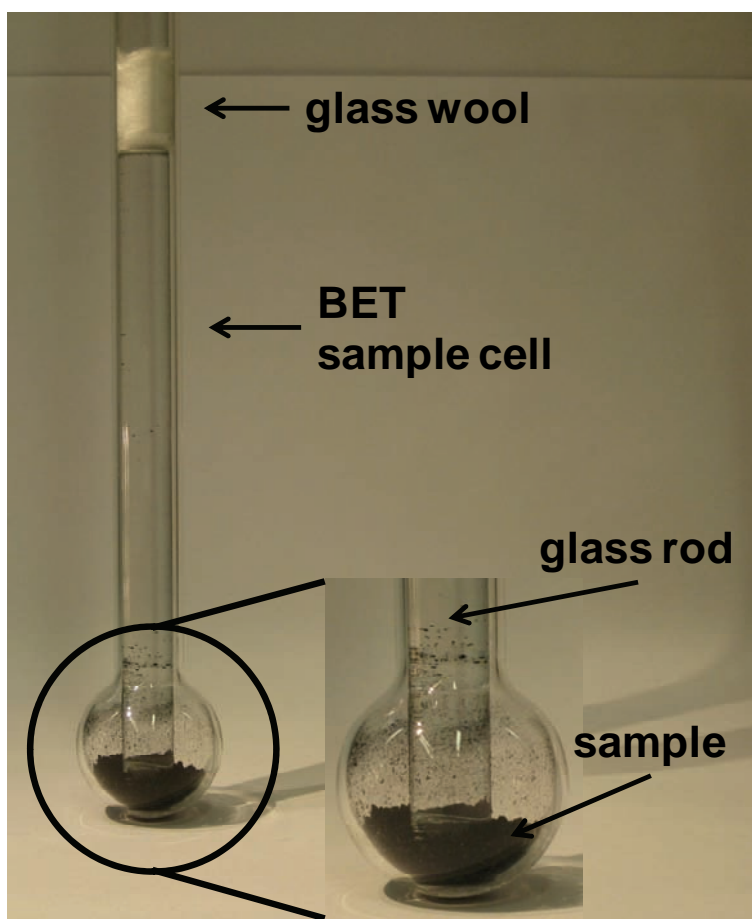


Figure 15 BET sample cell.

After the sample had been degassed overnight at $60 \text{ }^\circ\text{C}$ in vacuum, the nitrogen adsorption isotherm was measured at 77 K using an Autosorb-1 from Quantachrome, Germany. A correlation coefficient of 0.999 was achieved for the BET surface area measurements of the supported nanoparticle catalysts.

2.6 Electrochemical characterization using rotating disk electrode (RDE)

2.6.1 Preparation of catalytic active thin film electrodes

The preparation of the working electrode is shown in Figure 16. To prepare the thin catalytic film on the GC electrode surface, the catalyst powder (a) was mixed (b) with deionized water, 2-propanol and Nafion (5 wt.% of stock solution). The mixture was then horn sonicated (c) (5 – 30 min, output 8, Branson Sonifier 150, Germany).

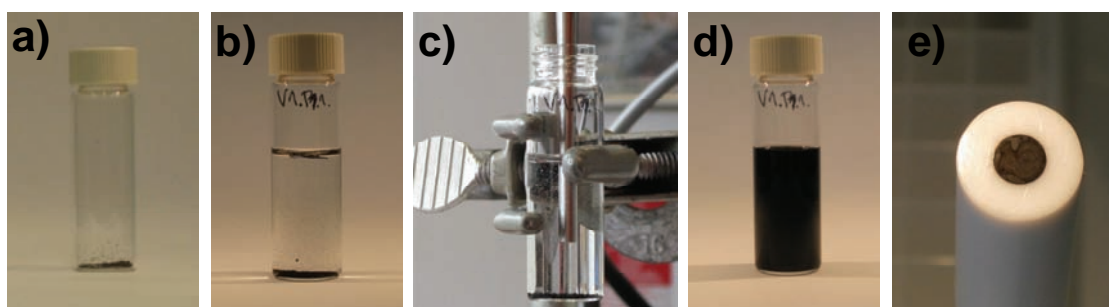


Figure 16 Preparation of the working electrode.

After sonification (d), an aliquot of catalyst mixture was pipetted onto the previously polished (1st 5 min, Buehler Alpha Micropolish Alumina 1 and NYLON PSA 2-7/8", 2nd 5 min, Buehler Gamma Micropolish II Alumina 0.05 and Microcloth PSA 2-7/8") and cleaned (bath sonicated, 5 min each step, 1st deionized water, 2nd acetone, 3th deionized water) GC electrode and dried at 60 °C for 10 min in air. The homogenous thin catalytic film (e) obtained a typical calculated Pt loading between 10 and 27 $\mu\text{g}_{\text{Pt}} \text{cm}_{\text{geo.}}^{-2}$. The influence on different Pt mass loadings in this given range is to neglect. Table 1 summarized the used catalyst mixture recipes.

Table 1 Catalyst mixture recipes for thin film electrode preparation.

chapter	m_{catalyst} [mg]	V_{water} [ml]	$V_{\text{2-propanol}}$ [ml]	V_{Nafion} [μl]
3.1	5	2.50	2.50	0
3.2	5	1.99	0.50	10
3.3	9	1.99	0.50	10
4.1, 4.2	5	3.98	1.00	20

2.6.2 Rotating disk electrode (RDE) setup

Figure 17 shows the rotating disk electrode (RDE) setup (a – detail view, b – overview) which was used for the electrochemical characterization and stability tests^{85, 86}. A custom-made three compartment electrochemical glass cell (7) was used as a three electrode setup with a Pt mesh as counter electrode (3) and a mercury-mercury sulfate electrode (Ametek, Germany) as reference electrode (2). The reference electrode was held in place by a Luggin-Haber capillary (c, 8). The working electrode was a commercial glassy carbon electrode (GC electrode) (4) with a fixed diameter of 5 mm (PINE Instruments, USA). The electrolyte can be purged through a frit (5, 6). A commercial potentiostat (VSP-5, BioLogic, France) and a PINE rotator (1) were used for the RDE experiments.



Figure 17 Rotating disk electrode (RDE) setup, a) detail view, b) overview.

The RDE experiments were conducted in a 0.1 M HClO_4 electrolyte solution, prepared by diluting of 70% redistilled HClO_4 (Sigma-Aldrich, #311421) with deionized water (18 M Ω m at room temperature, Sartorius, Germany). The working electrode was outside of the electrolyte and no potential was applied during purging with gases. The immersion of the working electrode into the electrolyte was applied under potential control (0.06 V vs. RHE) until the electrochemical experiment started immediately. All measurements were operated at room temperature.

2.6.3 Activity for the oxygen reduction reaction (ORR) using linear sweep voltammetry (LSV)

For the determination of the activity for the oxygen reduction reaction (ORR) linear sweep voltammetry (LSV) measurements were conducted using the RDE technique. The intrinsic kinetic current at 0.9 V vs. RHE was corrected with the mass transport diffusion limiting current between 0.2 and 0.5 V vs. RHE (see Figure 18). All LSV experiments were performed with a rotating speed of 1600 rpm (rounds per minute) and a scan rate of 5 mV s^{-1} in oxygenated 0.1 M HClO_4 electrolyte, under oxygen atmosphere at room temperature, by sweeping the potential from 0.06 V vs. RHE anodically to the open circuit potential (around 1.1 V vs. RHE).

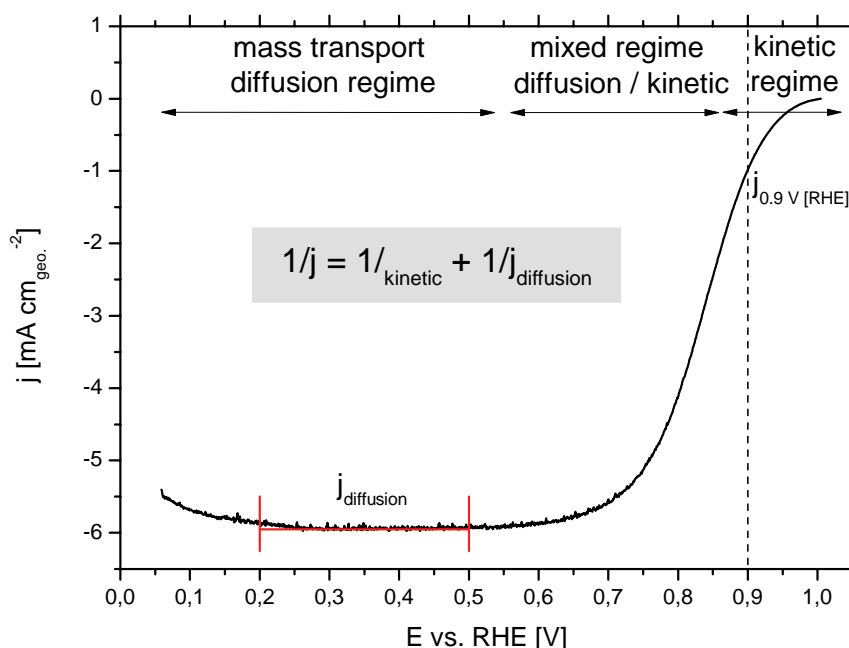


Figure 18 Analysis of a linear sweep voltammogram (Pt/C, 0.06 – 1.00 V vs. RHE, 5 mV s^{-1} , 1600 rpm, sat. O_2 , 0.1 M HClO_4 , room temperature).

For the Koutecky – Levich plot the rotation speed was varied in a range between 800 and 2400 rpm in oxygenated 0.1 M HClO_4 at room temperature. All reported activities were established at 0.9 V vs. RHE and compared to each other. All electrode potentials were converted into and are reported to the reversible hydrogen electrode (RHE) scale.

2.6.4 Platinum electrochemical active surface area (ECSA) using cyclic voltammetry (CV)

Cyclic voltammograms (CVs) were recorded in deaerated 0.1 M HClO₄ electrolyte through bubbling with nitrogen under nitrogen atmosphere at room temperature. To estimate the platinum electrochemical active surface area (ECSA) CV profiles were recorded between 0.06 and 1.00 V vs. RHE with a scan rate of 100 mV s⁻¹. The platinum ECSA was calculated using the mean integral charge of the hydrogen adsorption / desorption area with double layer current corrected at 0.4 V vs. RHE and with 210 μC cm_{Pt}⁻², assuming one hydrogen atom observed to one platinum atom (see Figure 19).

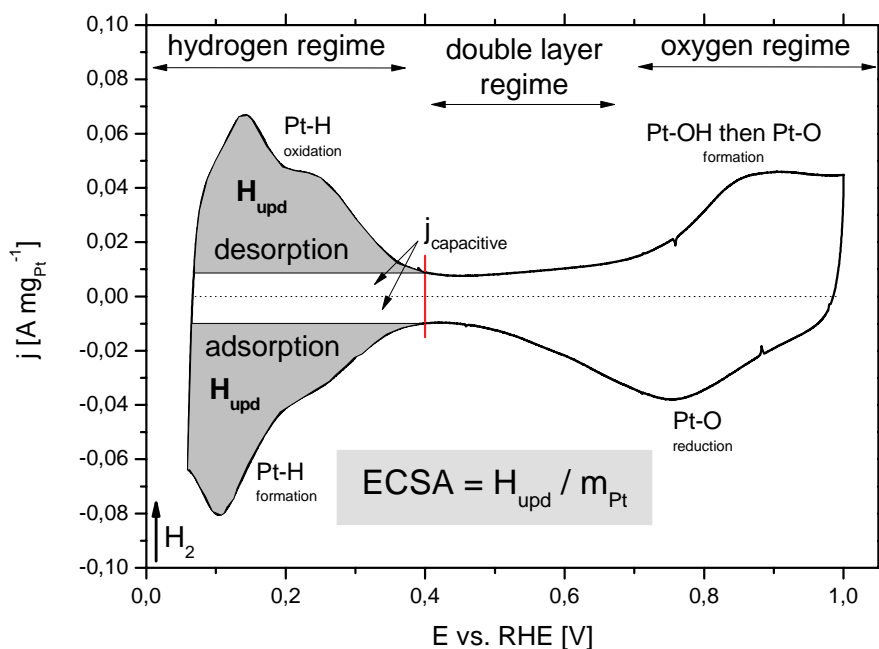


Figure 19 Analysis of a cyclic voltammogram (Pt/C, 0.06 – 1.00 V vs. RHE, 100 mV s⁻¹, sat. N₂, 0.1 M HClO₄, room temperature).

2.6.5 Electrochemical long-term durability experiments

Two different cycling voltammetry (CV) test modes were used for electrochemical stability testing. These long-term stability tests are accelerated degradation tests to simulate the long-term behavior of fuel cell electrocatalysts. All experiments were conducted in nitrogen purged 0.1 M HClO₄ under nitrogen atmosphere at room temperature.

The “lifetime” stability testing with 10000 voltage cycles was performed from 0.5 to 1.0 V vs. RHE at the scan rate of 50 mV s⁻¹. During the run-time three CVs from 0.06 to 1.00 V vs. RHE at a scan rate of 100 mV s⁻¹ were measured in each case after 500, 1000, 1500, 2000, 4000, 6000, 8000 and 10000 voltage cycles to determine the platinum electrochemical active surface area (ECSA) (see Figure 20).

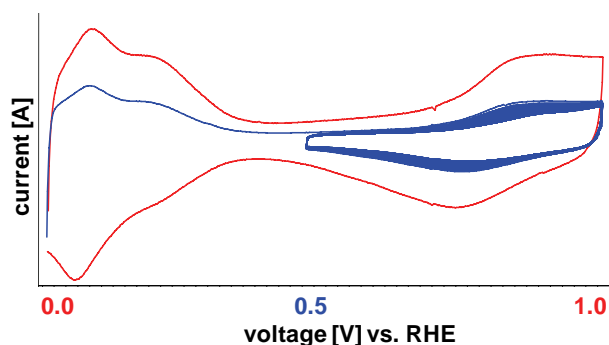


Figure 20 Voltage cycling in the “lifetime” stability test regime.

The “start-up” stability testing with 2000 voltage cycles was performed from 0.5 to 1.5 V vs. RHE at a scan rate of 50 mV s⁻¹. Thereby, during the run-time three CVs from 0.06 to 1.00 V vs. RHE at a scan rate of 100 mV s⁻¹ were also carried out in each case after 250, 500, 750, 1000, 1250, 1500, 1750 and 2000 voltage cycles to generate the platinum ECSA (see Figure 21).

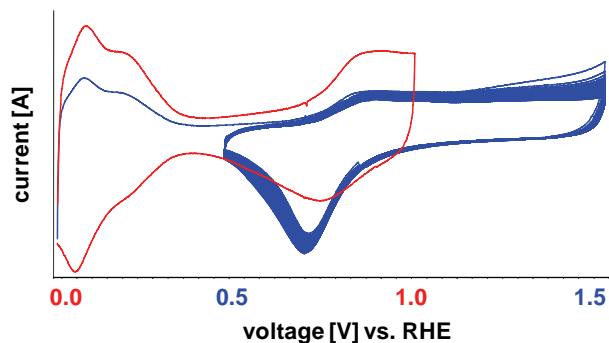


Figure 21 Voltage cycling in the “start-up” stability test regime.

2.6.6 Electrochemical dealloying procedure

Before the measurement of the initial activity and stability testing, all catalysts (without chapter 3.1 *Multi walled carbon nanotube (MWCNT) supported Pt fuel cell electrocatalyst*) were pretreated by voltammetric cycling, so called electrochemical dealloying. The dealloying procedure consists of three full CV profiles (0.06 – 1.00 V vs. RHE with a scan rate of 100 mV s⁻¹), following by 200 fast CV profiles from 0.06 to 1.00 V vs. RHE at a scan rate of 500 mV s⁻¹ and finally three full CV profiles (0.06 – 1.00 V vs. RHE with a scan rate of 100 mV s⁻¹) to leach off the less noble metal from the particle surface of the Pt alloys. This voltammetric pretreatment of the Pt alloy nanoparticle precursor electrocatalysts offered the formation of highly active bimetallic core – shell nanoparticles^{13, 15, 16}. For the comparison all pure Pt nanoparticle electrocatalysts was pretreated voltammetric with the same dealloying process. The resulting dealloyed catalysts after the voltammetric activation are now denoted as initial catalysts. All electrode potentials were converted into and are reported in the reversible hydrogen electrode (RHE) scale.

3 Activity, stability, and degradation of Pt fuel cell electrocatalysts: support effects

A multitude of new and improved catalyst materials and concepts for membrane fuel cells were developed over the last decade. The requirements of these catalysts are low cost, high activity and durability (see chapter 1.2 *Hydrogen PEM fuel cell electrocatalyst research targets*). In this chapter, different support materials for Pt nanoparticles like

- multi walled carbon nanotubes (MWCNT) (see chapter 3.1),
- mesoporous nitrogen doped carbon (meso-BMP) (see chapter 3.2) and
- silicon carbide derived carbon (CDC) (see chapter 3.3)

were characterized, evaluated and compared with commercial benchmark pure Pt nanoparticle catalysts for the oxygen reduction reaction. It's addressed the question, how does the support material influence the stability and activity of PEM fuel cell cathode catalysts?

Finally, an overview of the different supported Pt nanoparticle electrocatalysts is presented (see chapter 3.4 *Overview – support effects*).

3.1 Multi walled carbon nanotube (MWCNT) supported Pt fuel cell electrocatalyst

This chapter is based on the publication

Hasché, F.; Oezaslan, M.; Strasser, P.,

Activity, stability and degradation of multi walled carbon nanotube (MWCNT) supported Pt fuel cell electrocatalysts.

Physical Chemistry Chemical Physics **2010**, 12, (46), 15251-15258

<http://dx.doi.org/10.1039/C0CP00609B>

Reproduced by permission of The Royal Society of Chemistry.

In this chapter we compare the electrochemical active surface area, electrocatalytic performance, and morphological stability of a MWCNT (Bayer Materials Science, Baytubes) supported Pt nanoparticle cathode electrocatalyst with that of a conventional furnace black carbon supported Pt catalyst (BASF Fuel Cell). We directly find microscopic evidence for Pt particle migration over relatively long distance, at room temperature. However, our findings suggests that particle growth and coarsening are not controlling the loss of electrochemical active surface area for long voltage cycling (thousands of cycles). We rather conclude that carbon corrosion associated with Pt particle detachment from the conductive support is more likely to account for ECSA losses for long-term cycling. This chapter highlights that MWCNT supports do not enhance the ORR activity of Pt nanoparticles, however offer significant carbon durability advantages.

3.1.1 Structural characterization of carbon supported Pt nanoparticles

The X-ray diffraction (XRD) profiles of synthesized Pt/MWCNT (see chapter 2.1 *Synthesis of Pt/MWCNT*) and Pt/Vulcan XC 72R are shown in Figure 22. The pertinent reference reflections are indicated by vertical dashed lines. Platinum (111), (200) and (220) reflections are consistent with a face centered cubic (fcc) Fm3m space group.

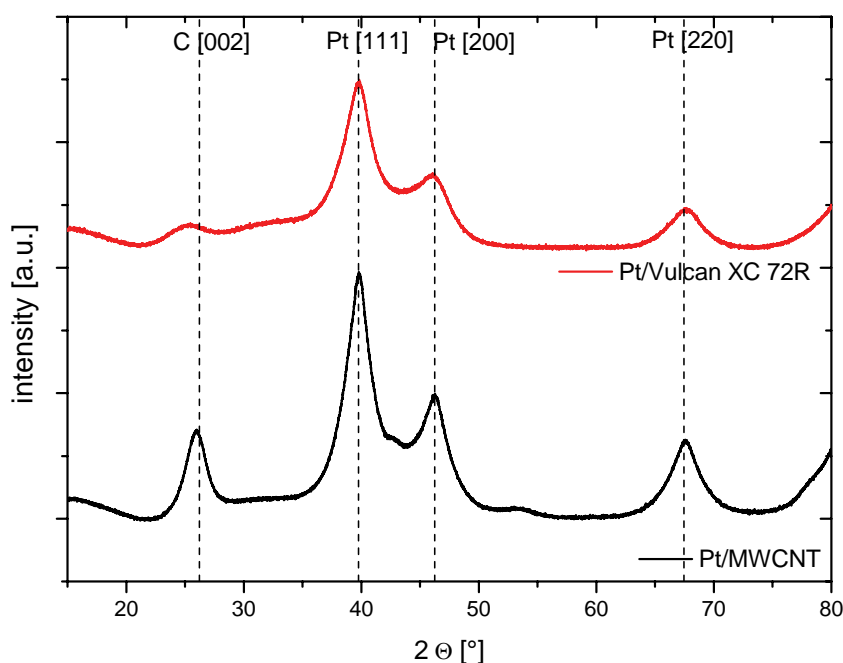


Figure 22 XRD for commercial Pt/Vulcan XC 72R and self made Pt/MWCNT. PDF(Pt)#00-004-0802, PDF(Graphite)#01-075-1621. Reproduced from reference ⁵² by permission of The Royal Society of Chemistry.

The crystallite size of Pt was calculated from the complete XRD pattern using integral breadth method via TOPAS 4-2 (Bruker AXS). The integral breadth method is independent of the distribution in size and shape. Both Pt catalysts exhibit a similar average crystallite size: for Pt/MWCNT 2.3 ± 0.3 nm and for commercial Pt/Vulcan XC 72R 2.1 ± 0.3 nm.

The diffraction profiles show a reflection of ordered graphitic domains in Figure 22, with MWCNT exhibiting a very strong and sharp ordered carbon reflection at $2\theta = 26.0^\circ$, corresponding to large carbon crystallites with a

d-spacing of about 3.424 Å. This is consistent with the (002) diffraction peak of an ideal graphite phase⁸⁷. A second intensive carbon reflection of MWCNT overlaps with the broad (111) and (200) Pt peaks and hence is not clear. The graphitization extent (G) can be determined from the average d_{002} spacing according to

$$\text{eq. 6} \quad (G) = (3.440 - d_{002}) / (3.440 - 3.354)$$

and was estimated to be 19 % for the heat-treated MWCNT at 300 °C for 7 h. The carbon Vulcan XC 72R reveals a broad intensive XRD peak at around 25° and shows as far as no graphitization compared to ideal (002) graphite peak.

Figure 23 displays TEM images of well dispersed platinum nanoparticles on the MWCNT support compared to the commercial Pt/Vulcan XC 72R catalyst. For Pt/MWCNT, the average Pt particle size using TEM was calculated to be 2.9 ± 1.1 nm. Most Pt nanoparticles were distributed on the outside of MWCNTs with an average particle size of 2.9 ± 1.2 nm. Around 12 % of Pt nanoparticles are within the multi walled carbon nanotubes averaging a particle size of 3.1 ± 1.1 nm. The Pt particle size of commercial Pt/Vulcan XC 72R was analyzed to be 2.5 ± 0.6 nm. The TEM particle size results are consistent to crystallite size from the XRD data. TEM technique was used for further determination of particle size distribution after electrochemical experiments, respectively.

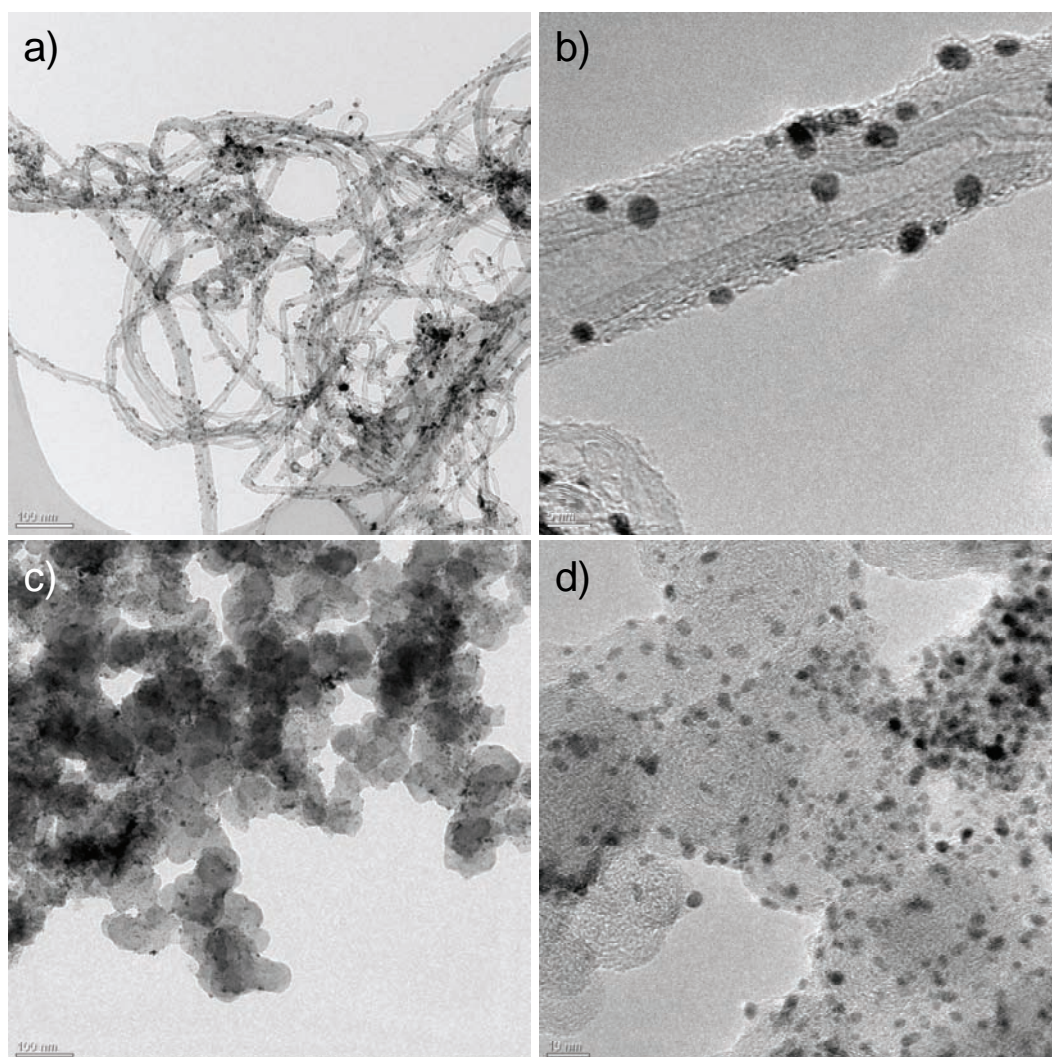


Figure 23 TEM images for Pt/MWCNT after synthesis, a) 100 nm scale, b) 5 nm scale and commercial Pt/Vulcan XC 72R, c) 100 nm scale, d) 10 nm scale. Reproduced from reference ⁵² by permission of The Royal Society of Chemistry.

3.1.2 Stability of Pt/MWCNT in the „lifetime“ and „start-up“ potential cycling regimes

Figure 24 combined with Table 2 and Table 3 (columns 8 – 13) report the evolution of the electrochemical active surface area (ECSA) versus the accumulated potential cycle numbers for the two Pt nanoparticle catalysts in two potential regimes. Figure 24 highlights the normalized N-ECSA values that were calculated according $N\text{-ECSA (cycle \#)} = \text{ECSA (cycle \#)} / \text{ECSA (initial cycle)} * 100 \%$. Table 2 and Table 3 present the absolute initial and final ECSA values of each catalyst.

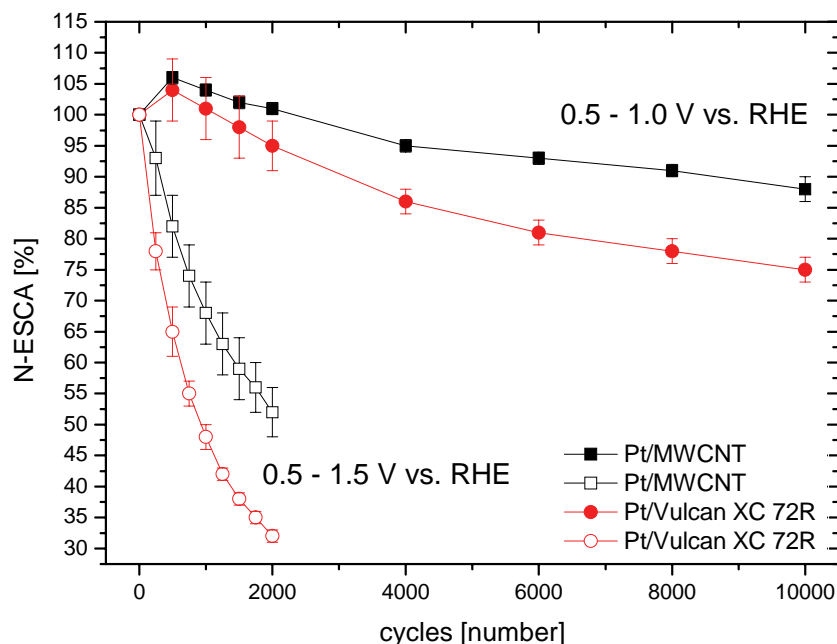


Figure 24 Normalized ECSA loss due to voltage cycling from 0.5 - 1.0 V vs. RHE (solid symbols) and 0.5 - 1.5 V vs. RHE (hollow symbols) with 50 mV s^{-1} for Pt/MWCNT (square) and commercial Pt/Vulcan XC 72R (circular). Reproduced from reference ⁵² by permission of The Royal Society of Chemistry.

Despite the fact that both carbon supports and catalysts started out with comparable BET surface area (Pt/MWCNT $153 \text{ m}^2 \text{ g}^{-1}$ and Pt/Vulcan XC 72R $151 \text{ m}^2 \text{ g}^{-1}$) respectively, Pt/MWCNT catalyst exhibited a significant smaller drop in N-ECSA compared to the commercial Pt/Vulcan XC 72R, suggesting an enhanced improvement in cathode catalyst stability using MWCNT support. Under “lifetime” conditions, N-ECSA values of the Pt/MWCNT dropped a mere 12 % compared to 25 % for Pt/Vulcan XC 72R. Under the more severe “start-up” cycling conditions, the N-ECSA value of Pt/MWCNT dropped off by 48 %, while Pt/Vulcan XC 72R exhibited 68 % decrease. These experimental results are consistent with earlier results and confirm the detrimental nature of electrode potentials above 1.0 V vs. RHE under start/stop and partial fuel starvation conditions^{78, 79, 88-91}. During the first 500 cycles of the “lifetime” testing regime, both Pt/MWCNT and Pt/Vulcan XC 72R catalysts exhibited a characteristic break-in type increase in ECSA and is consistent with earlier reports^{35, 48, 92}. This gain in ECSA can be linked to a temporary enhancement in Pt dispersion by Pt surface atoms or Pt particle rearrangement.

The initial ECSA increase was not observed during “start-up” cycling. This can be account for by the extreme corrosive conditions during the “start-up” regime, where an initial increase in Pt dispersion is impossible due to immediate massive dissolution of the smaller Pt nanoparticles. Thus, they highlight the ECSA benefits of the ordered MWCNT support compared to less ordered carbon black support such as Vulcan XC 72R.

Table 2 Catalyst performance – 10,000 voltage cycles from 0.5 to 1.0 V vs. RHE. Reproduced from reference ⁵² by permission of The Royal Society of Chemistry.

catalyst	$j_{(\text{mass.}, 0.9\text{V [RHE]})}$ [A/mg(Pt)]			$j_{(\text{spec.}, 0.9\text{V [RHE]})}$ [$\mu\text{A}/\text{cm}^2(\text{Pt})$]			ECSA [m^2/g]			N-ECSA ³⁾ [%]			particle size [nm]		
	initial ¹⁾	final ²⁾	Δ [%]	initial ¹⁾	final ²⁾	Δ [%]	initial ¹⁾	final ²⁾	Δ [%]	initial	final ²⁾	Δ [%]	initial	final	Δ [%]
Pt/MWCNT	0.12 ± 0.02	0.11 ± 0.01	-10	263 ± 63	219 ± 13	-17	47 ± 12	49 ± 7	5	100	88 ± 2	-12	2.9 ± 1.1	3.9 ± 1.2	34
Pt/Vulcan XC 72R	0.15 ± 0.02	0.10 ± 0.03	-34	291 ± 40	263 ± 82	-9	53 ± 4	39 ± 4	-26	100	75 ± 2	-25	2.5 ± 0.6	3.6 ± 0.9	44

¹⁾mean value determined from 6 (= 3 start-up + 3 lifetime) independent measurements

²⁾mean value determined from the 3 independent (lifetime) measurements

³⁾N-ECSA = ECSA (final) / ECSA (initial) * 100 %

Table 3 Catalyst performance – 2000 voltage cycles from 0.5 to 1.5 V vs. RHE. Reproduced from reference ⁵² by permission of The Royal Society of Chemistry.

catalyst	$j_{(\text{mass.}, 0.9\text{V [RHE]})}$ [A/mg(Pt)]			$j_{(\text{spec.}, 0.9\text{V [RHE]})}$ [$\mu\text{A}/\text{cm}^2(\text{Pt})$]			ECSA [m^2/g]			N-ECSA ³⁾ [%]			particle size [nm]		
	initial ¹⁾	final ²⁾	Δ [%]	initial ¹⁾	final ²⁾	Δ [%]	initial ¹⁾	final ²⁾	Δ [%]	initial	final ²⁾	Δ [%]	initial	final	Δ [%]
Pt/MWCNT	0.12 ± 0.02	0.05 ± 0.01	-59	263 ± 63	272 ± 109	4	47 ± 12	18 ± 3	-61	100	52 ± 4	-48	2.9 ± 1.1	5.3 ± 1.4	83
Pt/Vulcan XC 72R	0.15 ± 0.02	0.05 ± 0.01	-66	291 ± 40	294 ± 52	1	53 ± 4	18 ± 1	-67	100	32 ± 1	-68	2.5 ± 0.6	5.2 ± 1.5	108

¹⁾mean value determined from 6 (= 3 start-up + 3 lifetime) independent measurements

²⁾mean value determined from the 3 independent (start-up) measurements

³⁾N-ECSA = ECSA (final) / ECSA (initial) * 100 %

3.1.3 Activity of Pt/MWCNT in „lifetime“ and „start-up“ potential regimes

The mass transport corrected oxygen reduction reaction (ORR) activities were established with linear sweep voltammetry (LSV) at 0.90 V vs. RHE at room temperature. The resulting Pt mass and Pt surface area specific activities of Pt/MWCNT and Pt/Vulcan XC 72R catalysts before and after testing under “lifetime” cycling conditions are shown in Table 2. Figure 25 reports the detailed cyclic voltammetry and linear sweep voltammetry measurements of Pt/MWCNT and Pt/Vulcan XC 72R. From Figure 25, a detailed mass activity Tafel plot for both catalysts is provided in Figure 26.

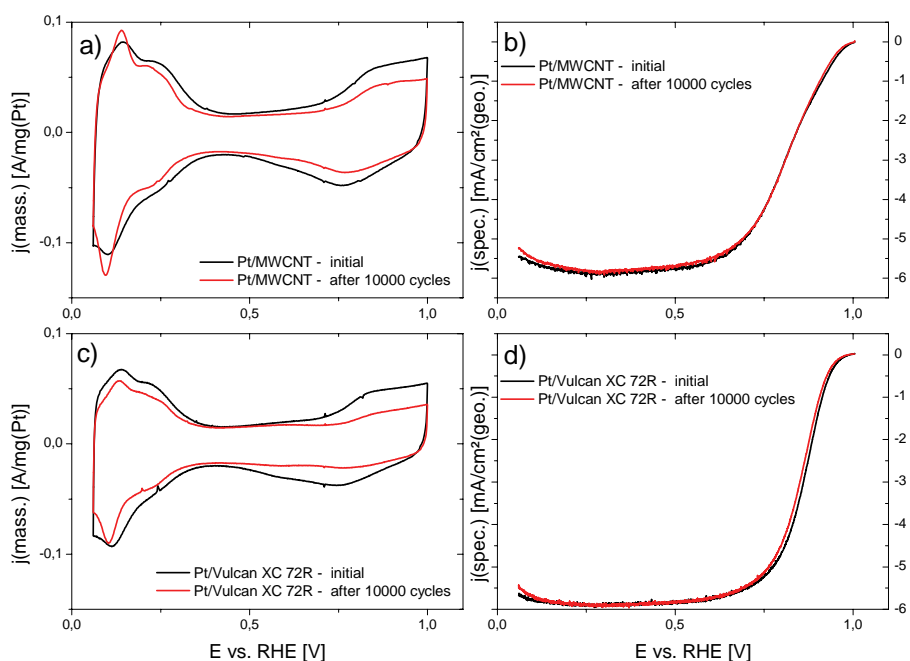


Figure 25 CV for a) Pt/MWCNT, c) Pt/Vulcan XC 72R and LSV for b) Pt/MWCNT, d) Pt/Vulcan XC 72R, 10,000 cycles from 0.5 - 1.0 V vs. RHE with 50 mV s^{-1} (initial – black, final – red). Reproduced from reference ⁵² by permission of The Royal Society of Chemistry.

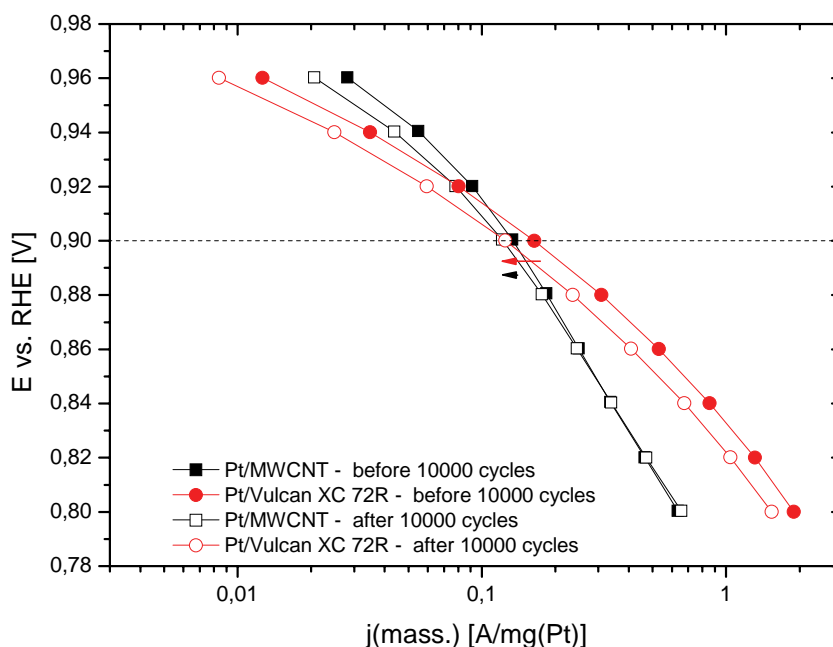


Figure 26 Tafel Plot before (solid symbols) and after (hollow symbols) 10,000 cycles from 0.5 - 1.0 V vs. RHE with 50 mV s^{-1} for Pt/MWCNT (square) and commercial Pt/Vulcan XC 72R (circular). Reproduced from reference ⁵² by permission of The Royal Society of Chemistry.

Initial Pt mass, j_{mass} , ORR activities of both catalysts were around $0.1 \text{ A mg}^{-1}_{\text{Pt}}$ and thus consistent with literature values⁹³; similarly Pt surface area specific, j_{specific} , range around $250 - 300 \mu\text{A cm}^{-2}_{\text{Pt}}$, consistent with literature values⁹³. Our study suggested that MWCNT supports do not enhance the initial Pt mass or Pt specific activity of Pt nanoparticles. After 10,000 “lifetime” potential cycles, the mass activity of Pt/Vulcan XC 72R dropped by 34 %, while that of the Pt/MWCNT only decreased by 10 % to a value of $0.11 \pm 0.01 \text{ A mg}^{-1}_{\text{Pt}}$ at 0.90 V vs. RHE. The Tafel plot revealed that Pt/Vulcan XC 72R exhibited a near-constant shift in the logarithmic activity over the 0.96 V – 0.80 V potential range. MWCNT supports clearly maintain an improved ORR activity over the durability of catalyst electrodes. The Pt mass and Pt surface area specific activities of Pt/MWCNT and Pt/Vulcan XC 72R catalysts before and after testing under “start-up” cycling conditions are shown in Table 3. The activity data in Table 3 were obtained from cyclic voltammetry and linear sweep voltammetry measurements (Figure 27). Detailed mass activity Tafel plots are derived from Figure 27 and provided in Figure 28.

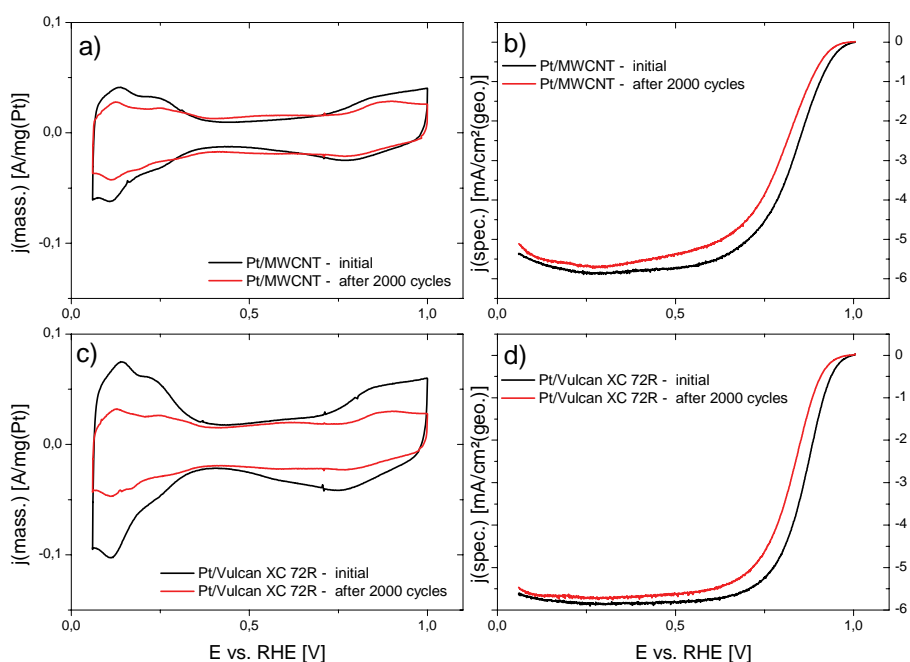


Figure 27 CV for a) Pt/MWCNT, c) Pt/Vulcan XC 72R and LSV for b) Pt/MWCNT, d) Pt/Vulcan XC 72R, 2000 cycles from 0.5 - 1.5 V vs. RHE with 50 mV s^{-1} (initial – black, final – red). Reproduced from reference⁵² by permission of The Royal Society of Chemistry.

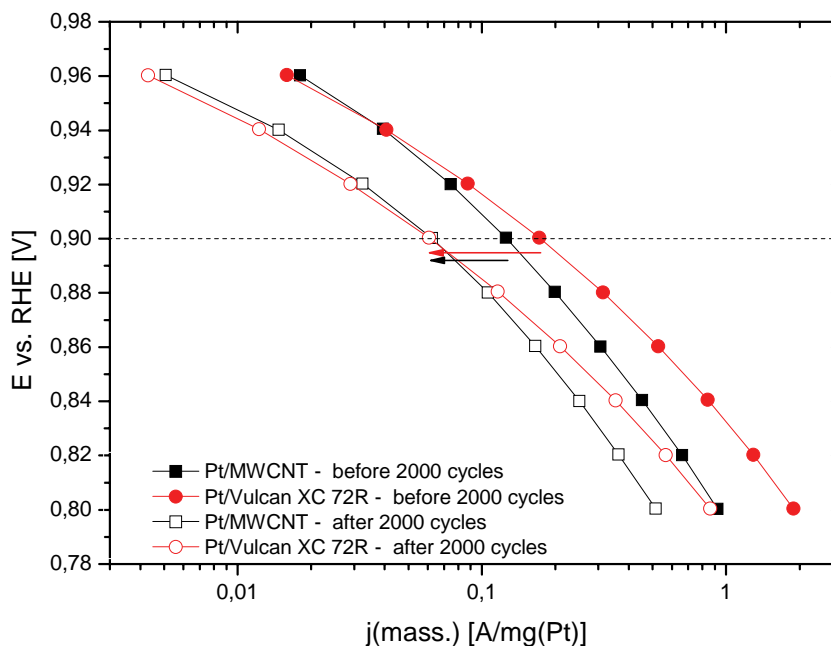


Figure 28 Tafel Plot before (solid symbols) and after (hollow symbols) 2000 cycles from 0.5 - 1.5 V vs. RHE with 50 mV s^{-1} for Pt/MWCNT (square) and commercial Pt/Vulcan XC 72R (circular). Reproduced from reference⁵² by permission of The Royal Society of Chemistry.

Here, the mass activities decreased by 59 % and by 66 % for Pt/MWCNT and Pt/Vulcan XC 72R after 2000 cycles between 0.5 – 1.5 V vs. RHE, respectively, evidencing a superior durability of MWCNT supports even under extremely corrosive cycling conditions. However, the Pt surface area specific ORR activities were essentially constant for both catalysts. The activity analysis clearly revealed that ordered MWCNT supports do not offer initial activity benefits, yet maintain a higher ORR activity even under in extremely corrosive longtime potential cycling.

3.1.4 Correlation of particle growth and ECSA loss mechanisms

Particle size growth mechanisms. Both Pt/carbon catalysts were prepared with virtually identical initial mean particle size of $2.9 \pm 1.1 \text{ nm}$ and $2.5 \pm 0.6 \text{ nm}$ for Pt/MWCNT and Pt/Vulcan XC 72R. After the two potential cycling protocols, the particle size distributions and the mean particle size of Pt were established from TEM images. Figure 29 and Figure 30 show the detailed histograms of the two cycling protocols compared to the particle size distribution before cycling for

Pt/Vulcan XC 72R and Pt/MWCNT, respectively. Over the course of the 10,000 “lifetime” cycles, Pt/Vulcan XC 72R particles grew from 2.5 ± 0.6 to 3.6 ± 0.9 nm, while the MWCNT supported particles coarsened over the same cycling treatment from 2.9 ± 1.1 nm to 3.9 ± 1.2 nm. Under “start-up” conditions Pt/Vulcan XC 72R mean particle size grew to 5.2 ± 1.5 nm, while the Pt/MWCNT particles finally reached 5.3 ± 1.4 nm.

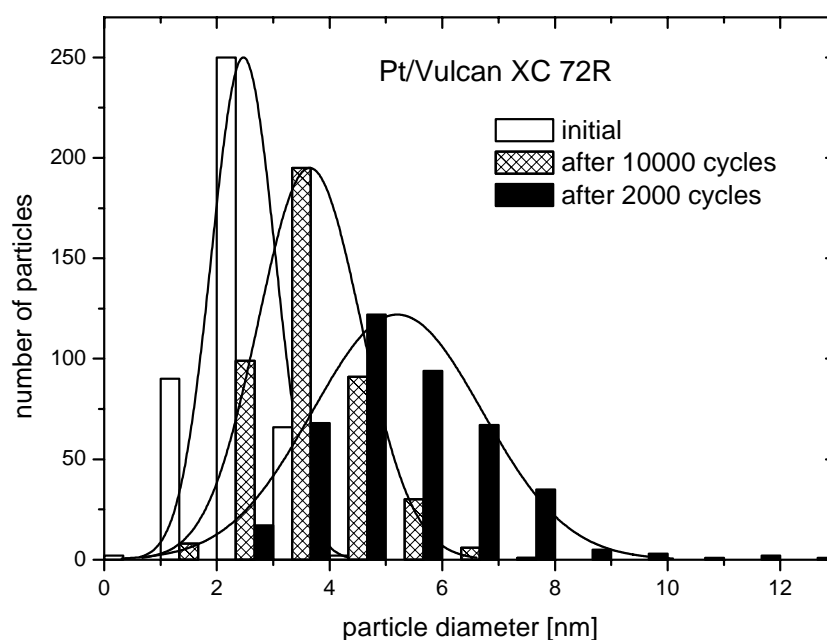


Figure 29 Histograms of particle size distribution for Pt/Vulcan XC 72R before and after electrochemical stability testing (2000 cycles from 0.5 - 1.5 V vs. RHE with 50 mV s^{-1} , 10,000 cycles from 0.5 - 1.0 V vs. RHE with 50 mV s^{-1}). The bar charts are shown with x-offset. Reproduced from reference ⁵² by permission of The Royal Society of Chemistry.

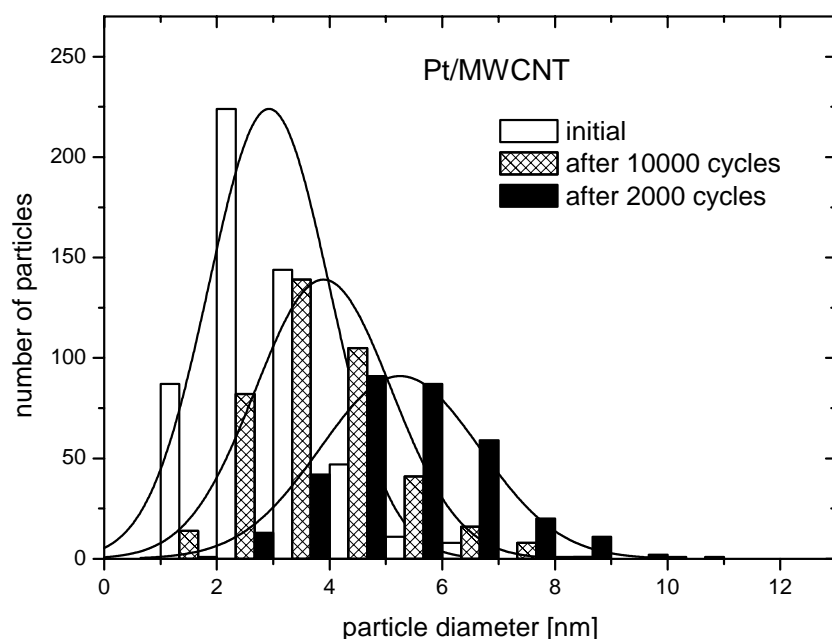


Figure 30 Histograms of particle size distribution for Pt/MWCNT before and after electrochemical stability testing (2000 cycles from 0.5 - 1.5 V vs. RHE with 50 mV s^{-1} , 10,000 cycles from 0.5 - 1.0 V vs. RHE with 50 mV s^{-1}). The bar charts are shown with x-offset. Reproduced from reference ⁵² by permission of The Royal Society of Chemistry.

From the thermodynamic relation between particle dissolution potential E and particle size (eq. 5) a critical particle size (estimate $D_{\text{critical}} = 2 r_{\text{critical}}$) can be obtained, at which Pt particles remain essentially stable under the chosen potential protocol. In contrast, there is no thermodynamically dictated slowdown in growth for coalescence of diffusing neutral metal clusters⁵⁰, atoms or particles⁴⁸ on a surface. Particle coalescence results in particle growth through collisions when particles are moving along the support surface. Under “lifetime” conditions, D_{critical} was computationally predicted to be in the range of 3 – 4 nm^{49, 94}, consistent with our results here. This lends credibility to the model and parameter used in ref. ⁴⁹ and highlights a general dominant role of Ostwald ripening (dissolution of Pt followed by ion migration and redeposition on larger particles) compared to neutral atom/particles migration and coalescence. The experimentally observed final particle size also makes it less likely that a Pt mass loss mechanism⁴⁹ is significantly affecting our measurement. For the “start-up” regime no estimate of D_{critical} was reported in literature, yet our results indicate a value of about 5 – 6 nm. If migration/coalescence of neutral Pt nanoparticles are assumed to be independent of electrode potential, the

experimental fact that $D_{\text{critical}}^{\text{"start-up"}} > D_{\text{critical}}^{\text{"lifetime"}}$ (see Table 2 and Table 3) further corroborates a controlling role of a potential-dependent dissolution/reprecipitation mechanism to account for particle growth. Previous reports⁴⁹ and our own upcoming results⁹⁴ obtained under very similar conditions showed that Pt particle attains their near-stable critical diameter over the course of 1200 cycles or less. We conclude from this that the growth of carbon-supported Pt nanoparticles had approached a critical near-stable mean diameter prior to the completion of the 10,000 cycles of the “lifetime” and the 2000 cycles of the “start-up” regime. We note that in a degradation regime that is based Ostwald ripening (dissolution/reprecipitation) of ions, ion transport processes may also become growth rate controlling, especially at low loadings and high surface areas of the support^{49, 95}.

Even though the electrode potential dependence of the final particle size highlights Ostwald ripening of Pt as the key particle growth mechanism, we propose that under our conditions mobility and coalescence of neutral particle do contribute. We base our proposition on experimental observations presented in Figure 31. Figure 31a (bright field) and Figure 31b (dark field) present a direct TEM observation of a migrating neutral Pt particle during potential cycling on Pt/MWCNT.

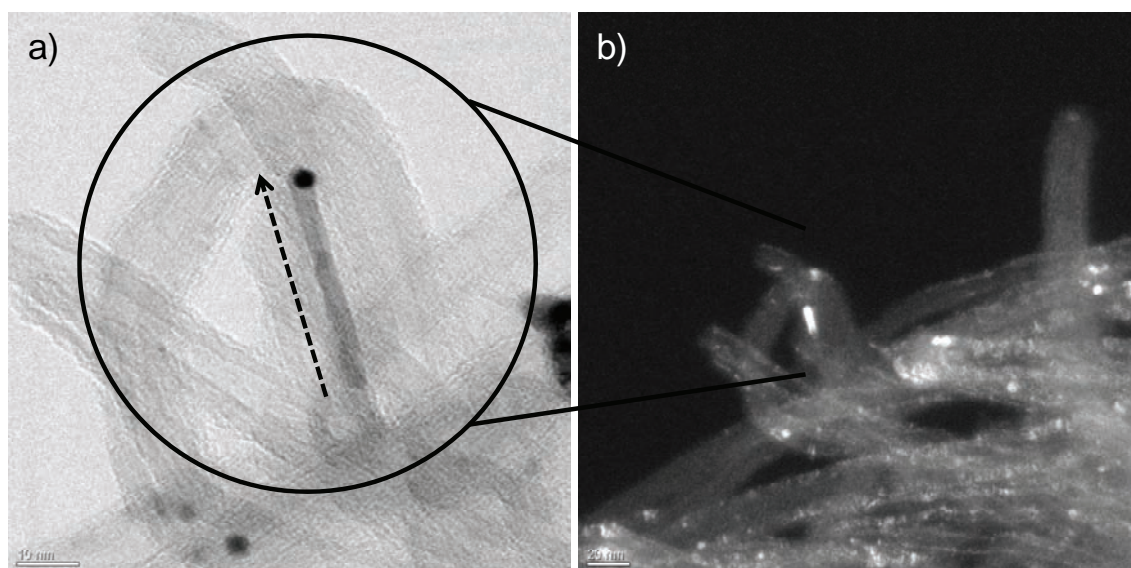


Figure 31 Pt migration within multi walled carbon nanotube – TEM image for Pt/MWCNT after electrochemical “lifetime” potential cycling (0.5 - 1.0 V vs. RHE, 10,000 cycles). a) bright field TEM (10 nm scale), b) dark field TEM (20 nm scale). Reproduced from reference⁵² by permission of The Royal Society of Chemistry.

An individual Pt particle, likely inside a carbon nanotube, migrated over a distance of almost 35 nm, about 10 times its own size, during the cycling protocol. The diffracting electrons of crystalline platinum imaging reveal that during its journey the particle left a atomically thin “sliding” trace of Pt behind, which appears to be coated on the inside of MWCNT. This image evidences a significant mobility of Pt nanoparticles on electrified carbon supports. It further shows that Pt atoms possess a fairly strong interaction with the graphitic carbon sheets. The formation of atomically thin Pt surface layers in the path of migrating Pt nanoparticles constitutes a new mechanism towards highly dispersed Pt, and could, if occurring on a larger scale, at least contribute to a reduced ECSA loss of the MWCNT supported catalysts. In Figure 32, TEM images of Pt/Vulcan XC 72R after electrochemical “lifetime” and “start-up” potential cycling evidence severe particle coarsening.

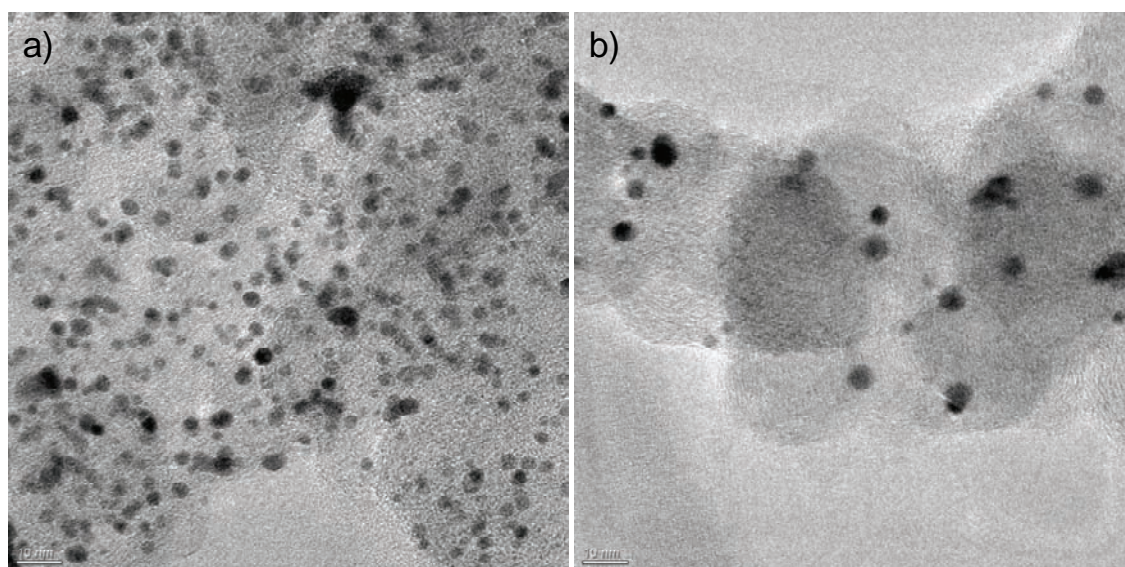


Figure 32 TEM image for commercial Pt/Vulcan XC 72R after electrochemical a) “lifetime” potential cycling (0.5 - 1.0 V vs. RHE, 10,000 cycles, 10 nm scale) and b) “start-up” potential cycling (0.5 - 1.5 V vs. RHE, 2000 cycles, 10 nm scale). Reproduced from reference⁵² by permission of The Royal Society of Chemistry.

Long-term ECSA loss mechanism. We now turn to the experimental ECSA trends in view of the particle size changes. ECSA loss can originate from increases in Pt mean particle size or from a decrease in the number of electrochemically accessible Pt nanoparticles, which, in turn, is controlled by carbon corrosion under particle detachment⁴⁸ or, thirdly, from a net dissolution

of Pt and loss (mass loss mechanism⁴⁹). Considering our conclusions above, the trends in ECSA losses and particle size changes suggests that, in the short term (first few thousand cycles), ECSA losses are related to growth of particles on the carbon support; however, in the longer term, that is, toward the end of the stability test under our conditions, they do not seem to be controlled by particle size. We rather conclude that ECSA losses under our conditions are based on the loss of electrochemically accessible Pt particles via carbon corrosion and detachment, that is mainly a function of the carbon stability. A significant influence of net Pt metal loss can be excluded for the “lifetime” regime based on the upper electrode potential of 1.0 V vs. RHE. A somewhat different picture of catalyst degradation emerges for the “start-up” potential cycling regime (0.5 – 1.5 V vs. RHE). The severely corrosive upper turning potential of 1.5 V vs. RHE resulted in immediate massive carbon corrosion and concomitant Pt dissolution of particles of virtually all sizes. Immediate ECSA loss is the consequence. This could be the reason why no break-in period was present in the experiments. ECSA losses are now likely controlled by Pt dissolution losses into the electrolyte as well as by carbon support corrosion. A quantitative comparison between N-ECSA losses in Table 2, Table 3 and Figure 24 (48 % for Pt/MWCNT and 68 % for Pt/Vulcan XC 72R under “start-up” conditions) demonstrates the stability benefits the ordered, rolled graphene sheets of MWCNT offer under these severe conditions. Here, the enhanced stability of Pt atoms on the rolled graphene sheets may play a significant part in explaining the stability differences.

3.1.5 Conclusions

In this chapter, we have compared the cycling stability (ECSA, particle size) along with the ORR activity of MWCNT and Vulcan XC 72R supported platinum nanoparticle electrocatalysts. We distinguished “lifetime” (0.5 – 1.0 V vs. RHE with 10,000 cycles) conditions and more severe “start-up” cycling conditions (0.5 – 1.5 V vs. RHE with 2000 cycles). From our experimental correlations of particle size, ECSA loss and activity change we concluded, that

- MWCNT support (BET surface area without Pt $192 \text{ m}^2 \text{ g}^{-1}$, with Pt $153 \text{ m}^2 \text{ g}^{-1}$) do not enhance nor are detrimental to the Pt mass or Pt specific ORR activity of Pt nanoparticles in comparison to a commercial Pt/Vulcan XC 72R catalyst with comparable BET surface area.
- MWCNT support exhibit a significantly enhanced cycling durability compared to the Vulcan XC 72R support of comparable BET surface area in both potential regimes.
- Pt particle growth is controlled by Pt dissolution/redeposition (Ostwald ripening) and a critical mean particle diameter D_{critical} is attained over the stability protocol ($D_{\text{critical}}^{\text{“lifetime”}} < D_{\text{critical}}^{\text{“start-up”}}$). Particle growth becomes negligible at D_{critical} for the relevant time scale.
- Carbon corrosion associated with Pt particle detachment controls the ECSA loss of Pt/carbon electrocatalysts for long cycling times after particles have attained D_{critical} . Despite the absence of a Pt ion sink, such as the hydrogen crossover of fuel cell MEA⁴⁹, a net Pt loss mechanism by dissolution of Pt (from essentially all particles) into the electrolyte can not entirely be excluded in the “start-up” regime with potentials up to 1.5 V/ RHE. In the latter case, the experimental quasi-stable mean particle size $D_{\text{critical}}^{\text{“start-up”}}$ (Table 3) is expected to be smaller than the theoretically predicted value.

3.2 Mesoporous nitrogen doped carbon (meso-BMP) supported Pt fuel cell electrocatalyst

This chapter is based on the publication

Hasché, F.; Fellinger, T.-P.; Oezaslan, M.; Paraknowitsch, J. P.;
Antonietti, M.; Strasser, P.

Mesoporous Nitrogen Doped Carbon Supported Platinum PEM Fuel Cell
Electrocatalyst Made From Ionic Liquids

ChemCatChem **2012**, 4, (4), 479-483

<http://dx.doi.org/10.1002/cctc.201100408>

Reproduced by permission of John Wiley and Sons.

The meso-BMP sample was provided from Fellinger, T.-P. (MPIKG Potsdam).

In this chapter we report the synthesis of a mesoporous nitrogen doped carbon supported platinum catalyst (Pt/meso-BMP) based on an ionic liquid as nitrogen/carbon precursor and the evaluation of the catalytic system for the oxygen reduction reaction. Further, we analyze the long-term behavior of this new catalyst and compare it with commercial high surface area carbon (HSAC) supported platinum catalyst.

3.2.1 Synthesis and structural characterization of Pt/meso-BMP

The mesoporous nitrogen doped carbon supported platinum nanoparticle fuel cell electrocatalyst (Pt/meso-BMP) was prepared by a two step synthesis, as shown in Figure 33. In the first step, the mesoporous nitrogen doped carbon material (meso-BMP) was synthesized corresponding to the reference^{96, 97} by using N-butyl-3-methylpyridinedicyanamide (BMP-dca) as ionic liquid compound. As evaluated by X-ray photoelectron spectroscopy (XPS) and elemental analysis (EA) the nitrogen content of 14.2 wt.% (XPS) / 17.17 wt.% (EA) is very high. The variation of the values can be explained by the surface specificity of XPS measurements. In the second step, platinum nanoparticles were deposited on the meso-BMP substrate. The deposition of Pt occurred by a wet impregnation – freeze-drying method and followed by thermal annealing in a reductive atmosphere (more details in chapter 2.2 *Synthesis of Pt/meso-BMP*)^{16, 98, 99}.

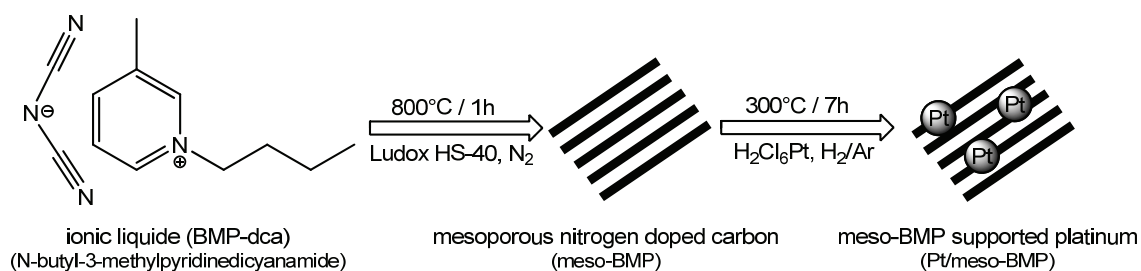


Figure 33 Synthesis route for mesoporous nitrogen doped carbon supported platinum nanoparticle catalyst. Reproduced from reference⁶⁴ by permission of John Wiley and Sons.

Figure 34 shows the XRD profiles for meso-BMP and Pt/meso-BMP. The as synthesized meso-BMP support material exhibits broad XRD reflections at $2\Theta = 26.1^\circ$ and 42.9° corresponding to the inter (002) and intra (101) lattice planes of graphitized carbon.

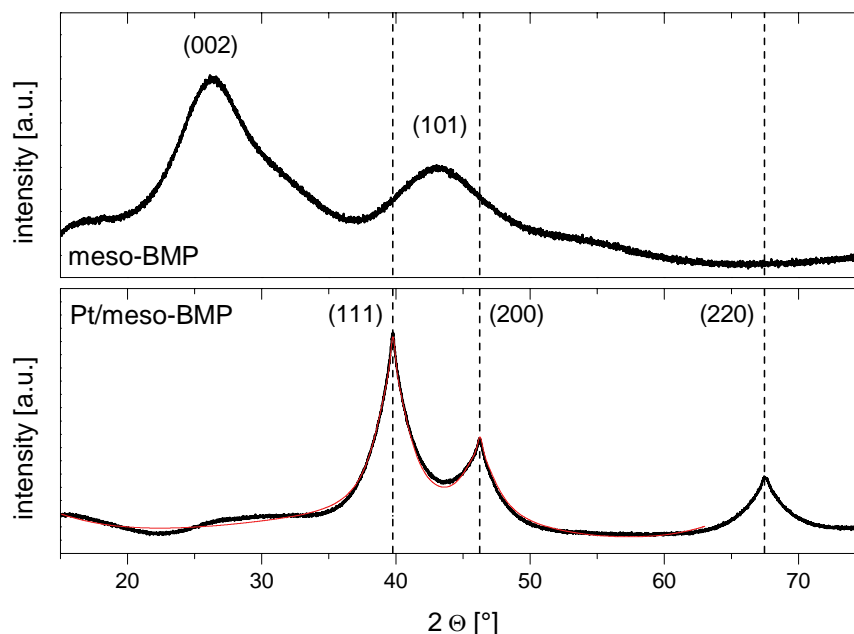


Figure 34 XRD profiles of the meso-BMP support material (top) and Pt/meso-BMP catalyst (bottom) with a Rietveld refinement fit (thin red line). Vertical dotted lines denote reference powder diffraction patterns of pure fcc Pt, PDF(Pt)#00-004-0802⁸⁷. Reproduced from reference ⁶⁴ by permission of John Wiley and Sons.

The reference powder diffraction patterns of (111), (200) and (220) lattice planes for pure face centered cubic (fcc) Pt⁸⁷ are indicated with the vertical dotted lines. The asymmetric shape of the XRD reflections for pure fcc Pt signify different crystallite sizes. According to the Rietveld analysis, Pt nanoparticles show a mean crystallite size of 1.9 ± 0.1 nm as the main crystal phase of 95.9 ± 1.5 wt.%, while the minor crystal phase of 4.1 ± 1.5 wt.% for Pt exhibits a mean crystallite size of 15.2 ± 3.0 nm. This size result conforms excellently to the mean particle size of 2.3 ± 0.6 nm established by transmission electron microscopy (TEM). Figure 35 shows TEM images of the as synthesized Pt/meso-BMP. Here, the established mesoporosity of the nitrogen doped carbon supported Pt material is visible (Figure 35a) as well as the good dispersion of Pt nanoparticles on the support material (Figure 35b).

Mesoporous nitrogen doped carbon (meso-BMP) supported Pt fuel cell electrocatalyst

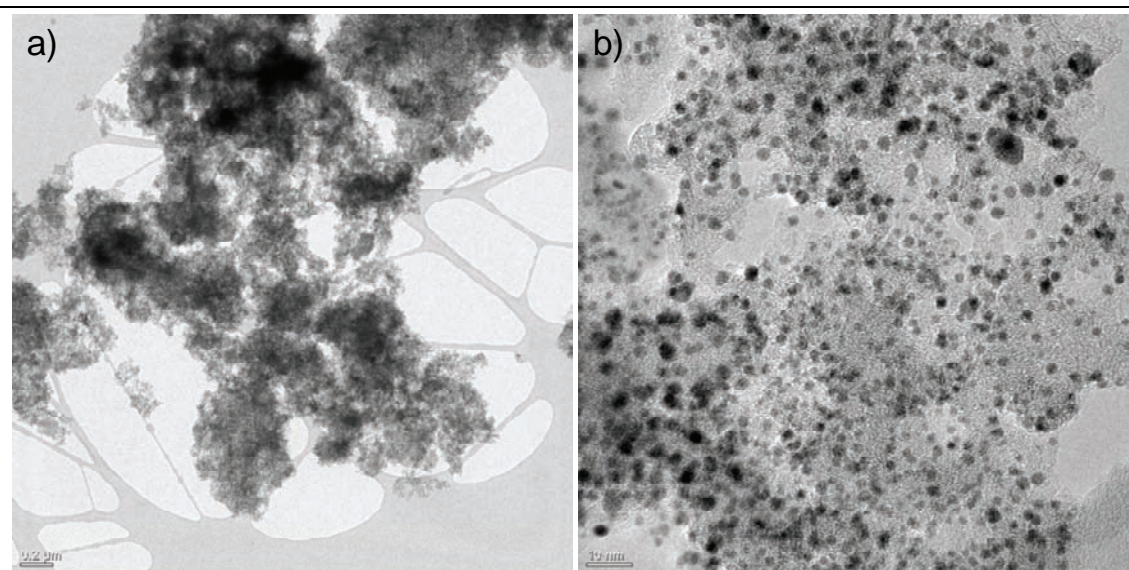


Figure 35 TEM images for the as synthesized Pt/meso-BMP, a) 0.2 μm bar scale, b) 10 nm bar scale. Reproduced from reference⁶⁴ by permission of John Wiley and Sons.

3.2.2 Activity and selectivity of Pt/meso-BMP for oxygen reduction

In the following, we tested the as synthesized Pt/meso-BMP nanoparticle catalyst for the ORR to compare its activity with a benchmark commercial HSAC supported pure Pt nanoparticle catalyst. Figure 36a shows the polarization curves for Pt/meso-BMP at various rotation speeds in oxygenated 0.1 M HClO_4 at room temperature established by rotating disc electrode (RDE) technique to construct a Koutecky – Levich plot, as shown in Figure 36b. All polarization curves exhibited a plateau behavior between 0.06 – 0.60 V vs. RHE, indicating the diffusion controlled regime. The current density increases with increasing rotation speed. Thereby, the oxygen diffusion to the catalytic reaction center is the rate limiting process and in consequence dependent on the rotation rate^{100, 101}. The diffusion controlled regime turns into a mixed diffusion – kinetic controlled region at higher voltages. Finally from about 0.85 V vs. RHE, the reaction rate is only kinetically controlled, as judged by the independence of the rotation rate. At the open circuit potential (around 1.0 V vs. RHE), eventually no electrocatalytic conversion of oxygen was observed.

Mesoporous nitrogen doped carbon (meso-BMP) supported Pt fuel cell electrocatalyst

The selectivity of Pt/meso-BMP for the direct oxygen reduction was established from the Koutecky – Levich plot; the experimental values of Figure 36a were replotted in Figure 36b using the following relationship (eq. 7)

$$\frac{1}{j} = \frac{1}{j_{\text{kinetic}}} + \frac{1}{j_{\text{diffusion}}} = \frac{1}{j_{\text{kinetic}}} + \frac{1}{(B \cdot \omega^{1/2})}$$

eq. 7
$$B = 0.62 \cdot n \cdot F \cdot D(\text{O}_2)^{2/3} \cdot \nu^{-1/6} \cdot c(\text{O}_2)$$

where j , j_{kinetic} and $j_{\text{diffusion}}$ as the current density, kinetic and diffusion limiting current density and ω as the rotation rate. The number of electrons transferred per oxygen molecule can be determined from the Koutecky – Levich slope (B). The so called “B Factor” is dependent on the experimental conditions and allows a comparison with the theoretical value for an ideal direct four electron process of oxygen reduction (eq. 8). Published data were used for the oxygen solubility ($c(\text{O}_2)$), the diffusivity ($D(\text{O}_2)$), the Faraday constant (F) and the kinematic viscosity of the electrolyte (ν)¹⁰².



The experimental “B Factor” was calculated at various voltages from the slope of the Koutecky – Levich Plot (Figure 36b) and is $0.454 \pm 0.012 \text{ mA cm}^{-2}_{\text{geo.}} \text{ s}^{1/2}$. This value is in excellent agreement with the theoretical “B Factor” for a direct four electron process ($0.467 \text{ mA cm}^{-2}_{\text{geo.}} \text{ s}^{1/2}$, deviation < 3%).

Mesoporous nitrogen doped carbon (meso-BMP) supported Pt fuel cell electrocatalyst

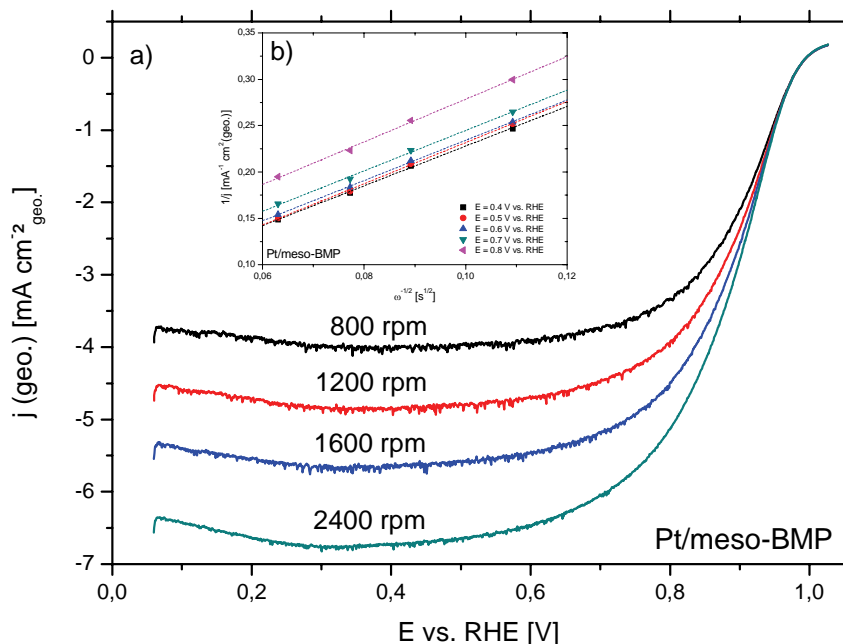


Figure 36 Electrochemical characterization of Pt/meso-BMP, a) polarization curves at various rotation speeds in oxygenated 0.1 M HClO₄, b) Koutecky – Levich plot for oxygen reduction at various voltages. Reproduced from reference⁶⁴ by permission of John Wiley and Sons.

Table 4 summarizes the as synthesized mean particle size, Pt mass based (j_{mass}) and Pt surface area specific based (j_{specific}) activities of Pt/meso-BMP for ORR compared with commercial benchmark pure Pt/HSAC. Pt/meso-BMP shows similar j_{mass} compared with Pt/HSAC by similar particle size and is in good agreement with published values^{52, 93, 103}. With a view to the Pt electrochemically active surface area (ECSA), Pt/meso-BMP exhibits clearly higher ECSA value than Pt/HSAC.

Table 4 Comparison of as synthesized mean particle size, Pt mass and Pt surface area specific based ORR activities for Pt/meso-BMP and Pt/HSAC nanoparticle catalysts. Reproduced from reference⁶⁴ by permission of John Wiley and Sons.

catalyst	mean particle size [nm]	ECSA [m ² g _{Pt} ⁻¹]	$j_{\text{(mass, 0.9 V [RHE])}}$ [A mg _{Pt} ⁻¹]	$j_{\text{(specific, 0.9 V [RHE])}}$ [μA cm _{Pt} ⁻²]
Pt/meso-BMP	2.3 ± 0.6	98 ± 9	0.12 ± 0.03	127 ± 20
Pt/HSAC	2.3 ± 0.7	74 ± 7	0.14 ± 0.01	191 ± 20

3.2.3 Stability of Pt/meso-BMP during voltage cycling

To evaluate whether this ECSA benefit translates in improved stability characteristics, a voltage cycling long-term stability test was performed for Pt/meso-BMP and Pt/HSAC nanoparticle catalysts. The catalysts were subjected to 10000 voltage cycles between 0.5 – 1.0 V vs. RHE with a scan rate of 50 mV s^{-1} in deaerated 0.1 M HClO_4 at room temperature. Such a voltage cycling protocol is an accelerated degradation test to assess the long-term behavior of fuel cell electrocatalysts^{36, 52, 104}. Figure 37 shows the resulted absolute ECSA trends (inset, normalized ECSA trend) for Pt/meso-BMP and Pt/HSAC during the voltage cycling.

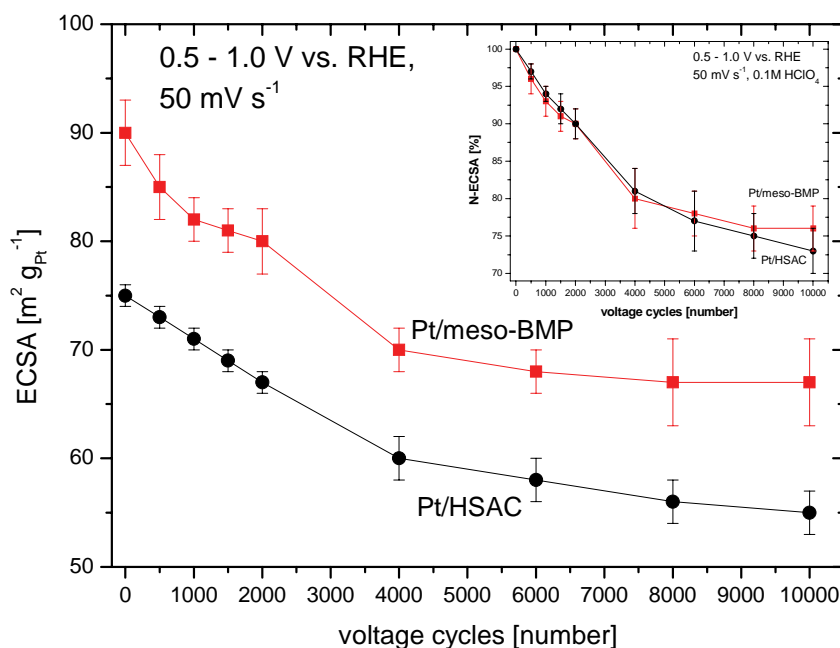


Figure 37 Evolution of the platinum electrochemical active surface area (ECSA) (inset: normalized ECSA trend) for Pt/meso-BMP (red squares) and Pt/HSAC (black circles) during voltage cycling from 0.5 to 1.0 V vs. RHE with 50 mV s^{-1} in deaerated 0.1 M HClO_4 electrolyte at room temperature. Reproduced from reference⁶⁴ by permission of John Wiley and Sons.

The ECSA values for Pt/meso-BMP nanoparticle catalyst are clearly higher than those for Pt/HSAC before and after voltage cycling testing. In results, the ECSA decreased from $90 \pm 3 \text{ m}^2 \text{g}_{\text{Pt}}^{-1}$ to $67 \pm 4 \text{ m}^2 \text{g}_{\text{Pt}}^{-1}$ (-26 %) and $75 \pm 1 \text{ m}^2 \text{g}_{\text{Pt}}^{-1}$ to $55 \pm 2 \text{ m}^2 \text{g}_{\text{Pt}}^{-1}$ (-27 %) for Pt/meso-BMP and Pt/HSAC, respectively. The ECSA loss is associated with mean particle size growth for

Mesoporous nitrogen doped carbon (meso-BMP) supported Pt fuel cell electrocatalyst

Pt/meso-BMP (2.3 ± 0.6 nm to 3.3 ± 0.9 nm) and Pt/HSAC (2.3 ± 0.7 nm to 3.1 ± 0.7 nm) and carbon corrosion. However, the normalized ECSA loss and curve trend is very similar for both Pt catalysts and indicate an equal behavior of degradation for both catalysts (see Figure 37 inset). This corresponds to earlier studies with different carbon supported Pt and Pt alloy nanoparticles, where the ECSA loss curve can be split into two regimes^{36, 52, 104}. In the earlier stage (up to 4000 voltage cycles) particle growth controls primarily the degradation mechanism while in the later stage carbon (support) corrosion associated with particle detachment is dominant.

3.2.4 Conclusions

In conclusion, we have synthesized a novel catalyst type of mesoporous nitrogen doped carbon supported platinum catalyst for the electrocatalytic reduction of oxygen. The new catalyst shows comparable activities like the benchmark commercial fuel cell Pt catalyst. A significantly increased Pt electrochemical active surface area (ECSA) was established compared to the benchmark catalyst. In addition, the increased ECSA of the ionic liquid based mesoporous nitrogen doped carbon supported Pt nanoparticle fuel cell electrocatalyst remained during the long-term stability test compared to a commercial supported Pt electrocatalyst. Further studies are necessary to evaluate and optimize this class of support material which shows promising opportunities for enhanced durability electrocatalysts for fuel cells.

3.3 Silicon carbide derived carbon (CDC) supported Pt fuel cell electrocatalyst

This chapter is based on the publication

Borchardt, L.; Hasché, F.; Lohe, M. R.; Oschatz, M.; Schmidt, F.; Kockrick, E.;
Ziegler, C.; Lescouet, T.; Bachmatiuk, A.; Büchner, B.; Farrusseng, D.;
Strasser, P.; Kaskel, S.

Transition metal loaded silicon carbide-derived carbons
with enhanced catalytic properties

Carbon **2012**, 50, (5), 1861-1870

<http://dx.doi.org/10.1016/j.carbon.2011.12.036>

Reproduced by permission of Elsevier.

The Pt/CDC sample was provided from Borchardt, L. (TU Dresden).

Here, we report on the synthesis and catalyst support applications of a novel silicon carbide derived carbon material. This material class offers high BET surface area, the possibility for controlled doping, high level of graphitization and structured frameworks. As such, it opens a promising prospect to achieve the long-term stability goals in fuel cell cathode catalyst research. We have prepared a silicon carbide derived carbon supported platinum nanoparticle catalysts (here forth referred to as “Pt/CDC”), and have studied its electrocatalytic activity for the oxygen reduction reaction. We find catalytic ORR activities comparable and superior to state of the art Pt/Vulcan XC 72R catalysts involving conventional carbon supports, making CDC a viable alternative catalyst support.

3.3.1 Structural characterization of Pt/CDC

Silicon carbide derived carbon supported platinum catalysts (Pt/CDC) with a platinum loading of 4.45 wt. %, a BET surface area of $1480 \text{ m}^2 \text{ g}^{-1}$ and a platinum average particle size of $2.5 \pm 0.7 \text{ nm}$ established with transmission electron microscopy (TEM) were characterized with respect to their surface voltammetric behavior in supporting acid electrolyte as well as to their electrocatalytic reactivity for the oxygen reduction reaction (ORR) in acidic liquid electrolytes.

The Pt/CDC catalyst exhibits a micropores size of 0.8 nm and a mesopores size of 3.3 nm. The platinum average particle size of well dispersed platinum nanoparticles is around $2.5 \pm 0.7 \text{ nm}$. Here, the obtained BET surface area of $1480 \text{ m}^2 \text{ g}^{-1}$ is around 9 times higher than that for the commercial Vulcan XC 72R. Highly structural CDC support material offer great advantages for the long-term stability over non structural carbons, such as Vulcan XC 72R. Figure 38 shows TEM images of the well defined structured Pt/CDC catalyst (Figure 38a and c) compared with a commercial non structured Pt/Vulcan XC 72R catalyst (Figure 38b and d).

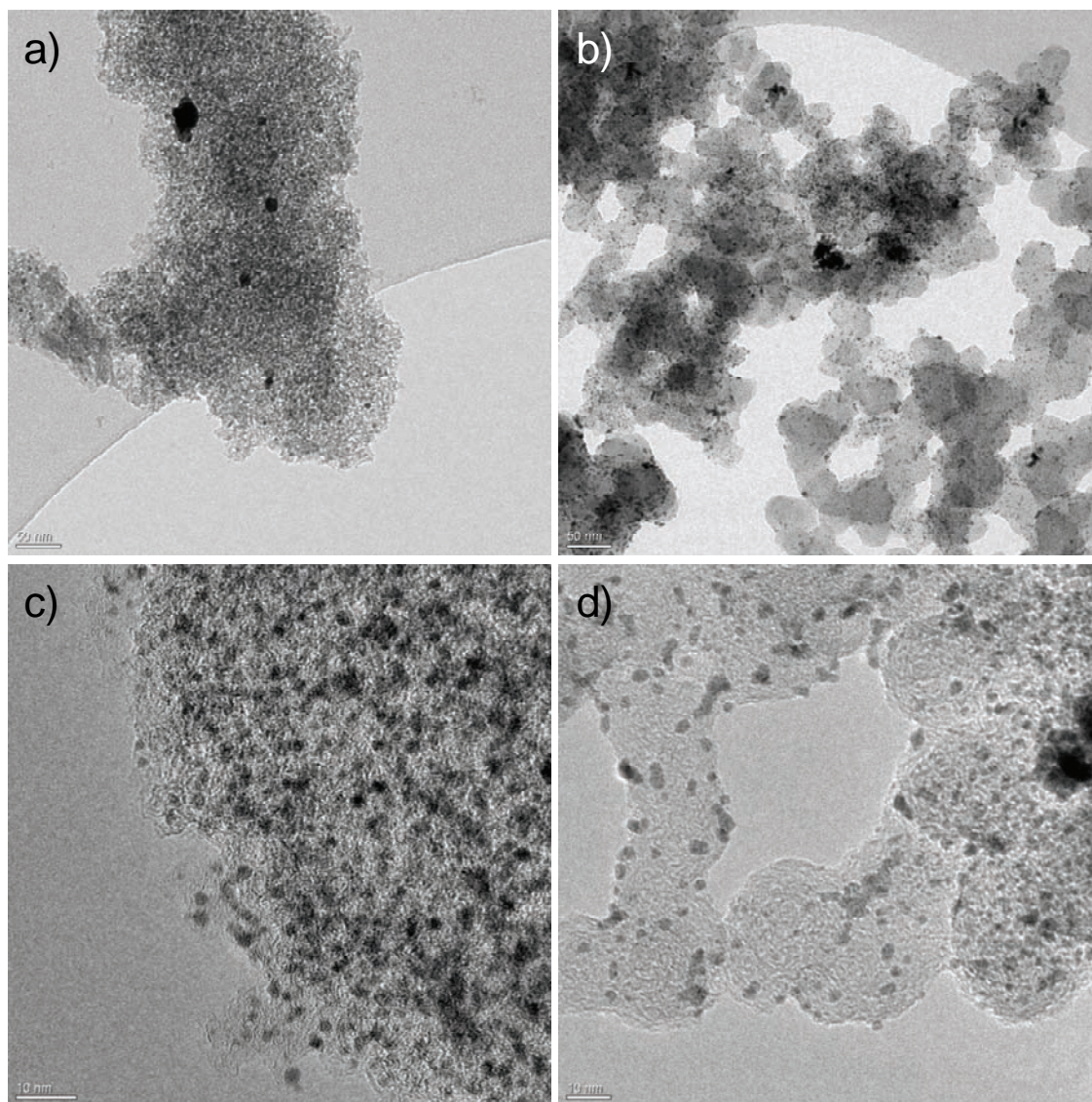


Figure 38 TEM image for Pt/CDC catalyst (a) 50 nm scale, (c) 10 nm scale and commercial Pt/Vulcan XC 72R catalyst (b) 50 nm scale, (d) 10 nm scale. Reproduced from reference ⁶² by permission of Elsevier.

Figure 38a and Figure 38b shows a 50 nm overview. Here, the different carbon structure is well observable. The non structured carbon sheets of the Pt/Vulcan XC 72R catalyst in Figure 38b and the structured framework of the Pt/CDC catalyst in Figure 38a. The well dispersion of platinum nanoparticles for the self made Pt/CDC catalyst is in Figure 38c visible and in a good agreement with the dispersion of the commercial Pt/Vulcan XC 72R catalyst shown in Figure 38d.

3.3.2 Activity and selectivity of Pt/CDC for oxygen reduction

Figure 39 inset shows the cyclic voltammetry (CV) profile for the Pt/CDC catalyst. The Pt/CDC catalyst exhibits a hydrogen absorption/desorption peak in the potential regime between 0.0 – 0.4 V vs. RHE, adjacent to a double layer capacitive current plateau starting at 0.4 V vs. RHE; anodically thereof, the Pt hydroxide/oxide formation region is visible in the potential range of 0.7 – 1.0 V vs. RHE. The electrochemical active surface area (ECSA) was estimated to $66 \pm 4 \text{ m}^2 \text{ g}^{-1}_{\text{Pt}}$ and is consistent with literature values⁹³. This result highlights that the platinum nanoparticles on the mesopores CDC support material are active and available for electrocatalysis.

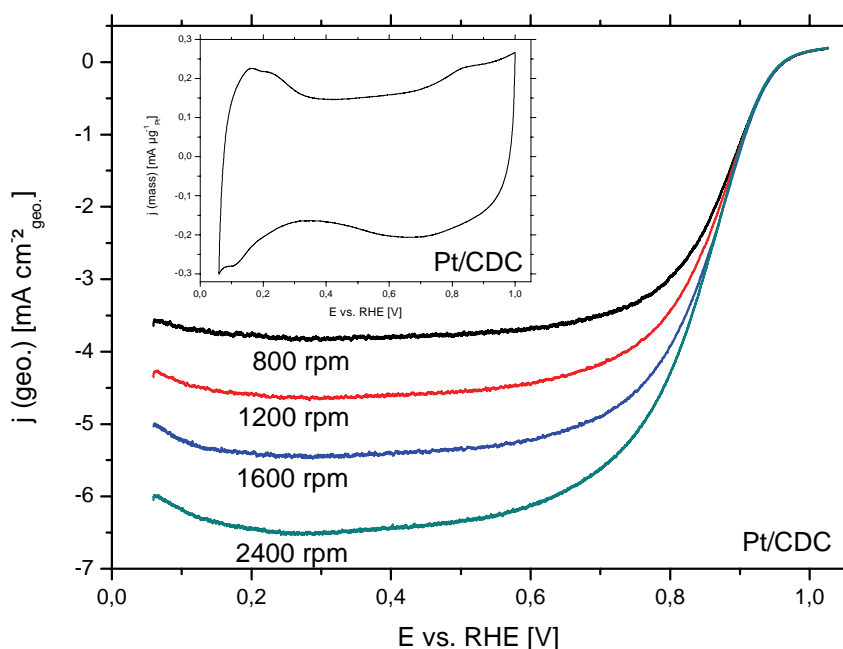


Figure 39 Electrochemical characterization for Pt/CDC catalyst, linear sweep voltammetry (LSV) with different rotating speeds performed anodically from 0.06 - 1.03 V vs. RHE with 5 mV s^{-1} in oxygen saturated 0.1 M HClO_4 at room temperature, inset) cyclic voltammetry (CV) conducted from 0.06 - 1.00 V vs. RHE with 100 mV s^{-1} in deaerated 0.1 M HClO_4 at room temperature. Reproduced from reference⁶² by permission of Elsevier.

Figure 39 shows the oxygen reduction sweep voltammetry curves of the Pt/CDC catalyst at several rotating speeds. All measured polarization curves exhibit a plateau behavior in the potential regime between 0.06 – 0.60 V vs. RHE, where oxygen diffusion to the catalyst surface becomes the rate limiting process^{100, 101} and hence is sensitively dependent on rotation rate.

At and anodic of about 0.70 V vs. RHE, the polarization curves exhibit a reactive regime dominated by mixed kinetic and diffusion control. Past 0.9 V/RHE, the voltammetric profile appears largely kinetically controlled, that is the surface catalysis is the slowest component in the overall reaction process, while mass transport is comparatively fast. This is why the sweeps become independent of the rotating speed. At the open circuit potential of about 0.96 V vs. RHE electrocatalytic conversion of oxygen ceases.

To extract the intrinsic catalytic activity, j_{kinetic} , of the Pt/CDC ORR catalyst, the measured ORR current density, j , in Figure 39 was corrected for mass transport according to

$$\frac{1}{j} = \frac{1}{j_{\text{kinetic}}} + \frac{1}{j_{\text{diffusion}}}$$

eq. 9

where $j_{\text{diffusion}}$ represents the diffusion limited ORR current density obtained from Figure 39 at a given rotation rate. Table 5 reports the platinum mass and surface area specific based activities of the Pt/CDC catalyst and a commercial Pt/Vulcan XC 72R catalyst⁵². Platinum electrochemical active surface area and particle size are reported in Table 5.

Table 5 ORR catalyst performance. Reproduced from reference⁶² by permission of Elsevier.

catalyst	$j_{(\text{mass}, 0.9\text{V}/\text{RHE})}$ [$\text{A mg}^{-1}\text{Pt}$]	$j_{(\text{specific}, 0.9\text{V}/\text{RHE})}$ [$\mu\text{A cm}^{-2}\text{Pt}$]	ECSA [$\text{m}^2\text{g}^{-1}\text{Pt}$]	particle size [nm]
Pt/CDC	0.19 ± 0.01	283 ± 35	66 ± 4	2.5 ± 0.7
Pt/Vulcan XC 72R	0.15 ± 0.02	291 ± 40	53 ± 4	2.5 ± 0.6

The Pt/CDC catalyst exhibited a platinum based ORR mass activity, j_{mass} of $0.19 \pm 0.01 \text{ A mg}^{-1}\text{Pt}$ at 0.90 V vs. RHE and a platinum surface area based (specific) activity of j_{specific} , $283 \pm 35 \mu\text{A cm}^{-2}\text{Pt}$ at 0.90 V vs. RHE. Clearly, our Pt/CDC catalyst with its low platinum loading and high BET surface area shows favorable ORR performance and is in line with reported⁹³ Pt mass and specific activities of commercial platinum catalysts supported on conventional Vulcan XC 72R or multi walled carbon nanotubes⁵². Thus, our study suggests that CDC supports are viable fuel cell catalyst supports that are capable to realize the full activity of nanoparticles.

In order to determine the number of transferred electrons during the oxygen reduction, we used the Koutecky – Levich equation^{100, 101} (eq. 10).

$$\frac{1}{j} = \frac{1}{j_{\text{kinetic}}} + \frac{1}{j_{\text{diffusion}}} = \frac{1}{j_{\text{kinetic}}} + \frac{1}{(B \cdot \omega^{1/2})}$$

eq. 10
$$B = 0.62 \cdot n \cdot F \cdot D(\text{O}_2)^{2/3} \cdot \nu^{-1/6} \cdot c(\text{O}_2)$$

Here, j is the current density, j_{kinetic} the kinetic current density, $j_{\text{diffusion}}$ the diffusion limiting current density, ω the rotating speed, F the Faraday constant ($F = 96485 \text{ C mol}^{-1}$) and B is a parameter dependent on the experimental conditions. A theoretical value for B (eq.5) of $0.467 \text{ mA cm}^{-2}_{\text{geo.}} \text{ s}^{1/2}$ was predicted for the four electron oxygen reduction process using published data⁷ for oxygen solubility ($c(\text{O}_2) = 1.26 \cdot 10^{-3} \text{ mol l}^{-1}$), oxygen diffusivity ($D(\text{O}_2) = 1.93 \cdot 10^{-5} \text{ cm}^2 \text{ s}^{-1}$) and kinematic viscosity of electrolyte ($\nu = 1.009 \cdot 10^{-2} \text{ cm}^2 \text{ s}^{-1}$). We then extracted the value of B specific to our experiments using a Koutecky – Levich plot for the Pt/CDC catalyst at various potentials (see Figure 40).

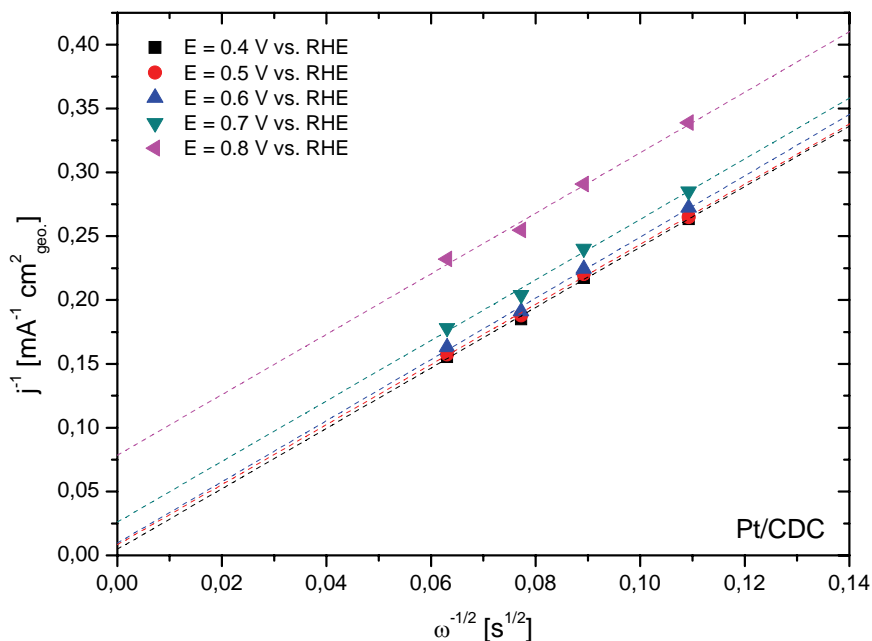


Figure 40 Koutecky - Levich plot for Pt/CDC catalyst at various potentials, data taken from Figure 39. Reproduced from reference⁶² by permission of Elsevier.

The plot of $1/j$ vs. $\omega^{-1/2}$ is linear and the fits run parallel, indicating a similar slope for various electrode potentials. The experimentally extracted mean B value for the various electrode potentials was $0.422 \pm 0.003 \text{ mA cm}^{-2}_{\text{geo.}} \text{ s}^{1/2}$.

The good agreement of the theoretical and experimental value of B corroborates the prevalence of the four electron over the two electron catalytic reduction pathway.

3.3.3 Conclusions

The Pt nanoparticle electrocatalyst supported on a novel family of silicon carbide derived carbon offered a highly structured support architecture to accommodate highly dispersed and homogeneously arranged Pt nanoparticles. From the structural characteristics and the ORR electrocatalytic performance measurements we concluded

- that the novel class of silicon carbide derived carbon is a viable alternative support material for fuel cell cathode catalysts,
- that the observed Pt mass and specific activities, as well as, the electrochemical active surface area are all in line with those for commercial Pt/carbon catalysts with conventional carbon materials.
- that the experimental determined B value suggests a four electron reduction pathway for the reduction of oxygen.
- that the high BET surface area and ordered framework of the silicon carbide derived carbons offer great advantages for the long-term stability and corrosion resistance.

3.4 Overview – support effects

Figure 41 shows an overview of TEM images of various supported Pt nanoparticle catalysts, which were evaluated for the reduction of oxygen to water. The various support materials clearly differ in terms of their structure for example tubes (MWCNT), mesoporosity (meso-BMP, CDC) or carbon sheets (Vulcan XC 72R).

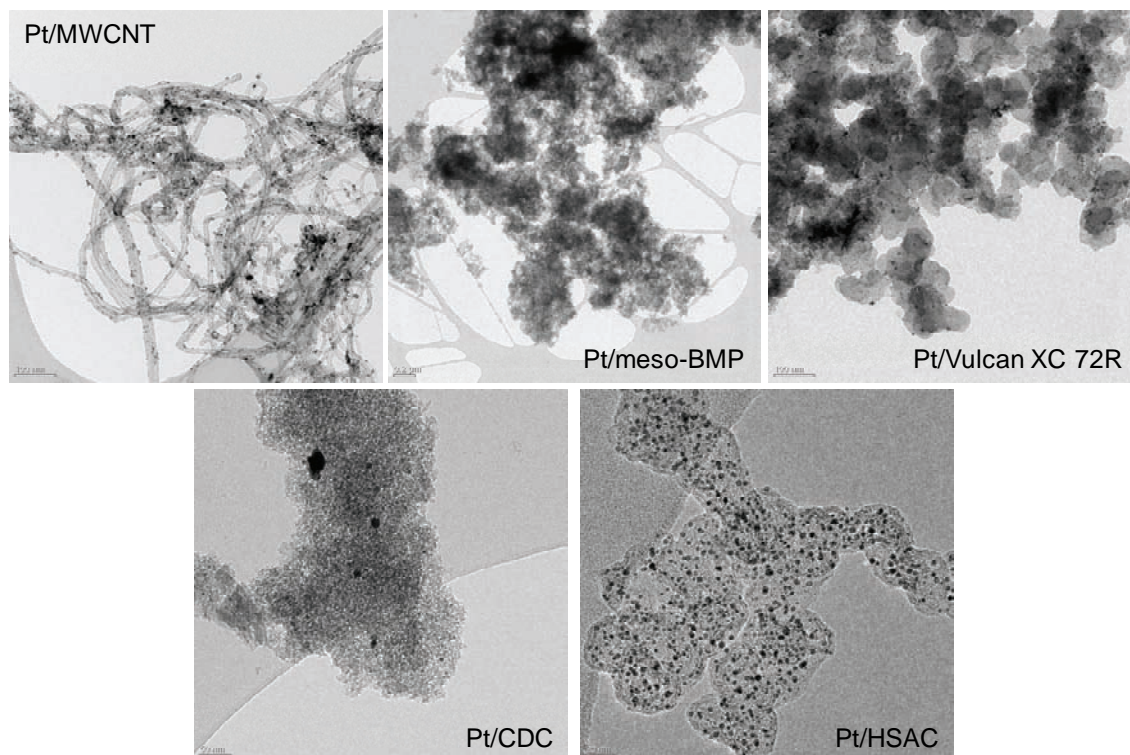


Figure 41 Overview of TEM images of supported Pt nanoparticle catalysts.

The corresponding XRD profiles are shown in Figure 42. Here, the Pt/MWCNT catalyst shows a significant diffraction peak at $2\theta = 26^\circ$ indicating the presence of an ideal (002) graphite phase⁸⁷ and confirms the high level of graphitization. All other catalysts show the absence of this reflection of an ideal (002) graphite phase⁸⁷. The (111), (200) and (220) reflections for pure fcc platinum⁸⁷ are denoted with vertical dotted lines. The broad reflections for platinum indicate a small crystallite size.

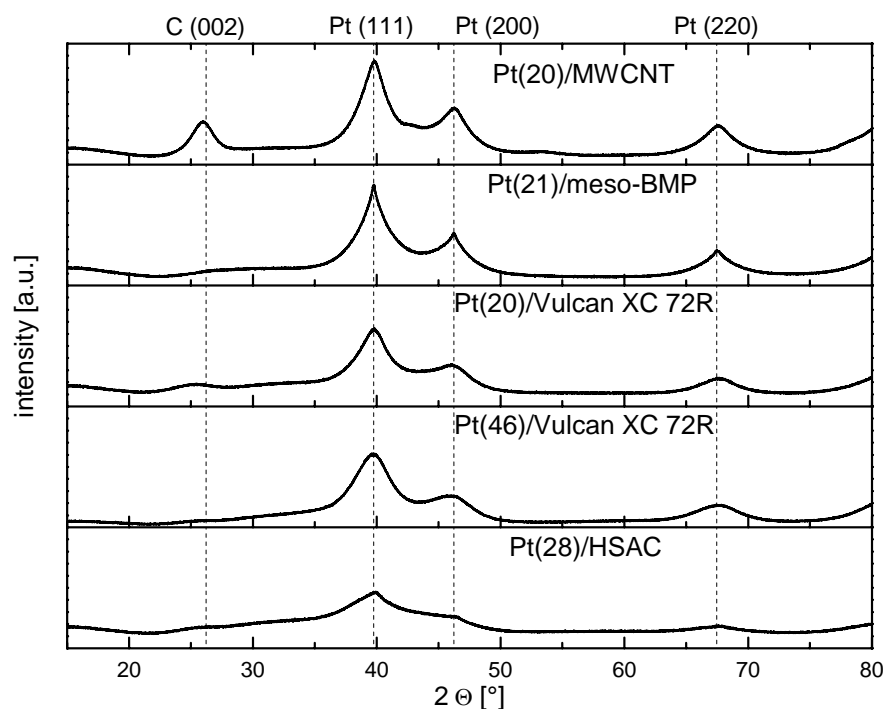


Figure 42 Overview of XRD profiles of supported Pt nanoparticle catalysts.

Table 6 gives an overview of the various characterized Pt supported catalysts. All supported Pt catalysts exhibit a similar mean particle size (Table 6, column 6) of around 2 – 3 nm. However, the Pt loading and BET surface area vary between 5 wt.% to 46 wt.% (Table 6, column 2) and $99 \text{ m}^2 \text{ g}^{-1}$ to $1480 \text{ m}^2 \text{ g}^{-1}$ (Table 6, column 7), respectively. All presented catalysts were tested for the oxygen reduction. The Pt mass based (j_{mass}) and Pt surface area specific based (j_{specific}) activities as well as the Pt electrochemical active surface area (ECSA) are comparable for all supported Pt nanoparticle catalysts. Due to the similar mean particle size, a particle size effect^{53, 105, 106} can be excluded.

Table 6 Overview of supported Pt nanoparticle catalysts: Pt loading, Pt mass based (j_{mass}) and Pt surface area specific (j_{specific}) based ORR activities, Pt electrochemical active surface area (ECSA) and mean particle size determined by TEM.

catalyst	Pt loading [wt.%]	$j_{\text{(mass, 0.9V [RHE])}}$ [A mg ⁻¹ _{Pd}]	$j_{\text{(specific, 0.9V [RHE])}}$ [μA cm ⁻² _{Pd}]	ECSA [m ² g ⁻¹ _{Pd}]	particle size _(TEM) [nm]	surface area _(BET) [m ² g ⁻¹]
Pt/MWCNT	20	0.12 ± 0.02	263 ± 63	47 ± 12	2.9 ± 1.1	153
Pt/meso-BMP	21	0.12 ± 0.03	127 ± 20	98 ± 9	2.3 ± 0.6	247
Pt/Vulcan XC 72R	20	0.15 ± 0.02	291 ± 40	53 ± 4	2.5 ± 0.6	151
Pt/Vulcan XC 72R	46	0.13 ± 0.02	271 ± 30	47 ± 3	2.3 ± 0.6	99
Pt/CDC	5	0.19 ± 0.01	283 ± 35	66 ± 4	2.5 ± 0.7	1480
Pt/HSAC	28	0.14 ± 0.01	191 ± 20	74 ± 7	2.3 ± 0.7	400

In conclusion, all materials showed state of the art activities⁹³ and are therefore suitable as supports for Pt nanoparticles. An explicit Pt mass based activity, BET surface area or Pt loading benefit for a support material class is not observed. Only an increased ECSA value for Pt/meso-BMP was observed and suggests a positive effect of mesoporosity and nitrogen doping for the dispersion of Pt nanoparticles on the support surface.

Table 7 summarizes the results of the “lifetime” voltage cycling test up to 1.0 V vs. RHE. The ECSA loss for all tested catalysts is similar, except for the Pt/MWNCT catalyst, for which a reduced ECSA loss was observed. Furthermore, the final mean particle size (3 – 4 nm) is in the same range for all tested catalysts, indicating a similar particle growth behavior during “lifetime” voltage cycling and an independence of the support material. Only the catalyst with the high Pt loading (46 wt.%) shows a slight increased final mean particle size related to the high metal loading. An effect of the BET surface area for the stability in this voltage regime can be excluded.

Table 7 Overview: Pt loading, ECSA loss and final particle size of supported Pt nanoparticle catalysts after „lifetime“ stability testing.

catalyst	Pt loading [wt.%]	ECSA loss ^[a] [%]	particle size ^[a] _(TEM) [nm]
Pt/MWCNT	20	12	3.9 ± 1.2
Pt/meso-BMP	21	26	3.3 ± 0.9
Pt/Vulcan XC 72R	20	26	3.6 ± 0.9
Pt/Vulcan XC 72R	46	20	4.3 ± 1.2
Pt/HSAC	28	27	3.1 ± 0.7

^[a] after “lifetime” voltage cycling test, 10000 cycles, 0.5 – 1.0 V vs. RHE, 50 mV s⁻¹, 0.1 M HClO₄, room temperature

In conclusion, the level of graphitization of the support material is essential to reduce the ECSA loss during voltage cycling. The ECSA loss and final mean particle size of supported Pt nanoparticles is independent of the BET surface area.

4 Activity, stability, and degradation of Pt alloy fuel cell electrocatalysts: catalytically active component

In this chapter the activity, stability, and degradation of several Pt alloy nanoparticle catalysts were investigated and compared with commercial benchmark pure Pt nanoparticle catalysts. It's addressed the question, how does the catalytically active component influence the stability and activity of PEM fuel cell cathode catalysts?

Therefore, in chapter *4.1 Activity, stability, and degradation mechanisms of dealloyed PtCu₃ and PtCo₃ nanoparticle fuel cell catalysts* an ECSA loss and life cycle degradation model is developed and presented. To confirm this model, in chapter *4.2 Activity, structure and degradation of dealloyed PtNi₃ nanoparticle fuel cell electrocatalyst* a highly active Pt alloy nanoparticle catalyst was synthesized and for oxygen reduction evaluated.

4.1 Activity, stability, and degradation mechanisms of dealloyed PtCu₃ and PtCo₃ nanoparticle fuel cell catalysts

This chapter is based on the publication

Hasché, F.; Oezaslan, M.; Strasser, P.,

Activity, Stability, and Degradation Mechanisms of Dealloyed PtCu₃ and PtCo₃ Nanoparticle Fuel Cell Catalysts.

ChemCatChem **2011**, 3, (11), 1805-1813

<http://dx.doi.org/10.1002/cctc.201100169>

Reproduced by permission of John Wiley and Sons.

In this chapter we correlate key macroscopic and microscopic descriptors of electrocatalyst stability, such as ECSA, ORR performance, chemical composition, and nanoparticle size for dealloyed PtCu₃ and PtCo₃ and benchmark them to a commercial Pt catalyst. We compare and determine changes before, during and after voltage cycling tests in the two distinct regimes (“lifetime” and “start-up”, see 2.6.5 *Electrochemical long-term durability experiments*) to obtain more insight in the dominant catalyst degradation mechanisms. The results highlight a significant activity and stability benefits of dealloyed PtCu₃ and PtCo₃ for ORR compared to pure Pt. In particular, after testing in the “lifetime” regime, Pt surface area based activity of the Pt alloy catalysts is still two times higher than that for pure Pt. From our electrochemical, morphological and compositional results, we provide a general picture of the temporal sequence of dominant degradation mechanisms of a Pt alloy catalyst during its life cycle. We conclude that particle growth and coarsening is the dominant short-term degradation mechanism of Pt and Pt alloys until a critical (quasi stable) particle size, D_{critical} , is arrived. At later stages, carbon corrosion associated with particle detachment become dominant. Predominantly under corrosive “start-up” voltage cycling condition the Pt and base metal dissolution as well as net loss into the electrolyte play a parallel dominant role as carbon corrosion.

4.1.1 Structural characterization of PtCu₃, PtCo₃ and Pt nanoparticles

The X-ray diffraction (XRD) profiles of the synthesized high surface area carbon (HSAC) supported Pt-Cu and Pt-Co alloy nanoparticles in atomic ratio 1:3 (more details in chapter 2.3 *Synthesis of PtCu₃/HSAC and PtCo₃/HSAC*) and the commercial untreated pure Pt/HSAC are shown in Figure 43. The vertical dotted lines in Figure 43 indicate the reference powder diffraction patterns (PDF) of (111), (200), and (220) reflections for pure platinum (black), copper (red) and cobalt (blue) with a face centered cubic (fcc) Fm3m space group⁸⁷.

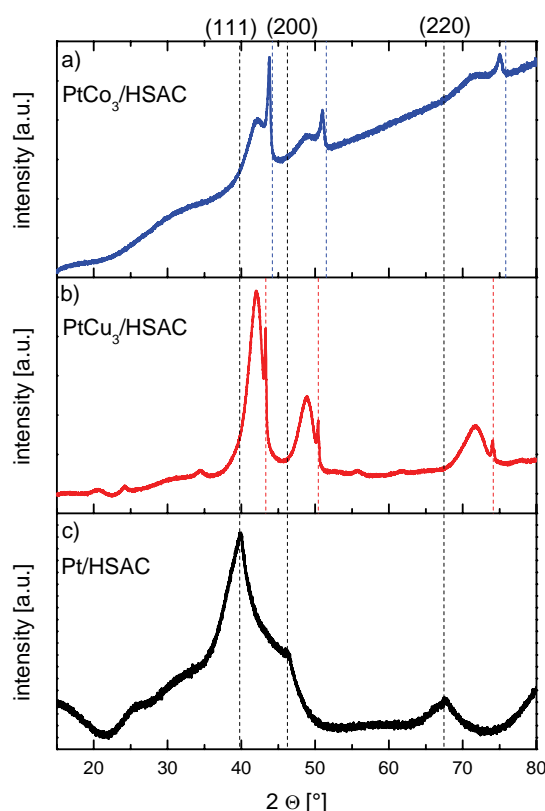


Figure 43 XRD profiles for (a) PtCo₃/HSAC catalyst, (b) PtCu₃/HSAC catalyst and (c) pure Pt/HSAC catalyst. Vertical dotted lines denote reference powder diffraction patterns (PDF) of pure fcc Pt (black), Cu (red) and Co (blue). PDF(Pt)#00-004-0802, PDF(Cu)#00-004-0836, PDF(Co)#00-015-0806⁸⁷. Reproduced from reference³⁶ by permission of John Wiley and Sons.

For PtCo₃/HSAC (Figure 43a) and PtCu₃/HSAC (Figure 43b) the Pt alloys exhibit multiple crystal phases. The (111), (200), and (220) reflections of the alloys were shifted to higher 2θ angles with respect to pure platinum, which

Activity, stability, and degradation mechanisms of dealloyed PtCu₃ and PtCo₃ nanoparticle fuel cell catalysts

indicated the contraction of the lattice by inserting of cobalt or copper in the fcc platinum lattice. No reflections of residual pure fcc platinum phase were found for the Pt alloys. The Pt-Cu alloy sample shows a pure fcc copper phase with sharp reflections at $2\Theta = 43.3^\circ$, 50.4° and 74.1° , indicating a large crystallite size, whereas no pure cobalt was detected for the Pt-Co alloy. As shown in Figure 43c, the broad reflections of pure fcc Pt/HSAC catalyst at $2\Theta = 39.8^\circ$, 46.2° and 67.5° show small crystallite size. The quantification by Rietveld refinement of the Pt alloy crystal phase structures is published in reference¹⁵.

To investigate the mean particle size and chemical composition of the Pt alloy nanoparticle catalysts before and after electrochemical testing, we used transmission electron microscopy (TEM) and energy dispersion X-ray spectroscopy (EDS). The results are summarized in Table 8. Here, the notation “initial” denotes the active dealloyed Pt alloy catalysts with core – shell nanostructure after electrochemical treatment, described in the chapter 2.6.6 *Electrochemical dealloying procedure*.

Table 8 Mean particle size and chemical composition for Pt/HSAC, PtCu₃/HSAC and PtCo₃/HSAC catalysts before and after electrochemical stability testing. Reproduced from reference³⁶ by permission of John Wiley and Sons.

catalyst	mean particle size via TEM [nm]					chemical composition via EDS [at.%]			
	as synthesized	10,000 cycles	Δ [%]	2,000 cycles	Δ [%]	as synthesized	initial	10,000 cycles	2,000 cycles
Pt/HSAC	2.3 ± 0.7	3.1 ± 0.7	+35	5.6 ± 1.5	+144	Pt ₁₀₀	Pt ₁₀₀	Pt ₁₀₀	Pt ₁₀₀
PtCu ₃ /HSAC	4.3 ± 1.6	4.4 ± 1.6	+2	6.8 ± 2.2	+58	Pt _{34±1} Cu _{66±1}	Pt _{63±2} Cu _{37±2}	Pt _{66±4} Cu _{34±4}	Pt _{91±3} Cu _{9±3}
PtCo ₃ /HSAC	4.0 ± 1.0	4.6 ± 1.8	+15	7.0 ± 2.8	+75	Pt _{37±2} Co _{63±2}	Pt _{80±2} Co _{20±2}	Pt _{83±3} Co _{17±3}	Pt _{94±2} Co _{6±2}

The mean particle size for the synthesized PtCu₃/HSAC and PtCo₃/HSAC nanoparticle catalysts is 4.3 ± 1.6 nm and 4.0 ± 1.0 nm, obtained from the evolution of TEM images by counting for more than 400 particles. Both Pt alloy catalysts exhibit a similar mean particle size after the thermal treatment, which rules out the stability benefit through the initial particle size. For the commercial untreated pure Pt/HSAC nanoparticle catalyst the mean particle size is 2.3 ± 0.7 nm. The difference in the mean particle sizes between the pure Pt/HSAC and Pt bimetallic alloy catalysts is caused by annealing at 800 °C for 7 hours for the alloy formation^{15, 27}.

We established the chemical composition of the Pt-Cu and Pt-Co alloy nanoparticles using EDS. Table 8 shows the as synthesized composition with the desired atomic ratio of platinum to metal from 1:3, Pt_{34±1}Cu_{66±1} and Pt_{37±2}Co_{63±2}. After an identical electrochemical dealloying protocol, the initial chemical composition of the dealloyed Pt-Cu and Pt-Co alloy nanoparticles changed drastically because of the dissolution of the non noble metal (copper or cobalt) from the particle surface. In according to earlier studies, we suppose the formation of highly active core – shell nanoparticles with platinum enriched shell and copper / cobalt enriched alloy core^{13-16, 35}. Finally, the initial chemical composition of the (dealloyed) core – shell bimetallic nanoparticles was Pt_{63±2}Cu_{37±2} and Pt_{80±2}Co_{20±2}. The fraction of removed cobalt in the Pt alloy nanoparticles was significantly higher than that for copper, which is in line with the relative dissolution potentials.

4.1.2 Activity and stability of Pt and Pt alloy nanoparticle catalysts in “lifetime” and “start-up” voltage cycling regimes

Table 9 summarizes the mass transport corrected activities of Pt/HSAC, PtCu₃/HSAC and PtCo₃/HSAC nanoparticle catalysts for the oxygen reduction reaction (ORR) before and after the electrochemical stability testing. From the linear sweep voltammetry (LSV) curves the intrinsic kinetic current for each initial catalyst was estimated at 0.9 V vs. RHE at room temperature. Here, j_{mass} , is the platinum mass based activity and j_{specific} is the platinum surface area specific based activity for ORR. Altogether, dealloyed PtCu₃/HSAC and PtCo₃/HSAC nanoparticle catalysts show 2 – 3 times higher initial platinum mass based activity, j_{mass} , and 3 – 4 times higher initial platinum surface area specific based activity, j_{specific} , than the commercial pure platinum nanoparticle catalyst. All measured initial activities are fully in agreement with published values in the literature^{14-16, 18, 19, 93}.

Activity, stability, and degradation mechanisms of dealloyed PtCu₃ and PtCo₃ nanoparticle fuel cell catalysts

Table 9 ORR activities for Pt/HSAC, PtCu₃/HSAC and PtCo₃/HSAC catalysts before and after electrochemical stability testing. Reproduced from reference ³⁶ by permission of John Wiley and Sons.

catalyst	$j_{(\text{mass}, 0.9 \text{ V}[\text{RHE}])} [\text{A mg}_{\text{Pt}}^{-1}]$		$j_{(\text{specific}, 0.9 \text{ V}[\text{RHE}])} [\mu\text{A cm}_{\text{Pt}}^{-2}]$				
	initial ¹⁾		initial ¹⁾	10,000 cycles ²⁾	Δ [%]	2,000 cycles ²⁾	Δ [%]
Pt/HSAC	0.14 ± 0.01		191 ± 20	248 ± 32	+ 30	274 ± 30	+ 43
PtCu ₃ /HSAC	0.44 ± 0.08		743 ± 104	566 ± 5	- 24	279 ± 33	- 62
PtCo ₃ /HSAC	0.34 ± 0.15		661 ± 266	380 ± 106	- 42	285 ± 23	- 57

¹⁾mean value was determined from 6 (= 3 start-up + 3 lifetime) independent measurements

²⁾mean value was determined from 3 independent measurements

“lifetime” voltage cycling regime. Figure 44 shows the changes of the platinum surface area specific based activities before (solid symbols) and after 10,000 “lifetime” voltage cycles from 0.5 – 1.0 V vs. RHE with 50 mV s⁻¹ (hollow symbols) for PtCo₃/HSAC (blue square), PtCu₃/HSAC (red circular) and Pt/HSAC (black triangle) nanoparticle catalysts.

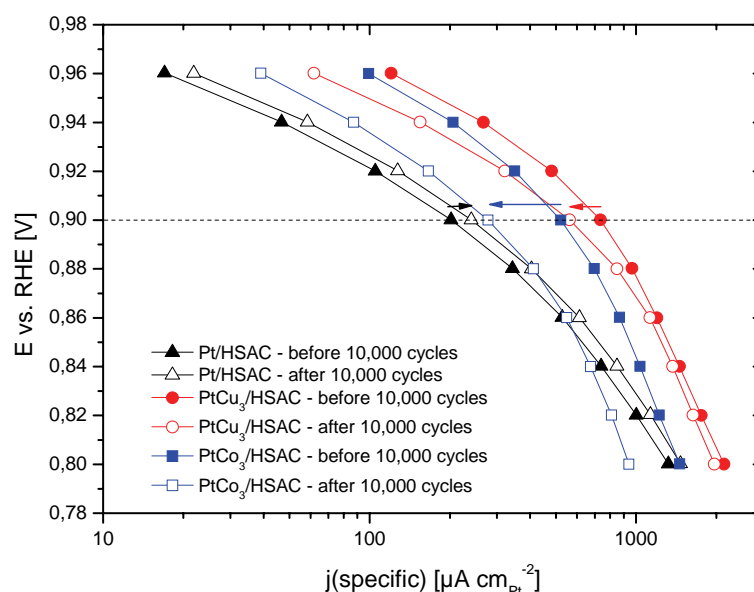


Figure 44 Platinum surface area specific activity based Tafel Plot for PtCo₃/HSAC (blue square), PtCu₃/HSAC (red circular) and Pt/HSAC (black triangle) catalysts before (solid symbols) and after (hollow symbols) 10,000 voltage cycles from 0.5 – 1.0 V vs. RHE with 50 mV s⁻¹ in 0.1 M HClO₄. Reproduced from reference ³⁶ by permission of John Wiley and Sons.

Activity, stability, and degradation mechanisms of dealloyed PtCu₃ and PtCo₃ nanoparticle fuel cell catalysts

In combination with Table 9 (see columns 3 – 5) we observed that j_{specific} for initial PtCu₃/HSAC and PtCo₃/HSAC nanoparticle catalysts decreased by 24% and 42%, whereas for Pt/HSAC j_{specific} increased by 30%. The increase of j_{specific} for Pt/HSAC after 10,000 voltage cycles can be explained by the particle size growth from 2.3 ± 0.7 nm to 3.1 ± 0.7 nm (35%, see Table 8). Meanwhile, j_{specific} decreased dramatically for both Pt alloys after 10,000 voltage cycles, as shown in Table 9 (see columns 3 – 5). But, the mean particle size of the Pt alloys is almost unchanged (PtCu₃/HSAC from 4.3 ± 1.6 nm to 4.4 ± 1.6 nm (2%) and PtCo₃/HSAC from 4.0 ± 1.0 nm to 4.6 ± 1.8 nm (15%), see Table 8). Furthermore, the electrochemical cycling up to 1.0 V vs. RHE lowered only slightly the overall chemical base metal content for both Pt alloys after the “lifetime” stability test protocol (see Table 8). Therefore, we conclude that the decrease of j_{specific} is likely caused by rearrangements of Pt atoms on the particle surface resulting in changes in defect densities (increased surface roughness), surface morphology, and Pt shell thickness. In parallel, the observed slight base metal losses from the near-surface region would lead to an increase in the platinum shell thickness of the core – shell nanoparticles. These processes reduce the lattice strain in the Pt enriched shell of the particles and hence the intrinsic specific ORR activity of the Pt alloy catalysts¹⁴.

Nevertheless, the resulting platinum surface area specific based activity, j_{specific} , of Pt alloy nanoparticle catalysts is still two times higher than that for commercial pure platinum nanoparticle catalyst after the “lifetime” test condition.

“start-up” voltage cycling regime. Figure 45 shows the changes of platinum surface area specific based activities before (solid symbols) and after 2,000 “start-up” voltage cycles from 0.5 – 1.5 V vs. RHE with 50 mV s^{-1} (hollow symbols) for PtCo₃/HSAC (blue square), PtCu₃/HSAC (red circular) and Pt/HSAC (black triangle) nanoparticle catalysts.

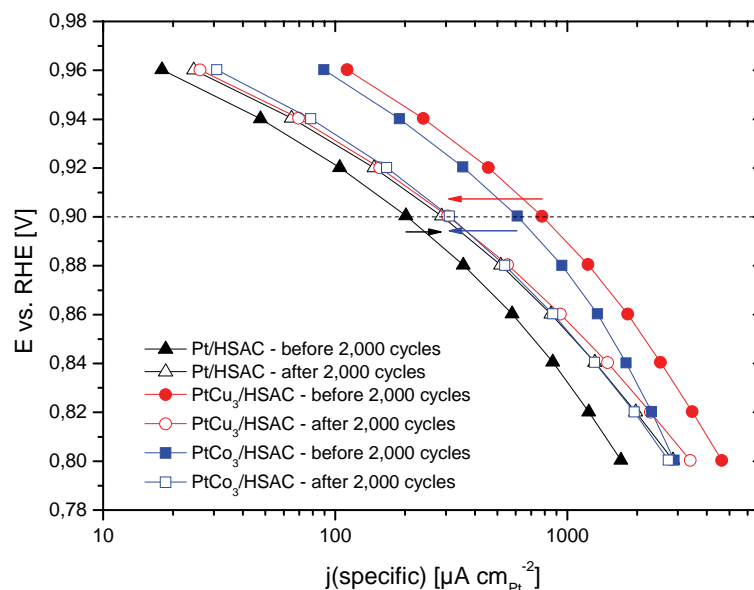


Figure 45 Platinum surface area specific activity based Tafel Plot for PtCo₃/HSAC (blue square), PtCu₃/HSAC (red circular) and Pt/HSAC (black triangle) catalysts before (solid symbols) and after (hollow symbols) 2,000 voltage cycles from 0.5 – 1.5 V vs. RHE with 50 mV s⁻¹ in 0.1 M HClO₄. Reproduced from reference ³⁶ by permission of John Wiley and Sons.

In combination with Table 9 (see columns 3, 6 – 7), j_{specific} for Pt/HSAC increased by 43%, whereas for PtCu₃/HSAC and PtCo₃/HSAC j_{specific} decreased by 62% and 57%. Under this strong corrosion and dissolution condition the mean particle size grow very fast for Pt/HSAC from 2.3 ± 0.7 nm to 5.6 ± 1.5 nm (144%), for PtCu₃/HSAC from 4.3 ± 1.6 nm to 6.8 ± 2.2 nm (58%) and for PtCo₃/HSAC from 4.0 ± 1.0 nm to 7.0 ± 2.8 nm (75%) (see Table 8). Meanwhile, the platinum surface area specific based activity, j_{specific} , only increased for the Pt/HSAC. For the Pt alloys j_{specific} decreased dramatically. Table 8 reveals a significant change in the chemical composition from initial Pt_{63±2}Cu_{37±2} to final Pt_{91±3}Cu_{9±3} and from initial Pt_{80±2}Co_{20±2} to final Pt_{94±2}Co_{6±2} after 2,000 “start-up” voltage cycles up to 1.5 V vs. RHE; this change is due to the strong corrosion conditions. The strong dissolution of copper or cobalt from the Pt alloy core – shell nanoparticles induced a drop in the geometric strain of the platinum shell which initially led to the improved performance for ORR. The decrease of j_{specific} related clearly to the change of the morphology and chemical composition of the

Pt alloys. The final values of j_{specific} for the alloy catalysts are similar to pure platinum particles by the same particle size.

In summary, PtCu₃ and PtCo₃ alloy nanoparticle catalysts exhibit a higher initial platinum mass and platinum surface area specific based ORR activities compared to the commercial pure platinum nanoparticle catalyst. After 10,000 “lifetime” voltage cycles up to 1.0 V vs. RHE the Pt alloys exhibit still an up to two times increased j_{specific} compared with the commercial pure platinum. The Pt alloys remain its chemical composition after 10,000 “lifetime” voltage cycles. Furthermore, after 2,000 “start-up” voltage cycles up to 1.5 V vs. RHE the values of j_{specific} for Pt alloys approximate rapidly to pure platinum at around 7 nm due to the change in the morphology and the composition to almost completely dealloyed particles. The activity loss is related with the morphological surface change as well the decrease of the compressive lattice strain of Pt alloy particles.

4.1.3 Particle growth and platinum ECSA loss mechanisms

Evolution in particle size distribution. Figure 46 to Figure 48 show the particle size distributions with the according TEM images for Pt/HSAC, PtCu₃/HSAC and PtCo₃/HSAC nanoparticle catalysts (a) after synthesis, (b) after 2,000 “start-up” voltage cycles from 0.5 – 1.5 V vs. RHE with 50 mV s⁻¹ and (c) after 10,000 “lifetime” voltage cycles from 0.5 – 1.0 V vs. RHE with 50 mV s⁻¹. From the analysis of the TEM images, all catalysts achieved a similar critical particle size (D_{critical}) after the voltage cycling (see Table 8, columns 2 – 6). The experimentally determined $D_{\text{critical}}^{\text{“lifetime”}}$ is 3 – 4 nm under “lifetime” conditions, whereas for the “start-up” conditions $D_{\text{critical}}^{\text{“start-up”}}$ is 5 – 7 nm. These values are in a good agreement with our previously experimental observation for Pt/Vulcan XC 72R and Pt/MWCNT nanoparticle catalysts⁵² and also in line with recent computational predictions of asymptotic particle diameters under the chosen “lifetime” conditions⁴⁹.

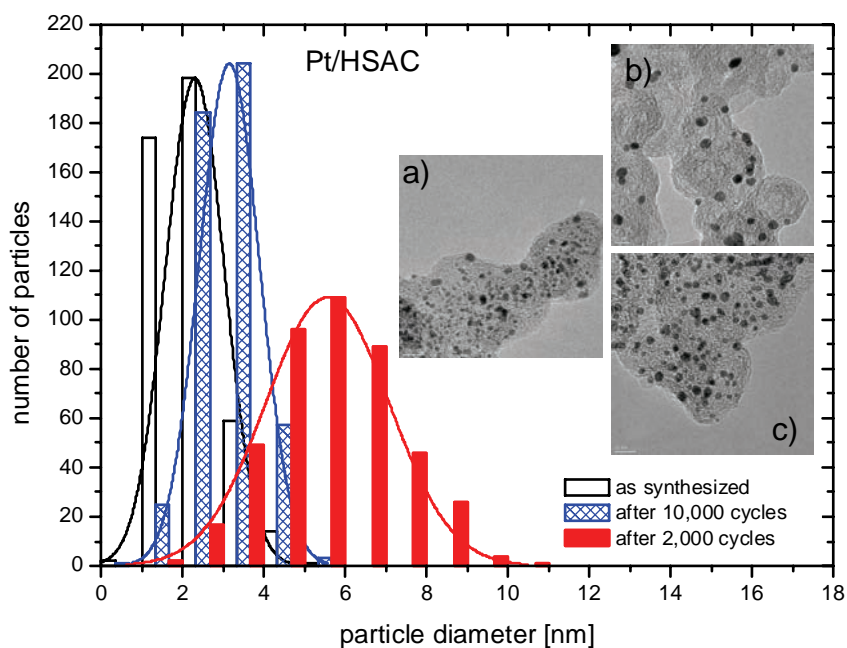


Figure 46 Evolution of the particle size distributions and the according TEM images (scale bar of 10 nm) for Pt/HSAC nanoparticle catalyst (a) as synthesized, (b) after 2,000 voltage cycles from 0.5 – 1.5 V vs. RHE and (c) after 10,000 voltage cycles from 0.5 – 1.0 V vs. RHE with 50 mV s^{-1} in 0.1 M HClO₄. The bar charts are shown with x-offset. Reproduced from reference³⁶ by permission of John Wiley and Sons.

Based on our data provided here, we suggest that these critical particle sizes (D_{critical}) are of general validity for the Pt alloy nanoparticles under typical and corrosive fuel cell conditions.

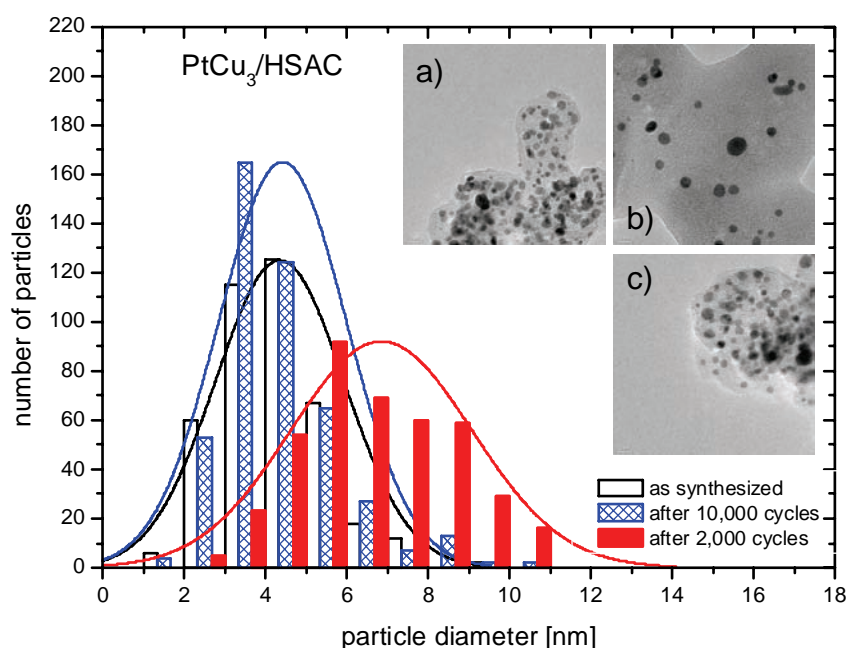


Figure 47 Evolution of the particle size distributions and the according TEM images (scale bar of 10 nm) for PtCu₃/HSAC nanoparticle catalyst (a) as synthesized, (b) after 2,000 voltage cycles from 0.5 – 1.5 V vs. RHE and (c) after 10,000 voltage cycles from 0.5 – 1.0 V vs. RHE with 50 mV s⁻¹ in 0.1 M HClO₄. The bar charts are shown with x-offset. Reproduced from reference³⁶ by permission of John Wiley and Sons.

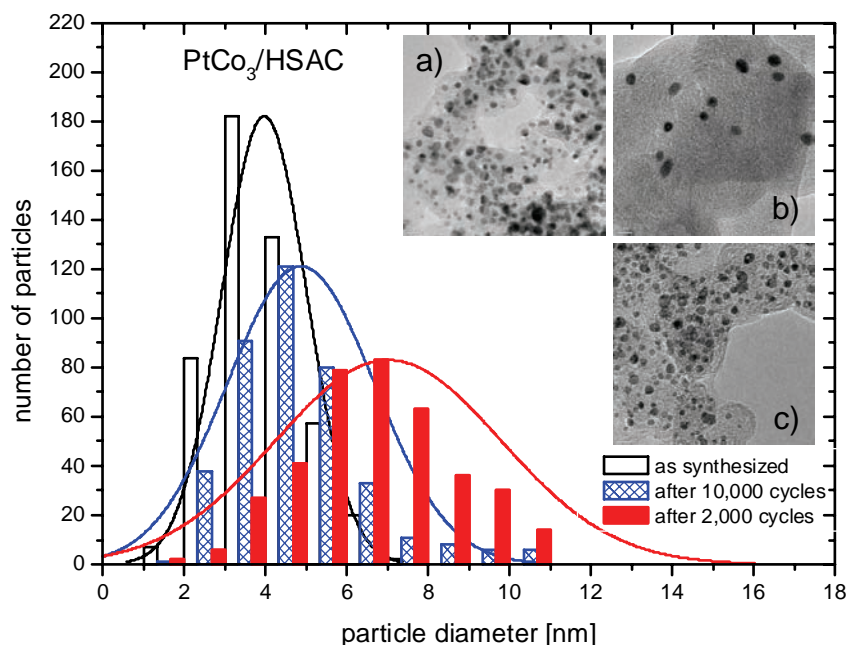


Figure 48 Evolution of the particle size distributions and the according TEM images (scale bar of 10 nm) for PtCo₃/HSAC nanoparticle catalyst (a) as synthesized, (b) after 2,000 voltage cycles from 0.5 – 1.5 V vs. RHE and (c) after 10,000 voltage cycles from 0.5 – 1.0 V vs. RHE with 50 mV s⁻¹ in 0.1 M HClO₄. The bar charts are shown with x-offset. Reproduced from reference³⁶ by permission of John Wiley and Sons.

Activity, stability, and degradation mechanisms of dealloyed PtCu₃ and PtCo₃ nanoparticle fuel cell catalysts

It is evident from our TEM studies, that the nanoparticle bulk density (particles per volume) dropped significantly during the “start-up” voltage cycling (see Figure 46 to Figure 48, b) compared to that in Figure 46 to Figure 48, a. The particle growth of Pt/HSAC, PtCu₃/HSAC and PtCo₃/HSAC catalysts by 144%, 58% and 75% (see Table 8, column 6) does not accurately sufficiently the decrease of the particle bulk density. We assume that carbon corrosion, particle detachment and dissolution / Pt loss into electrolyte contribute for the reduction of the particle bulk density^{48, 49, 107-109}.

During the “lifetime” voltage cycling the particle size grew by 35%, 2% and 15% (see Table 8, column 4) for Pt/HSAC, PtCu₃/HSAC and PtCo₃/HSAC catalysts, respectively. The TEM images after “lifetime” testing (see Figure 46 to Figure 48, c) exhibit a nearly unchanged nanoparticle bulk density behavior compared with the as synthesized (see Figure 46 to Figure 48, a). Here, we assume that the Pt alloys and pure platinum particles were achieved a stable $D_{critical}$, while the influence of the carbon corrosion, particle detachment and dissolution / Pt loss into electrolyte is negligible for this voltage regime. The critical particle size is dependent on the upper turning potential of the applied voltage cycles.

Initial ECSA of dealloyed PtCu₃, PtCo₃ and Pt. Table 10 summarizes the absolute and normalized platinum electrochemical active surface area (ECSA) for all catalysts before and after the electrochemical stability testing for both protocols.

Table 10 Platinum electrochemical active surface area (ECSA) for Pt/HSAC, PtCu₃/HSAC and PtCo₃/HSAC catalysts before and after electrochemical stability testing. Reproduced from reference³⁶ by permission of John Wiley and Sons.

catalyst	ECSA [m ² g _{Pt} ⁻¹] initial ¹⁾	N-ECSA ³⁾ [%]				
		initial	10,000 cycles ²⁾	? [%]	2,000 cycles ²⁾	? [%]
Pt/HSAC	74 ± 7	100	73 ± 3	- 27	31 ± 2	- 69
PtCu ₃ /HSAC	59 ± 6	100	94 ± 7	- 6	48 ± 3	- 52
PtCo ₃ /HSAC	50 ± 6	100	107 ± 4	+ 7	62 ± 3	- 38

¹⁾mean value was determined from 6 (= 3 start-up + 3 lifetime) independent measurements

²⁾mean value was determined from 3 independent measurements

³⁾N-ECSA (cycle#) = ECSA (cycle#) / ECSA (initial) * 100 %

The initial Pt alloys exhibit a lower ECSA compared with the commercial pure platinum. The reduced ECSA is caused by the difference in the as synthesized mean particle size of the Pt alloys (see Table 8, column 2). Generally, small particles show higher values for ECSA than large particles^{40, 49, 53}. In Table 10 the PtCu₃/HSAC and PtCo₃/HSAC exhibit almost same values of the ECSA, due to the similar mean particle sizes (see Table 8, column 2). The results for the ECSA of the Pt alloys and pure platinum are in a good agreement with published values in the literature^{35, 93, 110}.

Evolution of the normalized platinum electrochemical active surface area (N-ECSA). We now turn to the platinum electrochemical active surface area (ECSA) trends and combined with mean particle size changes to clarify the main loss mechanisms of Pt alloys and pure platinum. Figure 49 shows the experimentally determined normalized ECSA (N-ECSA) for Pt/HSAC (black triangle), PtCu₃/HSAC (red circular) and PtCo₃/HSAC (blue square) nanoparticle catalysts under “lifetime” (solid symbols) and “start-up” (hollow symbols) conditions. The N-ECSA was calculated as follows:
$$\text{N-ECSA (cycle\#)} = \text{ECSA (cycle\#)} / \text{ECSA (initial)} * 100\%.$$

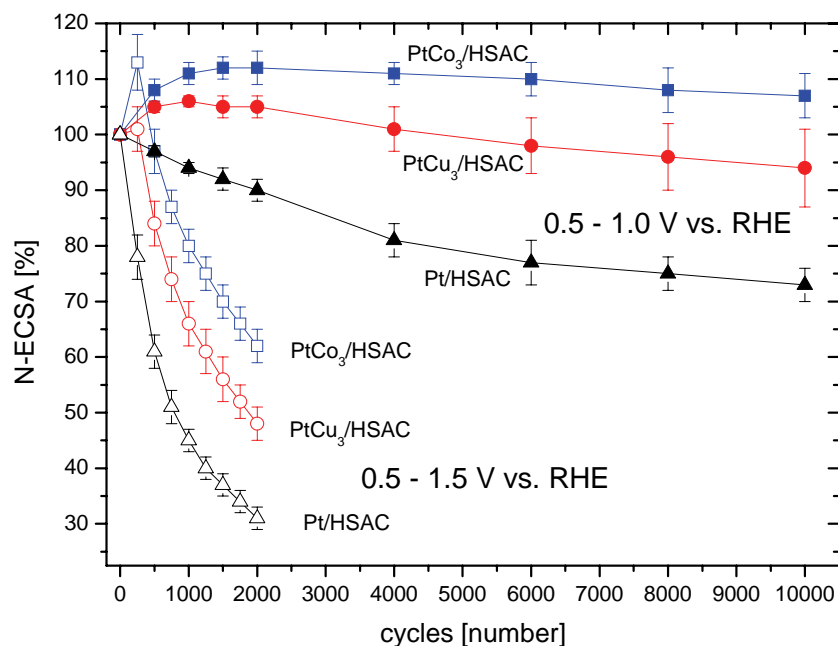


Figure 49 Evolution of the normalized platinum electrochemical active surface area (N-ECSA) loss for PtCo₃/HSAC (blue square), PtCu₃/HSAC (red circular) and Pt/HSAC (black triangle) catalysts due to the voltage cycling from 0.5 – 1.0 V vs. RHE (solid symbols) and from 0.5 – 1.5 V vs. RHE (hollow symbols) with 50 mV s⁻¹ in 0.1 M HClO₄. $N-ECSA(\text{cycle}\#) = ECSA(\text{cycle}\#) / ECSA(\text{initial}) * 100\%$. Reproduced from reference³⁶ by permission of John Wiley and Sons.

N-ECSA trends in the “lifetime” stability regime. We now discuss the curves of the N-ECSA for all catalysts in the “lifetime” regime. The N-ECSA dropped off by 27% and 6% for platinum and PtCu₃, respectively, while for PtCo₃ it increased by 7% (see Table 10, column 5). Generally, the increase of the particle size leads to a decrease of the ECSA. This is why the decrease of N-ECSA of platinum is at least partially accounted for its particle size growth (see Figure 46). Careful inspection of Figure 49, however, reveals that for platinum there is steady initial ECSA drop correlated with the increase of the mean particle size, which slows down after around 4,000 voltage cycles. We suppose that this is the point when a quasi stable stationary “critical” particle size, D_{critical} , had been reached. Beyond that point, the N-ECSA loss for platinum is no longer controlled by particle coarsening, but rather by carbon corrosion, particle detachment and dissolution / Pt loss into the electrolyte.

For PtCu₃ and PtCo₃ nanoparticle catalysts, the overall nominal change in the values of N-ECSA is nearly negligible. This observation is in agreement with TEM results from Figure 47 to Figure 48, showing comparable mean particle size before and after voltage cycling. But, the evolution of the N-ECSA curves of the Pt alloys exhibit important differences to that of pure platinum. Both Pt alloys show an increase in N-ECSA during the first thousand cycles (up to 4,000 voltage cycles) and afterwards a steady drop. During the first thousand voltage cycles, we observed a slight N-ECSA increase which could be related to (i) a slight initial dissolution of copper and cobalt atoms (see columns 8 – 9 in Table 8) from the particle surface associated with an increase in surface roughness of the particles and (ii) particle surface carbon poison removal due to the synthesis. These processes would be in line with the mechanisms for the lower j_{specific} activity discussed above. Based on these experimental observations, we conclude that a quasi stable, critical particle size (D_{critical}) must have already existed at the beginning of the “lifetime” test or else has been quickly attained during the initial phase of the voltage cycling test. It is worth noting that, again, beyond around 4,000 voltage cycles in Figure 49, the rate for ECSA loss of the Pt alloys approaches that of pure Pt. This may suggest a physically similar ECSA loss mechanism, for instance, based on support corrosion. According to this scenario, Ostwald-type ECSA loss mechanism would now no longer be dominant, while the N-ECSA loss is now largely controlled by carbon corrosion, particle detachment and dissolution / Pt loss into the electrolyte.

We summarize our results in the “lifetime” regime by highlighting that Pt and Pt alloy nanoparticle catalysts appear to arrive at a voltage dependent critical quasi-stable diameter, D_{critical} , of 3 – 4 nm after around 4,000 voltage cycles. Beyond that, ECSA losses are largely induced by carbon corrosion, particle detachment and dissolution / Pt loss into the electrolyte.

N-ECSA trends in the “start-up” stability regime. During cycling in the “start-up” regime, the carbon corrosion and metal dissolution are the dominant mechanisms^{49, 55}. In fact, a much more drastic decrease of the N-ECSA was observed for all catalysts compared to that in the “lifetime” regime. The N-ECSA reduced by 69%, 52% and 38% for Pt, PtCu₃ and PtCo₃, respectively (see Table 10, column 7), well correlating with the changes in mean particle size (see Table 8, column 5). But again, looking at the actual run of the N-ECSA loss in Figure 49, significant differences between Pt and Pt alloys are obvious. For Pt at the beginning it is a steady drop and after around 1,000 voltage cycles the loss curve becomes slowed down. The two ranges, at first steady drop and following slowed down, are very similar to the N-ECSA run for the “lifetime” stability test. However, D_{critical} is reached earlier and is larger due to the higher upper turning potential of 1.5 V vs. RHE. When D_{critical} has been achieved in the first 1,000 voltage cycles, the N-ECSA loss is no longer controlled by particle growth, but rather by the carbon corrosion, particle detachment and dissolution / Pt loss into the electrolyte. Here, the slope of the N-ECSA loss curve is steeper than that in the “lifetime” regime.

This characteristic N-ECSA loss behavior of Pt is principally observed for PtCu₃ and PtCo₃. More rapid dissolution of Cu or Co and the removal of carbon poison on the particle surface during cycling up to 1.5 V vs. RHE resulting in a rapid increase of surface roughness, explains the initial fast N-ECSA increase during the first 250 voltage cycles. Rapid base metal loss is evidence by Cu/Co content of less than 10 at. % for the Pt alloys (see Table 8). After quick Cu/Co leaching the runs of the N-ECSA loss curves of the Pt alloys are similar to that of pure Pt. This suggests that the nearly completely dealloyed Pt alloys now approach the Pt characteristics for ECSA and final ORR activities as seen in Table 9, column 6.

In summary, for the Pt alloys the early stage of the voltage cycling test in the “start-up” regime is dominated by two competing processes, namely, rapid metal dealloying/ dissolution and particle growth, which give rise to the complex N-ECSA curves. Particle growth leads to a decrease of N-ECSA, in contrast, strong dealloying causes an increase of N-ECSA by the enhanced surface

Activity, stability, and degradation mechanisms of dealloyed PtCu₃ and PtCo₃ nanoparticle fuel cell catalysts

roughness. The Pt alloy particles eventually reach a quasi-stable mean particle diameter, D_{critical} , and a stable Pt rich chemical composition. At this point, the rate of N-ECSA loss slows down and approaches the behavior of pure Pt. The later stages of the degradation process in the “start-up regime” are dominated by carbon corrosion associated with particle detachment, possibly combined with the dissolution of Pt into the electrolyte.

Evolution of the degradation and ESCA loss mechanisms for Pt and Pt alloys particles. In Figure 50, we illustrate the dominant degradation mechanisms of Pt and Pt alloy nanoparticle electrocatalysts over the life cycle of our experimental stability tests.

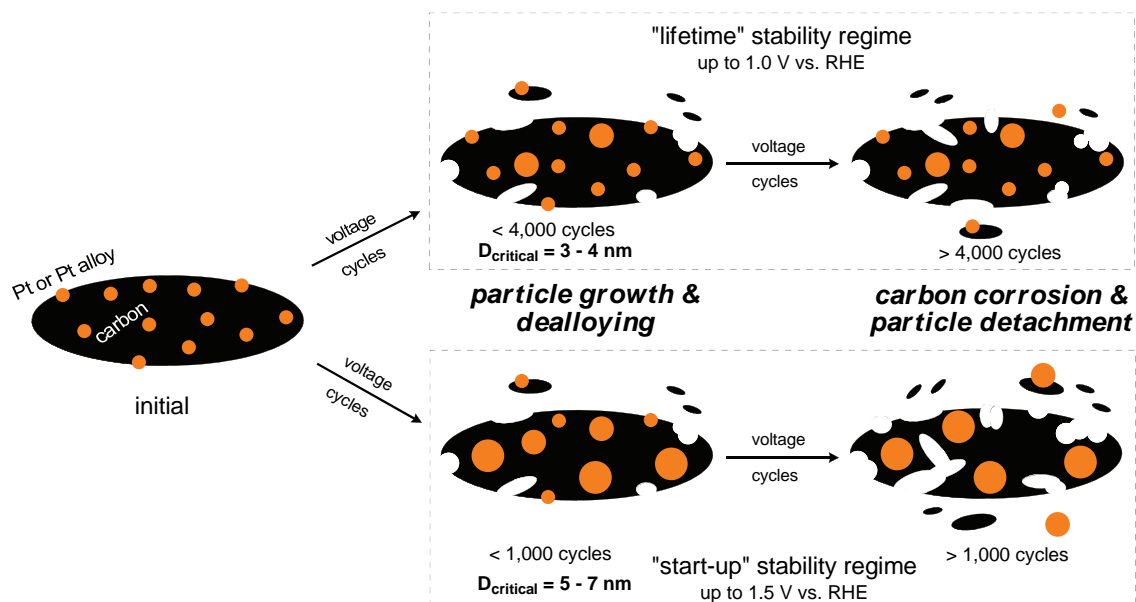


Figure 50 Illustration of dominant ECSA loss mechanisms along the life cycle of carbon supported Pt, Pt-Cu and Pt-Co alloy catalysts. Particle growth up to a quasi-stable critical diameter, D_{critical} , is followed by a degradation regime dominated by support corrosion associated with particle detachment. Continued metal dissolution is likely at the extremely corrosive upper electrode voltages of the “start-up” regime. Reproduced from reference ³⁶ by permission of John Wiley and Sons.

Our life cycle degradation model initially assumes well-dispersed pure Pt and Pt alloy nanoparticles on a carbon support, left portion of the Figure 50. ECSA loss mechanisms during voltage cycling in the “lifetime” and “start-up” regimes are indicated in the upper and lower box, respectively. From our experimental results we propose a transient particle growth degradation mechanism for both regimes. We cannot distinguish whether this particle growth

Activity, stability, and degradation mechanisms of dealloyed PtCu₃ and PtCo₃ nanoparticle fuel cell catalysts

occurs primarily through an Ostwald ripening or a particle coalescence mechanisms or a combination of both. Particle growth slows down significantly at a critical mean particle size, D_{critical} , which depends on the upper turning potential of the applied voltage cycles. For the Pt alloys and especially under corrosive “start-up” condition, transient strong non noble metal dissolution may be offsetting the rate of particle growth. The dealloying process and particle growth run to the same time and cannot be excluded. Once a critical particle size has been reached, ECSA degradation enters a longer-term regime controlled by support stability. Pt dissolution, especially for the “lifetime” condition, becomes secondary compared to the structural degradations of the carbon support. Upon carbon loss, active catalyst particles detach into the electrolyte and are lost for the catalytic process.

4.1.4 Conclusions

In this chapter, we have examined the activity, stability, and degradation mechanisms of dealloyed PtCu₃/HSAC and PtCo₃/HSAC nanoparticle catalysts under two distinct voltage cycling protocols, a “lifetime” (10,000 voltage cycles from 0.5 – 1.0 V vs. RHE with 50 mV s⁻¹) and a “start-up” (2,000 voltage cycles from 0.5 – 1.5 V vs. RHE with 50 mV s⁻¹) regime, which are highly relevant to fuel cell operation. From our experimental data and correlation of the platinum electrochemical active surface area, particle size distribution, particle bulk density, chemical composition and oxygen reduction activity, we conclude, that

- the PtCo₃ and PtCu₃ nanoparticle catalysts exhibit clearly enhanced cycling durability compared to pure Pt nanoparticle catalyst in both voltage cycling regimes.
- the dealloyed Pt alloy nanoparticle catalysts show a 2 – 3 times higher initial platinum mass based activity, j_{mass} , and a 3 – 4 times higher initial platinum surface area specific based activity, j_{specific} , compared with a commercial pure platinum nanoparticle catalyst.
- the dealloyed Pt alloy nanoparticle catalysts show still two times higher j_{specific} at the end of the typical “lifetime” operating condition than pure Pt.
- all catalysts reach a voltage dependent critical mean particle size, D_{critical} , at which the particle size growth rate drops to low values. This particle coarsening is the dominant ECSA loss mechanism at early stages of the catalyst life cycle, in particular for pure Pt. Once D_{critical} is reached, ECSA loss is mainly controlled by the carbon corrosion associated with particle detachment. In the case of corrosive voltage cycling in the “start-up” regime, strong oxidation of carbon and dissolution of Pt become dominant mechanisms for a rapid ECSA loss and accelerated net loss of Pt into the electrolyte.

- the ECSA loss for Pt alloys during the initial stage is a complex behavior between particle growth and base metal dissolution associated with rearrangement of Pt surface atoms. It is manifest by an initial increase in ECSA followed by a drop in ECSA at a very similar rate as pure Pt. The concurrent drop in specific activity is likely related to an increase of the Pt shell thickness by redeposition and base metal loss.
- the critical particle size (D_{critical}) for electrocatalysts under the present conditions was reached at around 4,000 voltage cycles in the “lifetime” regime, whereas already at around 1,000 voltage cycles for the “start-up” regime.
- the critical particle size is strongly dependent on the maximum voltage range. In the “lifetime” regime $D_{\text{critical}}^{\text{“lifetime”}}$ at 3 – 4 nm is smaller than that in the “start-up” regime ($D_{\text{critical}}^{\text{“start-up”}}$ at 5 – 7 nm).
- the chemical compositional stability of the dealloyed PtCu₃ and PtCo₃ nanoparticle catalysts is voltage dependent. Under “lifetime” testing the composition changes only slightly. In contrast, under “start-up” testing the Pt alloys exhibit significant compositional base metal losses. The final copper / cobalt concentration is lower than 10 at. %.

Together, we provide an evolutionary lifecycle model of the dealloyed PtCu₃, PtCo₃ nanoparticle fuel cell catalysts addressing the temporal sequence of dominant degradation processes.

4.2 Activity, structure and degradation of dealloyed PtNi₃ nanoparticle fuel cell electrocatalyst

This chapter is based on the publication

Hasché, F.; Oezaslan, M.; Strasser, P.,

Activity, Structure and Degradation of Dealloyed PtNi₃ Nanoparticle
Electrocatalyst for the Oxygen Reduction Reaction in PEMFC.

Journal of The Electrochemical Society **2012**, 159, (1), B25-B34.

<http://dx.doi.org/10.1149/2.030201jes>

Hasché, F.; Oezaslan, M.; Strasser, P.,

Activity and Structure of Dealloyed PtNi₃ Nanoparticle
Electrocatalyst for the Oxygen Reduction Reaction in PEMFC.

ECS Transactions **2011**, 41, (1), 1079-1088.

<http://dx.doi.org/10.1149/1.3635640>

Reproduced by permission of ECS – The Electrochemical Society.

Here, a synthesis, activity and stability study of a dealloyed, highly active PtNi₃ alloy nanoparticle catalyst for the oxygen reduction reaction (ORR) in acidic media is presented. After activation by electrochemical dealloying of a PtNi₃ precursor, the Pt-Ni nanoparticle catalyst (referred to as “dealloyed PtNi₃”) exhibits a 7 – 8 times higher Pt mass based activity and a 6 – 7 times higher Pt surface area specific based activity for ORR than pure Pt at comparable mean particle size. In addition, the long-term stability of the dealloyed PtNi₃ was tested for typical fuel cell operating as well as more corrosive fuel cell start-up conditions. After 10000 voltage cycles between 0.5 – 1.0 V vs. RHE at 50 mV s⁻¹ the dealloyed PtNi₃ catalyst still shows 4 – 5 fold increase in Pt surface area specific based activity compared with that for pure Pt. The enhanced activity performance of the dealloyed PtNi₃ nanoparticles is a promising electrocatalyst to attain the required demands for the PEMFC application.

4.2.1 Structural and compositional characterization of as synthesized PtNi₃ alloy catalyst

Figure 51 shows the XRD profiles of the synthesized PtNi₃/Vulcan XC 72R (more details in chapter 2.4 *Synthesis of PtNi₃/Vulcan XC 72R*) and commercial pure Pt/Vulcan XC 72R nanoparticle catalyst which was used for the preparation of the Pt-Ni alloy. The vertical lines in the XRD profile denote the reference powder diffraction patterns of (111), (200), and (220) reflections for pure face centered cubic (fcc) Pt (black, dashed lines) and Ni (blue, dotted points)⁸⁷. The XRD profile for Pt-Ni alloy shows three cubic crystal phases obtained from the Rietveld refinement. The (111), (200), and (220) reflections of the alloy are clearly shifted to higher 2θ angles with respect to pure fcc Pt, indicating the insertion of Ni atoms in the fcc Pt lattice and the resulting lattice contraction.

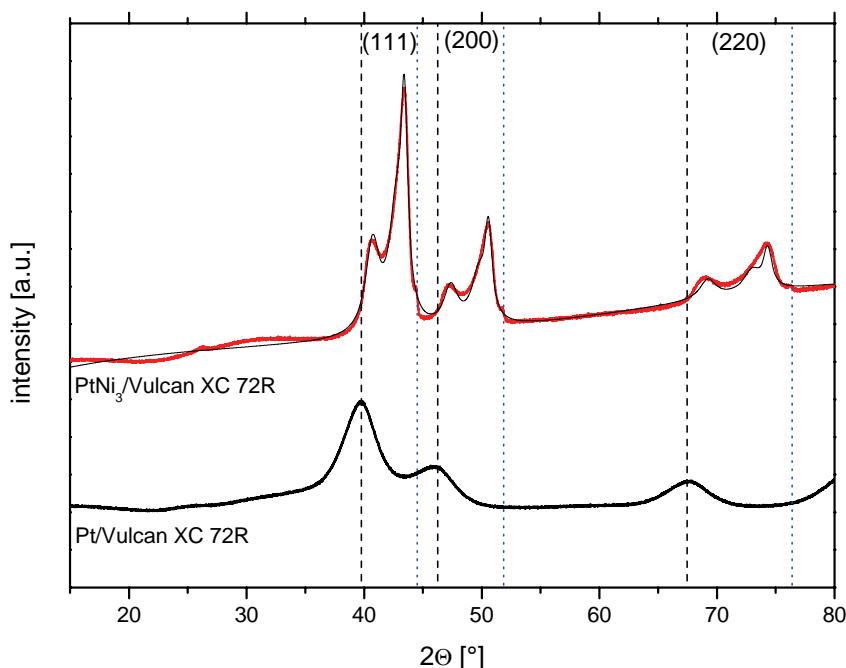


Figure 51 XRD profiles of the as synthesized PtNi₃/Vulcan XC 72R catalyst and pure Pt/Vulcan XC 72R catalyst, shown with y-offset. The thin black line indicates the Rietveld refinement fit of PtNi₃/Vulcan XC 72R ($R_{wp} = 3.50$, $R_{exp} = 0.55$, $GOF = 6.33$). Vertical lines denote reference powder diffraction patterns of pure fcc Pt (black, dashed lines) and Ni (blue, dotted points). PDF(Pt)#00-004-0802, PDF(Ni)#00-004-0850⁸⁷. Reproduced from reference¹⁰⁴ by permission of ECS – The Electrochemical Society.

No reflections of pure Pt were found, in contrast to pure fcc Ni phase with very small reflexes at $2\Theta = 44.4^\circ$, 51.7° and 76.2° . A quantification by Rietveld refinement only showed a pure fcc Ni phase below 1 wt. %. Nevertheless, the quantitative Rietveld analysis revealed that the disordered fcc Pt-Ni alloy phase is the major component: 45.9 ± 4.2 wt.%, with a crystallite size of 4.2 ± 0.4 nm. The stoichiometric composition of the major fcc Pt-Ni component was determined from the lattice parameter as Pt₃₆Ni₆₄ using Vegard's law. The minor fractions are the fcc Pt rich alloy crystal phase as Pt₇₉Ni₂₁ (25.8 ± 2.4 wt.%, 4.3 ± 0.3 nm) and the fcc Ni rich alloy crystal phase as Pt₂₂Ni₇₈ (28.4 ± 3.3 wt.%, 9.2 ± 0.9 nm).

Furthermore, the chemical composition of the as synthesized Pt-Ni alloy catalyst was analyzed using EDS. The EDS result exhibits an average composition of Pt_{31±1}Ni_{69±1}, which is similar to the desired atomic ratio. The evaluation of TEM images yielded a mean particle size of 6.4 ± 1.9 nm for the Pt-Ni alloy precursor by counting for more than 400 particles.

4.2.2 Electrochemical characterization of dealloyed PtNi₃ nanoparticle catalyst

For the catalytic activation the Pt-Ni alloy nanoparticle precursor was electrochemically dealloyed by removing of Ni atoms from the particle surface¹³⁻¹⁶. The first and second CV profile of the PtNi₃ alloy precursor is shown in Figure 52a. During the voltage cycling the CV profile approached more and more the characteristic CV features of a pure Pt surface, associating with the broad underpotential hydrogen deposition and stripping peaks (0.06 – 0.40 V vs. RHE), the double layer capacitive current plateau (0.4 – 0.6 V vs. RHE) and the Pt hydroxide and oxide peaks (0.7 – 1.0 V vs. RHE). As guide to the eye, the inserted arrows in Figure 52a indicate the decrease of the very broad anodic shoulder between 0.3 – 0.6 V vs. RHE and at the same time the increase of the hydrogen ad/desorption regime during the voltage cycling.

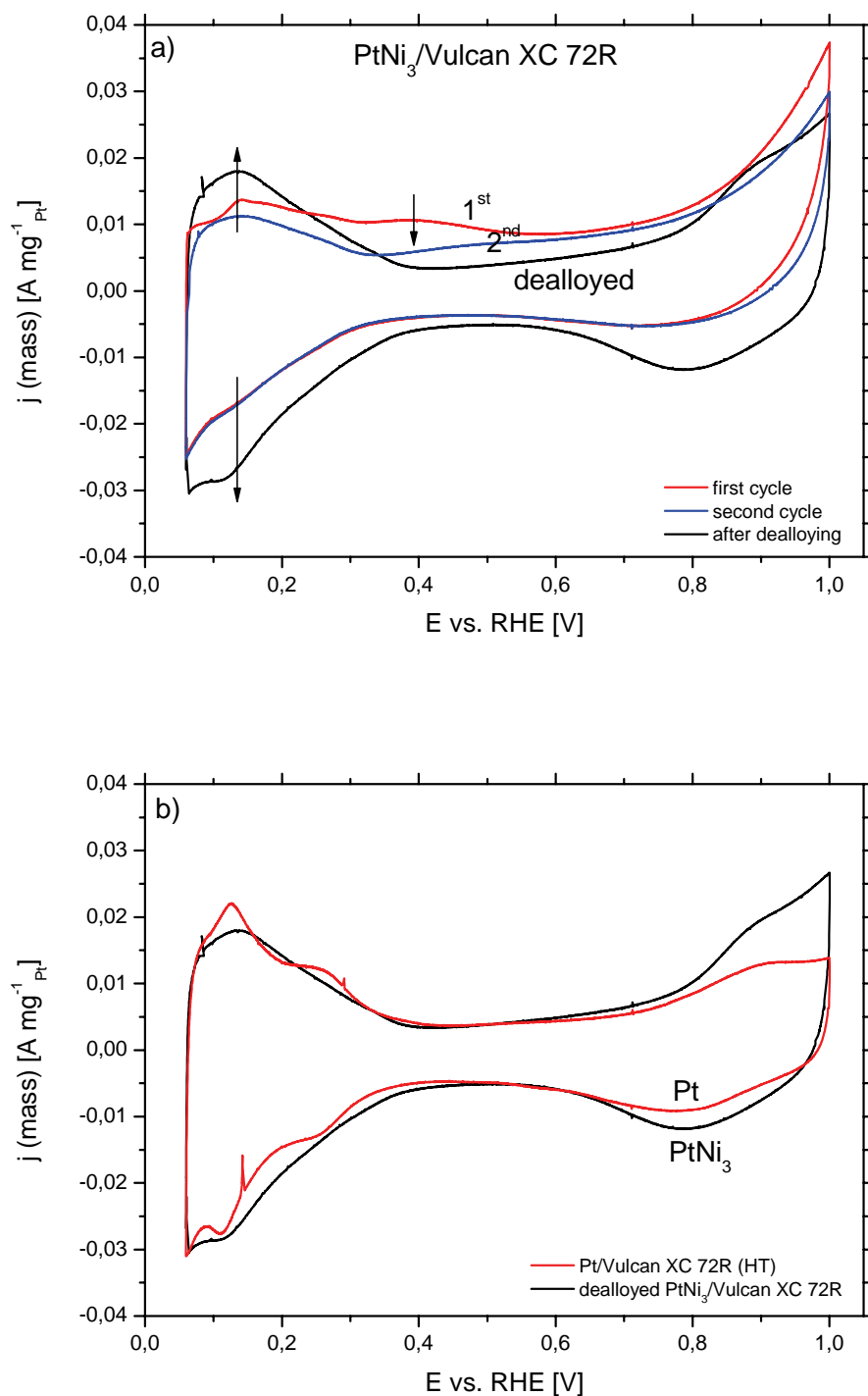


Figure 52 Cyclic voltammogram profiles of (a) PtNi₃/Vulcan XC 72R for the first scan (red), second scan (blue) and after dealloying (black); (b) comparison of dealloyed PtNi₃/Vulcan XC 72R (black) with Pt/Vulcan XC 72R (HT) (red). CV: 0.06 – 1.00 V vs. RHE, 100 mV s⁻¹ in deaerated 0.1 M HClO₄ at room temperature. Reproduced from reference ¹⁰⁴ by permission of ECS – The Electrochemical Society.

The very broad anodic shoulder on the first CV scan indicate the presence of underpotentially deposited Ni, whereas the hydrogen ad/desorption regime exhibits the presence of Pt on the particle surface. The dissolution of Ni is an irreversible process under the chose potential condition; any signs of Ni redeposition during the cathodic scan are absent. The activation by dealloying was completed when the CV profile reached a time-stable state and shape. Figure 52b compares the CV profiles of the dealloyed PtNi₃ and heat treated pure Pt (see below) and reveals the Pt enrichment on the particle surface of dealloyed Pt-Ni alloy particles. This electrochemical activation process with resulting in time-stable Pt-resembling cyclic voltammograms was also observed for Pt poor Pt-Cu and Pt-Co alloy system¹³⁻¹⁶.

The platinum electrochemical active surface area (ECSA) of the dealloyed PtNi₃/Vulcan XC 72R catalyst obtained from the final CV profile after dealloying is $19 \pm 3 \text{ m}^2 \text{ g}^{-1}$. To compare the dealloyed PtNi₃ nanoparticle catalyst with a pure Pt catalyst by similar mean particle size, a commercial, pure 46.7 wt. % Pt/Vulcan XC 72R catalyst was subjected to thermal annealing (henceforth denoted as Pt/Vulcan XC 72R (HT) or Pt (HT)) with the same annealing protocol which was earlier used for the Pt-Ni alloy formation. This value is in a good agreement with the ECSA of $17 \pm 2 \text{ m}^2 \text{ g}^{-1}$ for the Pt/Vulcan XC 72R (HT) catalyst by similar mean particle size.

The observed Ni loss for PtNi₃ alloy electrocatalyst after the voltage cycling is consistent with the EDS results. The chemical composition changed clearly from as synthesized Pt_{31±1}Ni_{69±1} to Pt_{56±2}Ni_{45±2}.

The TEM images of the PtNi₃ catalyst show well dispersed alloy nanoparticles supported on the carbon (Vulcan XC 72R) as synthesized (Figure 53a) and after electrochemical dealloying (Figure 53b).

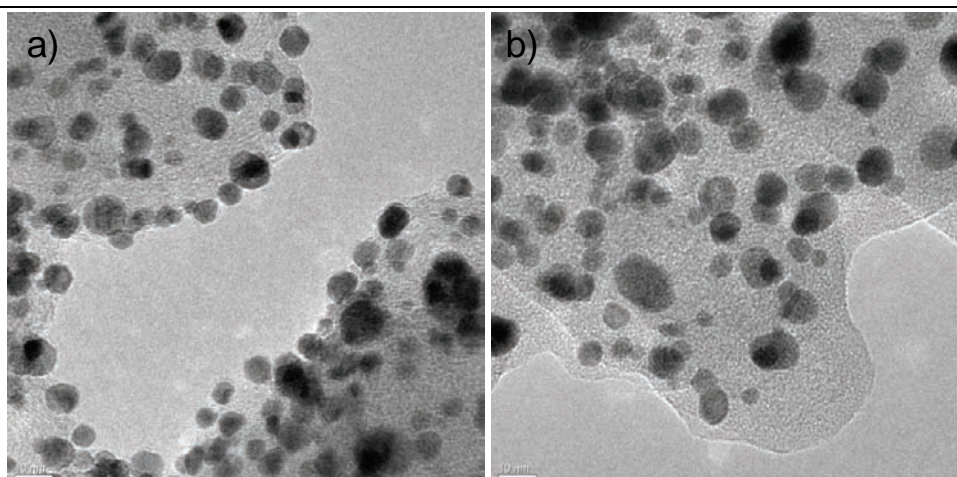


Figure 53 TEM images (scale bar of 10 nm) of PtNi₃/Vulcan XC 72R, (a) as synthesized and (b) after electrochemical dealloying procedure. Reproduced from reference ¹⁰⁴ by permission of ECS – The Electrochemical Society.

Figure 54 illustrates the resulting particle size distributions of the PtNi₃ catalyst before and after dealloying. The mean particle size here shifted from 6.4 ± 1.9 nm to 7.4 ± 2.4 nm. A careful observation of the particle size histograms indicates very slight decrease of the fraction of alloy particles below 3 nm.

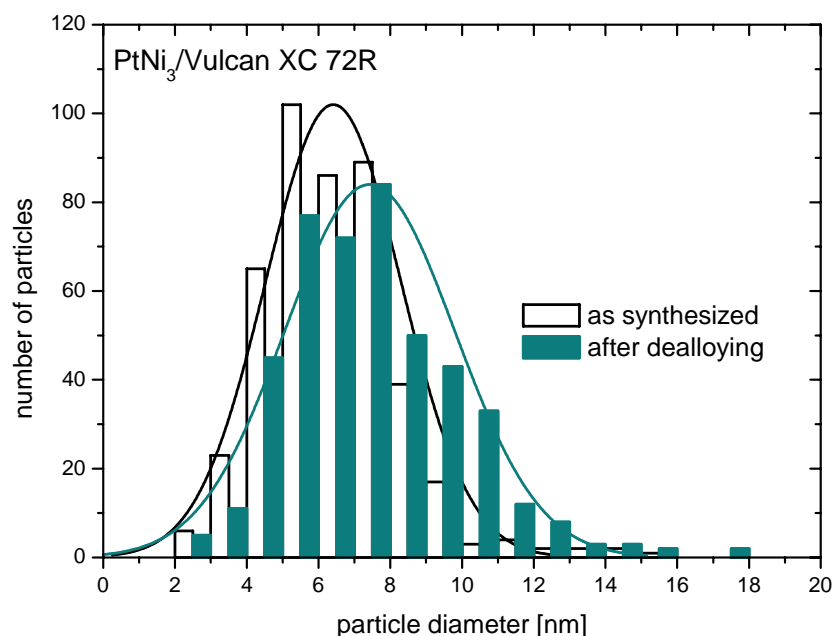


Figure 54 Evolution of the particle size distributions for PtNi₃/Vulcan XC 72R, as synthesized and after dealloying. The bar charts are shown with x-offset. Reproduced from reference ¹⁰⁴ by permission of ECS – The Electrochemical Society.

We suggest that it likely relates to the dissolution of small particles and the deposition on large particles, generally referred to as Ostwald ripening^{47, 48}.

4.2.3 ORR activities of dealloyed PtNi₃ nanoparticle catalyst

Figure 55 shows the polarization curves of the dealloyed PtNi₃/Vulcan XC 72R nanoparticle catalyst at various rotating speeds in oxygenated 0.1 M HClO₄ at room temperature. All polarization curves exhibit a plateau behavior in the voltage regime between 0.06 to 0.70 V vs. RHE. Here, the oxygen diffusion to the catalytic reaction center is the rate limiting process and is dependent on the rotating rate^{100, 101}. The mass transport diffusion controlled regime is followed by a transition region of mixed diffusional and kinetic control. Above 0.95 V vs. RHE the polarization curves became independent of the electrode rotating rate. The reaction rate is now kinetically controlled. The electrocatalytic conversion of oxygen drops to zero at the open circuit potential of around 1.0 V vs. RHE.

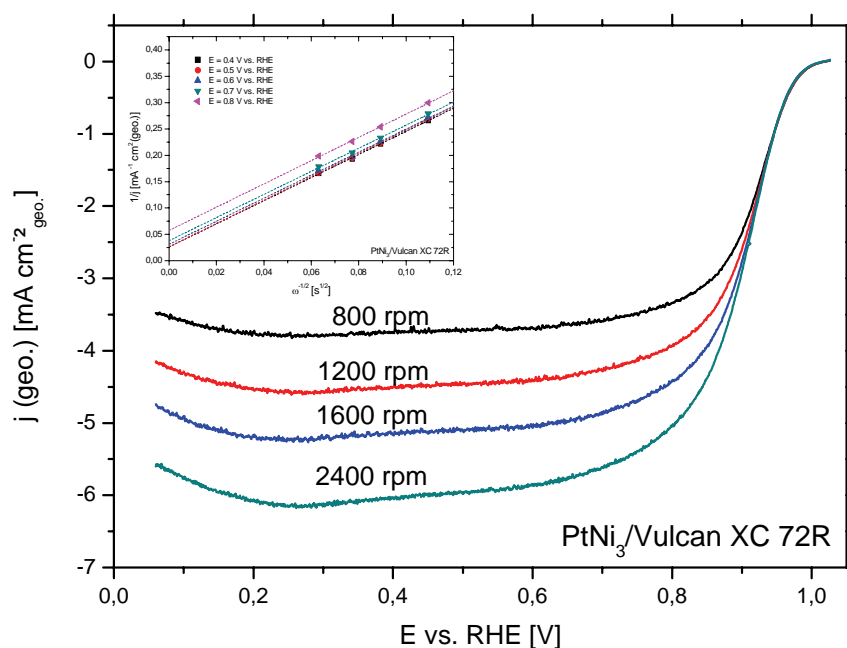


Figure 55 Polarization curves of dealloyed PtNi₃/Vulcan XC 72R at various rotating speeds in oxygenated 0.1 M HClO₄ at room temperature; inset: Koutecky – Levich Plot at various electrode voltages. Reproduced from reference¹⁰⁴ by permission of ECS – The Electrochemical Society.

Activity, structure and degradation of dealloyed PtNi₃ nanoparticle fuel cell electrocatalyst

In addition, we determined the number of transferred electrons for the oxygen reduction reaction using the Koutecky – Levich equation (eq. 11)^{100, 101}. The experimentally resulting “B Factor” was compared with the theoretic calculated for a four electron process.

$$\frac{1}{j} = \frac{1}{j_{\text{kinetic}}} + \frac{1}{j_{\text{diffusion}}} = \frac{1}{j_{\text{kinetic}}} + \frac{1}{(B \cdot \omega^{1/2})}$$

eq. 11
$$B = 0.62 \cdot n \cdot F \cdot D(\text{O}_2)^{2/3} \cdot \nu^{-1/6} \cdot c(\text{O}_2)$$

Here, j is the current density, j_{kinetic} and $j_{\text{diffusion}}$ is the kinetic and diffusion limiting current density and ω is the rotating rate. The “B Factor” is dependent on the experimental conditions and includes the oxygen solubility ($c(\text{O}_2)$) and the diffusivity ($D(\text{O}_2)$), the Faraday constant (F), the kinematic viscosity of the electrolyte (ν) and the number of transferred electrons (n). The theoretical value of the “B Factor” for a four electron oxygen reduction process is $0.467 \text{ mA cm}^{-2}_{\text{geo.}} \text{ s}^{1/2}$, using published data¹⁰². The experimental “B Factor” of the dealloyed PtNi₃ catalyst was calculated from the slope of the Koutecky – Levich Plot, shown in Figure 55 (inset). The mean value for the “B Factor” obtained from various electrode voltages is $0.454 \pm 0.003 \text{ mA cm}^{-2}_{\text{geo.}} \text{ s}^{1/2}$. The good agreement of the theoretical and experimental values (divergence < 3%) for the “B Factor” confirmed the suitability of the dealloyed PtNi₃ as an electrocatalyst for a direct four electron process of oxygen reduction in a PEM fuel cell.

Table 11 summarizes the mean particle size of the as synthesized and the ORR activities for dealloyed PtNi₃, Pt and Pt (HT) nanoparticle catalysts supported on Vulcan XC 72R.

Table 11 Comparison of mean particle size of the as synthesized and the ORR activities of dealloyed PtNi₃/Vulcan XC 72R, Pt/Vulcan XC 72R (HT) and Pt/Vulcan XC 72R nanoparticle catalysts. Reproduced from reference¹⁰⁴ by permission of ECS – The Electrochemical Society.

catalyst	mean particle size [nm]	ECSA [m ² g _{Pt} ⁻¹]	$j_{(\text{mass}, 0.9 \text{ V [RHE])}}$ [A mg _{Pt} ⁻¹]	$j_{(\text{specific}, 0.9 \text{ V [RHE])}}$ [μA cm _{Pt} ⁻²]
PtNi ₃ /Vulcan XC 72R	6.4 ± 1.9	19 ± 3	0.29 ± 0.06	1491 ± 280
Pt/Vulcan XC 72R (HT)	6.4 ± 2.0	17 ± 2	0.04 ± 0.01	237 ± 26
Pt/Vulcan XC 72R	2.3 ± 0.6	47 ± 3	0.13 ± 0.02	271 ± 30

Here, the dealloyed PtNi₃ catalyst shows a 7 – 8 times higher Pt mass based activity (j_{mass}) compared with pure heat treated Pt (HT) catalyst and a 2 – 3 times higher j_{mass} compared with pure, untreated Pt catalyst. The Pt surface area specific based activity (j_{specific}) of dealloyed PtNi₃ is still 6 – 7 times higher than that for Pt (HT) and 5 – 6 times higher than for untreated Pt. Thus, dealloyed PtNi₃ shows considerable ORR performance than pure Pt (HT) by similar mean particle size and pure, untreated Pt with a mean particle size of 2.3 nm. We suggest that the difference in the surface specific areas of 2 nm Pt and 6 nm Pt (HT) caused by the not completed electrochemical removing process of carbonous catalyst surface poisons for Pt(HT) catalyst which formed during the annealing. The resulting ORR activities of dealloyed PtNi₃ nanoparticles are significantly higher than those for Pt-Ni nanoparticle systems with a mean particle size up to 8 nm which reported in the literature^{21, 23, 40}.

4.2.4 Durability of dealloyed PtNi₃ nanoparticle catalyst

Two different stability voltage cycling tests were performed to examine the long-term durability of the dealloyed, highly active PtNi₃ catalyst, one simulating typical fuel cell operation conditions and another simulating strongly corrosive fuel cell start-up/shut-down operation conditions^{36, 52}. These long-term stability tests are accelerated degradation tests to simulate the long-term behavior of fuel cell electrocatalysts (more details in chapter 2.6.5 *Electrochemical long-term durability experiments*).

ORR activity. The bar diagram in Figure 56 sums up the Pt surface area specific based activities determined at 0.9 V vs. RHE for dealloyed PtNi₃/Vulcan XC 72R, Pt/Vulcan XC 72R and Pt/Vulcan XC 72R (HT) before and after both stability test experiments.

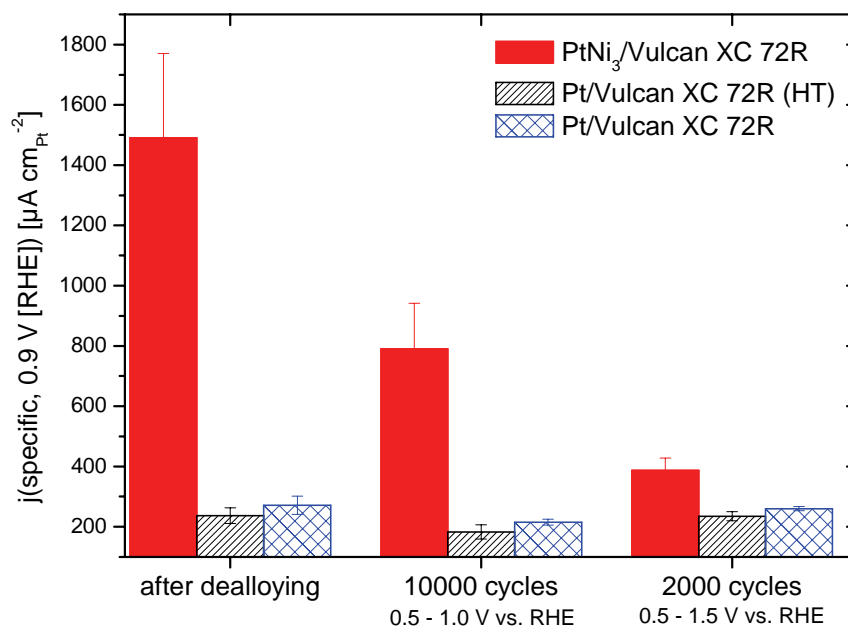


Figure 56 Comparison of the Pt surface area specific based activities (j_{specific}) at 0.9 V vs. RHE for dealloyed PtNi₃/Vulcan XC 72R, Pt/Vulcan XC 72R (HT), and Pt/Vulcan XC 72R after dealloying, after 10000 voltage cycles (0.5 – 1.0 V vs. RHE, 50 mV s⁻¹), and after 2000 voltage cycles (0.5 – 1.5 V vs. RHE, 50 mV s⁻¹). Reproduced from reference ¹⁰⁴ by permission of ECS – The Electrochemical Society.

The dealloyed active PtNi₃ catalyst shows clearly improved j_{specific} activities for ORR after both stability tests compared with the benchmark catalysts, commercial pure Pt and heat treated Pt (HT) catalysts. Furthermore, the dealloyed PtNi₃ catalyst exceeds the required U.S. Department of Energy (DoE) activity target 2015⁶ for j_{specific} after 10000 voltage cycles (0.5 – 1.0 V vs. RHE) established by RDE experiments and is still 4 – 5 times higher than the pure heat treated Pt (HT) catalyst and 3 – 4 times higher than the pure Pt catalyst. In addition, after 2000 voltage cycles (0.5 – 1.5 V vs. RHE) under corrosive condition the dealloyed PtNi₃ catalyst shows still almost 2 fold increase in j_{specific} than Pt and Pt (HT). Furthermore, in contrast to the pure Pt catalysts, the dealloyed PtNi₃ catalyst shows a drastic decrease in j_{specific} after both stability tests compared to the initial values. Dissolution of Ni from the Pt alloy core – shell nanoparticles induced a drop in the geometric strain of the Pt shell which initially led to the improved performance for ORR. The decrease of j_{specific} related clearly to the changes in the morphology and chemical composition of Pt

Activity, structure and degradation of dealloyed PtNi₃ nanoparticle fuel cell electrocatalyst

alloys (from Pt_{56±2}Ni_{45±2} to final Pt_{76±6}Ni_{24±6} after “lifetime” and Pt_{89±4}Ni_{11±4} after “start-up” testing established by EDS). The activity loss is associated with the change in morphological surface and the decreased compressive lattice strain of Pt-enriched shell of alloy particles. However, the absolute final values of j_{specific} are significantly higher than those for the benchmark pure Pt catalysts.

ECSA loss trend combined with mean particle size for the “lifetime” regime. Figure 57 and Table 12 show the Pt electrochemical active surface area (ECSA) trends and the change of the mean particle size during the “lifetime” voltage cycling (0.5 – 1.0 V vs. RHE, 50 mV s⁻¹) for the dealloyed PtNi₃, Pt and Pt (HT) catalysts.

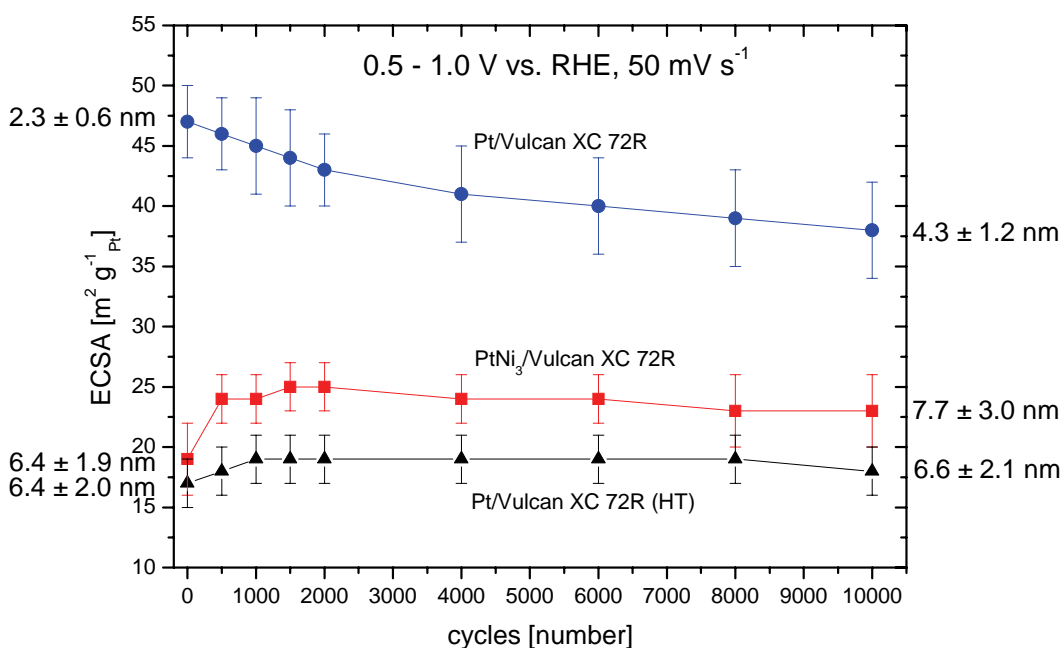


Figure 57 Comparison of Pt electrochemical active surface area (ECSA) for dealloyed PtNi₃/Vulcan XC 72 R (red squares), commercial pure Pt/Vulcan XC 72R (blue circulars), and heat treated Pt/Vulcan XC 72R (HT) (black triangles) combined with the initial (left side) and final (right side) mean particle sizes during the “lifetime” voltage cycling (0.5 – 1.0 V vs. RHE, 50 mV s⁻¹, 0.1 M HClO₄, room temperature). Reproduced from reference ¹⁰⁴ by permission of ECS – The Electrochemical Society.

Pure Pt/Vulcan XC 72R catalyst exhibits a higher initial value of ECSA than the heat treated Pt/Vulcan XC 72R (HT) and dealloyed PtNi₃/Vulcan XC 72R. This result is based on the different mean particle size for the as synthesized catalysts. Generally, a smaller particle size leads to a higher value

Activity, structure and degradation of dealloyed PtNi₃ nanoparticle fuel cell electrocatalyst

of ECSA and contrary^{49, 53, 103, 111}. Due to the similar initial mean particle sizes, PtNi₃ and Pt (HT) reveal similar ECSA values.

Table 12 Correlation of mean particle size and Pt electrochemical active surface area (ECSA) for PtNi₃/Vulcan XC 72 R, commercial pure Pt/Vulcan XC 72R, and heat treated Pt/Vulcan XC 72R (HT) after dealloying, “lifetime” (10000 voltage cycles, 0.5 – 1.0 V vs. RHE, 50 mV s⁻¹), and “start-up” (2000 voltage cycles, 0.5 – 1.5 V vs. RHE, 50 mV s⁻¹) stability testings. Reproduced from reference¹⁰⁴ by permission of ECS – The Electrochemical Society.

catalyst	after dealloying		after „lifetime” testing		after „start-up” testing	
	mean particle size ¹⁾	ECSA ^{2),4)}	mean particle size	ECSA ^{3),4)}	mean particle size	ECSA ^{3),4)}
	[nm]	[m ² g _{Pt} ⁻¹]	[nm]	[m ² g _{Pt} ⁻¹]	[nm]	[m ² g _{Pt} ⁻¹]
PtNi ₃ /Vulcan XC 72R	6.4 ± 1.9	19 ± 3	7.7 ± 3.0	23 ± 3	7.5 ± 2.0	25 ± 3
Pt/Vulcan XC 72R (HT)	6.4 ± 2.0	17 ± 2	6.6 ± 2.1	18 ± 2	6.8 ± 2.5	21 ± 1
Pt/Vulcan XC 72R	2.3 ± 0.6	47 ± 3	4.3 ± 1.2	38 ± 3	6.6 ± 1.4	24 ± 2

¹⁾ as synthesized

²⁾ mean value determined from 6 (= 3 „start-up” + 3 „lifetime”) independent measurements

³⁾ mean value determined from 3 independent measurements

⁴⁾ based on as synthesized Pt loading

During the “lifetime” voltage cycling, the ECSA of pure Pt decreased at 20 % from $47 \pm 3 \text{ m}^2 \text{ g}_{\text{Pt}}^{-1}$ to $38 \pm 3 \text{ m}^2 \text{ g}_{\text{Pt}}^{-1}$, associated with an increase of the mean particle size from initial $2.3 \pm 0.6 \text{ nm}$ to final $4.3 \pm 1.2 \text{ nm}$ (87 %). In contrast, Figure 57 and Table 12 show that no significant particle growth is observable for PtNi₃ and Pt (HT) after “lifetime” stability testing. In addition, the ECSA value increased slightly from $19 \pm 3 \text{ m}^2 \text{ g}_{\text{Pt}}^{-1}$ to $23 \pm 3 \text{ m}^2 \text{ g}_{\text{Pt}}^{-1}$ (21 %) and from $17 \pm 2 \text{ m}^2 \text{ g}_{\text{Pt}}^{-1}$ to $18 \pm 3 \text{ m}^2 \text{ g}_{\text{Pt}}^{-1}$ (8 %) for PtNi₃ and Pt (HT). The increasing ECSA during the first thousand voltage cycles likely comes from the Pt surface reorganization and the removal of carbonous catalyst surface poisons, which formed during the annealing protocol. Selective dissolution of Ni ions from the catalyst continued during voltage cycling; this follows from the change in chemical composition from Pt_{56±2}Ni_{45±2} to final Pt_{76±6}Ni_{24±6}. The Ni loss likely caused additional surface roughness which, in turn, initially increased the ECSA. This result is in good agreement with our previous reports for long-term stability experiments of other carbon supported Pt, and dealloyed PtCu₃ and PtCo₃ nanoparticle catalysts and underline the assumption of an existing critical quasi stable particle size^{36, 52}. In summary, once the critical quasi stable particle size (D_{critical}) has been achieved, the ECSA loss is primarily caused by carbon corrosion associated with support corrosion and particle detachment. This leads to a slowdown of the ECSA loss curve during the stability test.

Activity, structure and degradation of dealloyed PtNi₃ nanoparticle fuel cell electrocatalyst

The experimentally determined D_{critical} was 3 – 4 nm after “lifetime” stability test conditions^{36, 52}. The PtNi₃ and Pt (HT) catalysts show an initial mean particle size of 6.4 nm ± 2.0 nm. Based on the model of D_{critical} , the mean particle size of the PtNi₃ and Pt (HT) catalysts should not change after “lifetime” stability test because D_{critical} has been reached before the “lifetime” stability test. The ESCA loss is controlled by carbon corrosion associating with particle detachment. In contrast, the untreated Pt catalyst with an initial mean particle size of 2.3 ± 0.6 nm showed a particle growth as predicted. Both predictions are confirmed by the presented experimental data.

ECSA loss trend combined with mean particle size for the “start-up” regime. Figure 58 and Table 12 show the change of the ECSA and mean particle size during the “start-up” voltage cycling (0.5 – 1.5 V vs. RHE, 50 mV s⁻¹) for the dealloyed PtNi₃, Pt and Pt (HT) catalysts. Here, all catalysts attained similar final mean particle sizes of 6 – 8 nm.

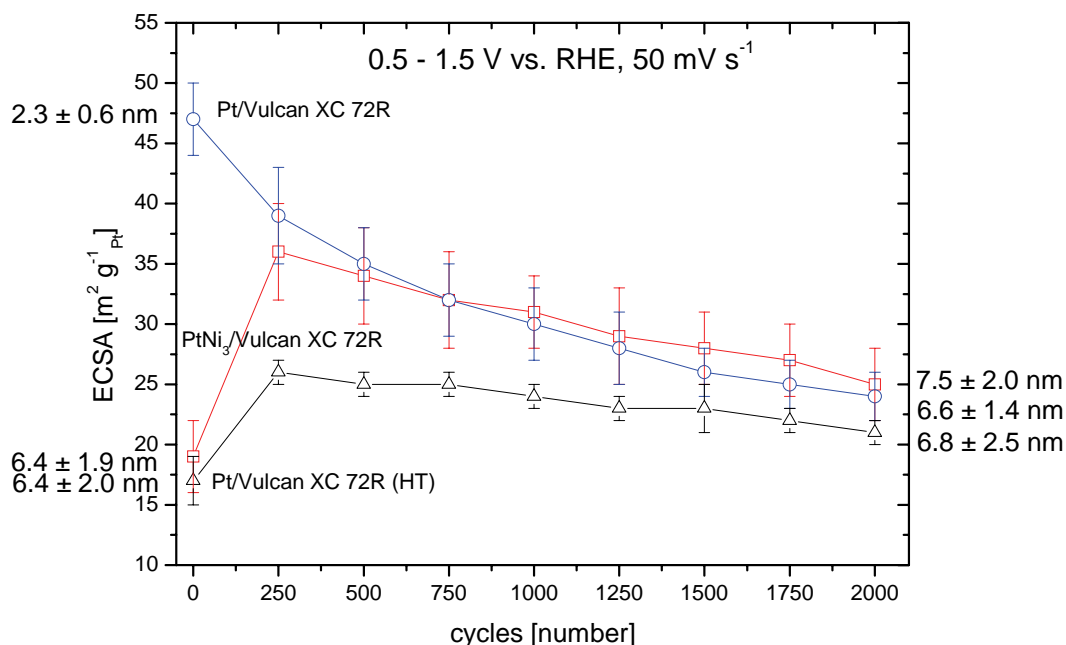
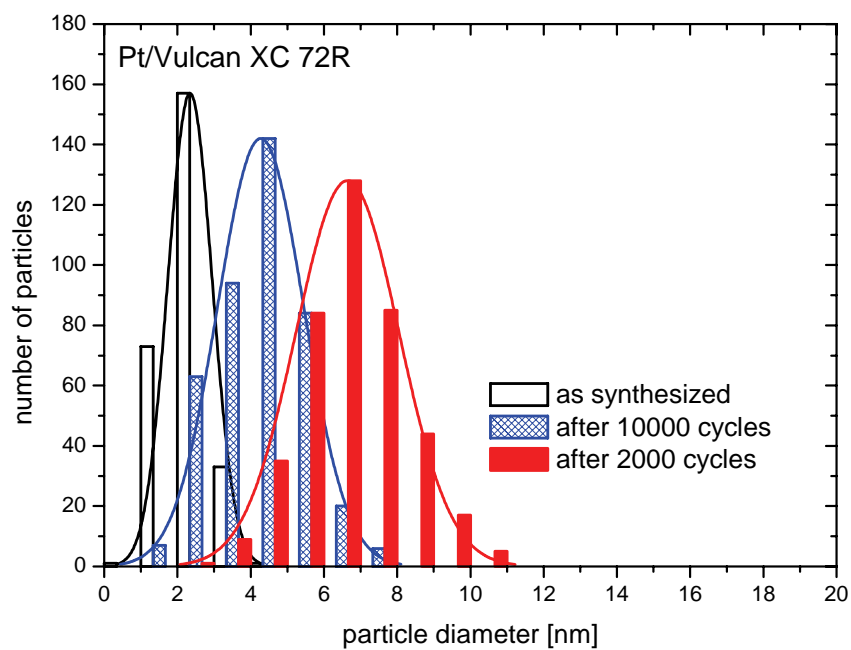
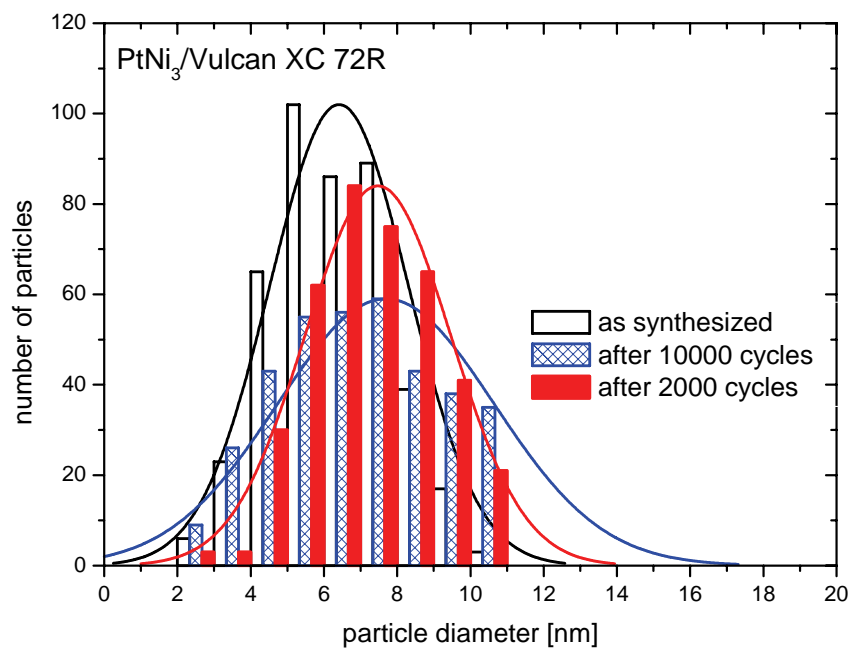


Figure 58 Comparison of Pt electrochemical active surface area (ECSA) for dealloyed PtNi₃/Vulcan XC 72 R (red squares), commercial pure Pt/Vulcan XC 72R (blue circulars), and heat treated Pt/Vulcan XC 72R (HT) (black triangles) combined with the initial (left side) and final (right side) mean particle sizes during the “start-up” voltage cycling (0.5 – 1.5 V vs. RHE, 50 mV s⁻¹, 0.1 M HClO₄, room temperature). Reproduced from reference¹⁰⁴ by permission of ECS – The Electrochemical Society.

The run of the ECSA loss curve was clearly different for the pure, untreated Pt catalyst with the initial mean particle size of 2.3 ± 0.6 nm compared with those for Pt (HT) and PtNi₃ catalysts with a 3 times larger initial size (6.4 ± 2.0 nm). The Pt catalyst of 2.3 nm only showed a steady decrease of the ECSA during the “start-up” stability test. This sloping ECSA run was related with the particle growth from 2.3 ± 0.6 nm to 6.6 ± 1.4 nm. In contrast, the PtNi₃ and Pt (HT) catalysts showed an increase of the ECSA during the first 250 voltage cycles and subsequently a continuous decrease of the ECSA. Here, the mean particle size grew very slightly from 6.4 ± 2.0 nm to 6.8 ± 2.5 nm and 7.5 ± 2.0 nm for Pt (HT) and PtNi₃ catalysts. This small particle growth is negligible. The increase of the ECSA values up to 250 voltage cycles is likely based on the Pt surface reorganization processes, the removal of surface poisoning which formed by the synthesis and in the case of the Pt alloy an increasing particle surface roughness resulted from the strong dissolution / dealloying of the non noble metal Ni. Above 250 voltage cycles the decreasing ECSA is based on the carbon corrosion. All together leads to a slight increase of ECSA after “start-up” stability testing. The strong dealloying is indicated by the change in chemical composition from Pt_{56±2}Ni_{45±2} after dealloying procedure to generate the active catalyst to Pt_{89±4}Ni_{11±4}. The drastic Ni loss is due to the high voltage range up to 1.5 V vs. RHE and in line with the relative dissolution potential. The results for the final mean particle sizes are in a good agreement with our previously experimental determined values for other Pt alloy and pure Pt catalyst systems^{36, 52}.

Particle size distributions. Figure 59 shows the particle size distributions for PtNi₃/Vulcan XC 72 R, commercial pure Pt/Vulcan XC 72R, and heat treated Pt/Vulcan XC 72R (HT) as synthesized and after the two voltage cycling stability tests. Only a slight change of the mean particle size for the PtNi₃ and Pt (HT) catalysts is observable after both stability tests.



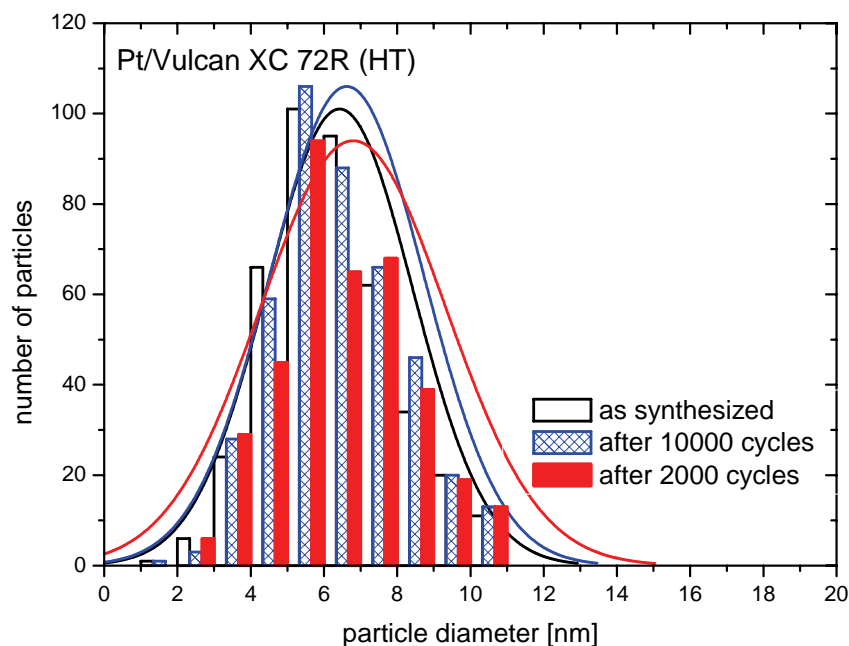


Figure 59 Evolution of the particle size distributions for PtNi₃/Vulcan XC 72R, commercial pure Pt/Vulcan XC 72R, and heat treated Pt/Vulcan XC 72R (HT) as synthesized, after 10000 “lifetime” voltage cycles (0.5 – 1.0 V vs. RHE, 50 mV s⁻¹), and after 2000 “start-up” voltage cycles (0.5 – 1.5 V vs. RHE, 50 mV s⁻¹) experiments. The bar charts are shown with x-offset. Reproduced from reference ¹⁰⁴ by permission of ECS – The Electrochemical Society.

It is noted that particles below 2.5 nm were not found after the “start-up” stability tests due to the voltage cycling up to 1.5 V vs. RHE and the relation between the particle size and dissolution potential, given by the combination of Nernst and Gibbs-Thomson equation (see eq. 5)^{49, 55}. Meanwhile, Pt catalyst of initial 2.3 ± 0.6 nm grew significantly to larger particles after both stability testings. The attained mean particle size depends on the critical quasi stable particle size and is correlated to the maximum voltage, scan rate and the number of cycles (equal to time).

4.2.5 Conclusions

In this chapter, we have examined the catalytic ORR activity and electrode voltage cycling durability of a dealloyed PtNi₃ nanoparticle catalyst under “lifetime” and “start-up” fuel cell conditions. As benchmark catalysts, we used a heat treated pure Pt (HT) nanoparticle catalyst with similar mean particle size in order to exclude particle size effects as well as a commercial pure Pt catalyst with 3 times smaller mean particle size. Based on the results of the electrochemical experiments, composition and particle size distributions we conclude, that

- the initial voltammetric Ni dissolution (Ni dealloying) is an electrochemical activation process, which leads to a catalytically active Pt-enriched nanoparticle catalyst with in time-stable Pt-resembling cyclic voltammograms.
- the dealloyed PtNi₃ nanoparticle catalyst exhibits a 7 – 8 fold increase in ORR Pt mass based activity compared to the heat treated Pt catalyst with comparable particle size; and that PtNi₃ shows a 2 – 3 times higher platinum mass based activity than commercial Pt nanoparticles. In terms of their Pt surface area ORR activity, the dealloyed Pt-Ni catalyst shows a 6 – 7 fold and a 5 – 6 fold higher activity compared to pure Pt (HT) and commercial non-annealed pure Pt, respectively.
- the dealloyed PtNi₃ nanoparticle catalyst shows 4 – 5 times and 3 – 4 times higher platinum surface area specific based activities after “lifetime” stability test with 10000 voltage cycles between 0.5 – 1.0 V vs. RHE with a scan rate of 50 mV s⁻¹ in deaerated 0.1 M HClO₄ compared to pure Pt (HT) and commercial pure Pt catalysts.
- the ECSA loss for PtNi₃ nanoparticle catalyst is reduced during voltage cycling testing due to the larger and stable mean particle size.

5 Thermal stability of supported platinum nanoparticle catalysts: in situ studies

This chapter is based on the publication

Hasché, F.; Oezaslan, M.; Strasser, P.,

In Situ Observation of the Thermally Induced Growth
of Platinum-Nanoparticle Catalysts Using High-Temperature X-ray Diffraction.

ChemPhysChem **2012**, 13, (3), 828-834

<http://dx.doi.org/10.1002/cphc.201100857>

Reproduced by permission of John Wiley and Sons.

Fundamental understanding and deliberate control of structural and morphological changes of catalytically active metal nanoparticles¹¹²⁻¹¹⁴ under reactive conditions is of general importance for a wide range of reaction processes in heterogeneous and electrochemical catalysis, such as water-gas shift reaction¹¹⁵, NO oxidation¹¹⁶, ammonia decomposition¹¹⁷, hydrodesulfurization¹¹⁸, methanation¹¹⁹, oxygen evolution¹²⁰, or the oxygen reduction reaction^{5, 15, 17, 36, 51, 52, 58, 89, 104, 107, 108, 121-125}. The long-term durability and, associated with it, the activity of metal nanoparticle catalysts are controlled by diverse effects pertaining to loss of catalytic surface area such as particle coalescence, particle agglomeration, or to a loss of active catalytic centers caused by changes in the catalyst structure, by decomposition of catalysts, or by site poisoning. In particular, metal particle growth is a very common reason of catalyst deactivation leading to reduced catalyst dispersions and metal atom utilization and hence results in reduced metal mass based activity and catalytic active surface area^{53, 105, 111}. The current challenge in controlling the stability of catalytic metal nanoparticles is to identify the dominant degradation mechanisms under a chosen set of catalytic operation conditions in order to arrive at a rational design of more stable nanoparticles.

In this chapter, we have performed in situ experiments to monitor the thermal migration and coalescence of carbon supported Pt nanoparticles (Pt/C) with particle sizes below 3 nm as a mostly used cathode fuel cell electrocatalyst in absence of an electric field and electrolyte. The goal was to unambiguously

evaluate the extent of metal particle coarsening as function of relevant external experimental parameters. We have observed the Pt particle growth dynamics using a lab-based high temperature X-ray diffraction (HT-XRD) setup in parallel beam geometry (see Figure 11)²⁷. The in situ HT-XRD experiments were carried out at various Pt loadings with different carbon support materials and gas atmospheres under typical low (80 °C) and high (160 °C) temperature proton exchange membrane fuel cell (PEMFC) operation conditions^{60, 83}. Our results show that particle growth occurs rapidly with decreasing BET surface area and/or increasing Pt loading at high temperature. The mechanism of particle growth by induced thermal treatment is caused by agglomeration and coalescence until a critical (quasi stable) particle size is reached. Here, the particle growth depends on the induced temperature, the initial particle size and the interparticle distance (λ).

The behavior of particle size growth was examined in situ on different commercially available carbon supported Pt nanoparticle catalysts observed by HT-XRD. Table 13 summarizes the Pt/C materials with their initial Pt loadings and BET surface areas. In addition to one high surface area carbon (HSAC) supported Pt material (Pt/HSAC), a number of Vulcan XC 72R supported Pt catalysts with various loadings of 10, 20, and 46 wt. % were examined. The Pt/HSAC material showed a three times higher BET surface area compared with the Pt/Vulcan XC 72R at similar Pt loading.

Table 13 Various Pt loadings and BET surface areas of Pt nanoparticle catalysts. Reproduced from reference ¹²⁶ by permission of John Wiley and Sons.

catalyst	BET surface area [m ² g ⁻¹]	platinum loading [wt.%]
Pt(10 wt.)/Vulcan XC 72R	185	10.0
Pt(20 wt.)/Vulcan XC 72R	151	20.0
Pt(46 wt.)/Vulcan XC 72R	99	46.7
Pt(46 wt.)/HSAC	290	45.9

5.1 Crystallite growth rate in dependence on BET surface area and treatment temperature

Figure 60 shows the experimental time resolved XRD profiles of Pt(46 wt.)/Vulcan XC 72R at 160 °C for 155 hours under N₂ atmosphere. The XRD reflections at $2\Theta = 39.8^\circ$ and 46.2° correspond to (111) and (200) lattice planes of pure face centered cubic (fcc) platinum with a space group of Fm3m⁸⁷. The first scan (#1) was detected at 30 °C and represents the initial crystal structure and mean crystallite size before heating up to 160 °C. Scan #2 represents the first XRD profile at 160 °C. A very slight reflection shift to smaller 2Θ values signified a slight thermal expansion of the fcc Pt lattice parameter at 160 °C compared to that in scan #1 at 30 °C. In addition, the broad reflections for Pt(46 wt.)/Vulcan XC 72R indicated small crystallite size.

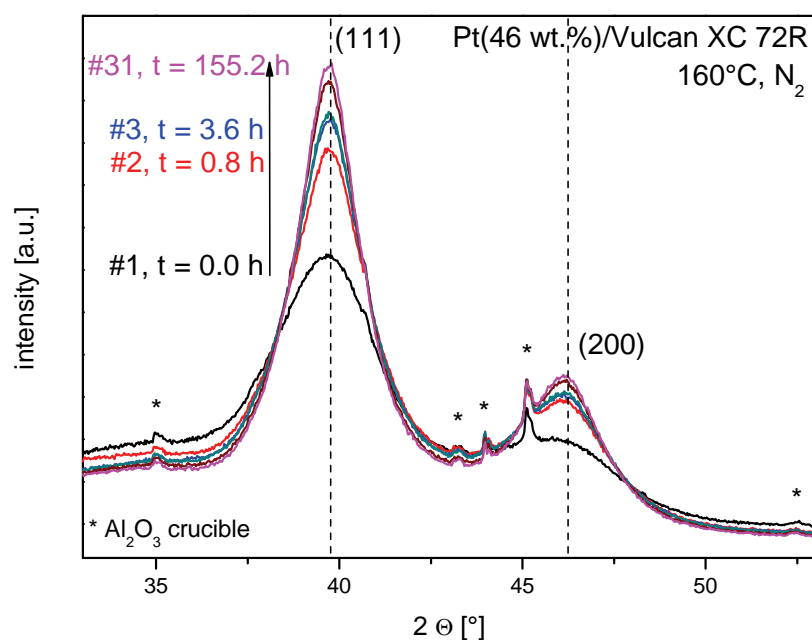


Figure 60 Series of time resolved XRD profiles for Pt(46 wt.)/Vulcan XC 72R nanoparticle catalyst during the thermal treatment at 160 °C for 155 hours in N₂ atmosphere. Scan #1 was measured at 30 °C and the scan numbers correlate with Figure 2. Vertical dotted lines denote reference powder diffraction pattern (PDF) of pure fcc Pt, PDF(Pt)#00-004-0802⁸⁷. Reproduced from reference¹²⁶ by permission of John Wiley and Sons.

The series of XRD profiles in Figure 60 shows that over the course of the thermal treatment experiment the (111) and (200) reflections became sharper and more intense due to the growth of the Pt crystallites at 160 °C in N₂ atmosphere. The small, sharp reflections at $2\Theta = 35.0^\circ$, 43.3° , 44.0° , 45.1° , and 52.5° emerged from the Al₂O₃ crucible, which served as sample holder and internal standard for all HT-XRD measurements.

We calculated the mean crystallite size from the (111) and (200) reflections using the size distribution and shape-independent integral breath method⁸⁴. The integral breath method introduced by Laue is the ratio of the integrated intensity to the intensity at the maximum. Figure 61 shows the resulting crystallite size growth curves for Pt(46 wt.)/Vulcan XC 72R at 80 °C and 160 °C in N₂ atmosphere. The scan numbers in Figure 61 correlate with the XRD profiles in Figure 60.

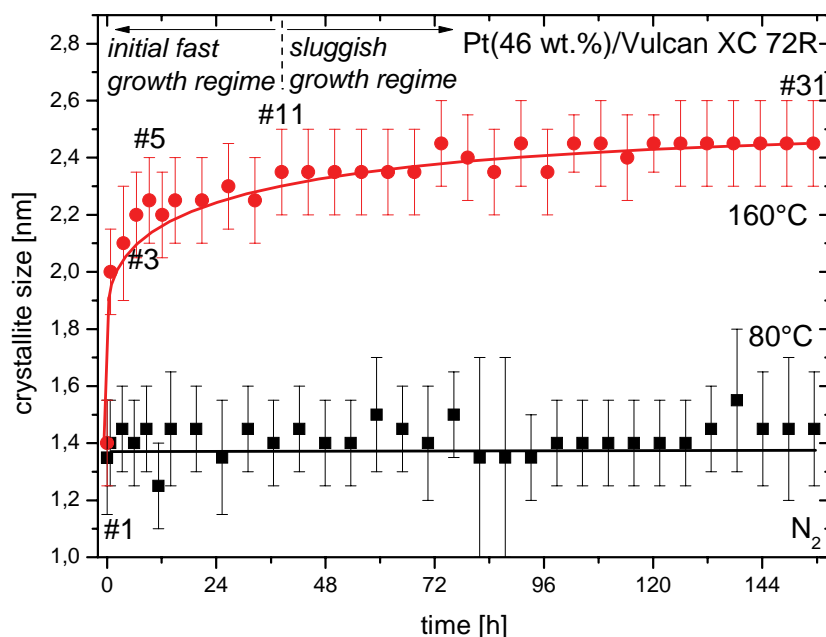


Figure 61 Mean crystallite size of platinum versus holding time at 80 °C (black squares) and 160 °C (red circles) for Pt(46 wt.)/Vulcan XC 72R nanoparticle catalyst in N₂ atmosphere. The initial mean crystallite size was determined at 30 °C. The scan numbers correlate with XRD profiles in Figure 60. Reproduced from reference¹²⁶ by permission of John Wiley and Sons.

The thermal treatment at 80 °C for 155 hours in N₂ atmosphere only showed very slight crystallite size growth for Pt(46 wt.)/Vulcan XC 72 R (see

black squares in Figure 61). However, after 155 hours at 160 °C the crystallites grew significantly from 1.4 ± 0.2 nm to 2.5 ± 0.2 nm approaching asymptotically a quasi stable size regime (see Figure 61, red circles). From the parabolically shaped growth curve at 160 °C two growth regimes can be identified. (I) Initial fast growth regime; the crystallite size increased by 50 % after 4 hours (scan #3) and by 68 % after 38 hours (scan #11). (II) Sluggish growth regime; the crystallite size growth was clearly slowed down (only 7 % between 38 and 155 hours, more than 4 days).

Unlike to the results of Pt(46 wt.)/Vulcan XC 72R, the Pt(46 wt.)/HSAC catalyst with a BET surface area of $290 \text{ m}^2 \text{ g}^{-1}$ revealed a very different particle growth behavior during thermal treatment. Figure 62 shows the calculated mean crystallite size for Pt(46 wt.)/HSAC versus holding time, obtained from the HT-XRD profiles (not shown) at 80 °C and 160 °C under N_2 atmosphere. The first measurement was again recorded at 30 °C to determine the initial crystallite size for the later comparison.

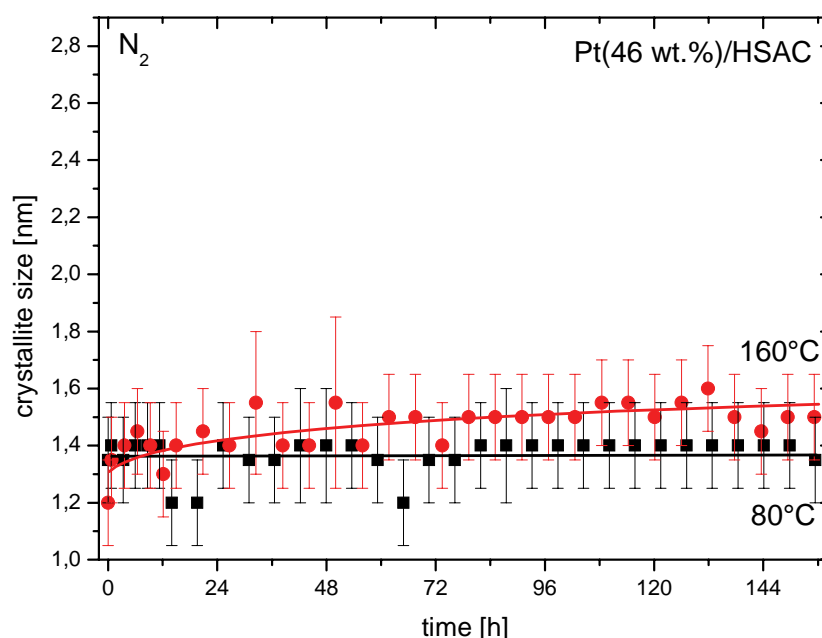


Figure 62 Mean crystallite size of platinum versus holding time at 80 °C (black squares) and 160 °C (red circles) for Pt(46 wt.)/HSAC nanoparticle catalyst under N_2 atmosphere. The initial mean crystallite size was determined at 30 °C. Reproduced from reference ¹²⁶ by permission of John Wiley and Sons.

Only a very slight increase of the mean crystallite size from 1.2 ± 0.2 nm to 1.5 ± 0.2 nm was observed at 160 °C (red circles in Figure 62), whereas the crystallite remained largely unchanged at 80 °C for 155 hours (black squares in Figure 62) under N₂ atmosphere.

More quantitatively, the mean crystallite size increased by 75 % for the lower BET surface area support (Vulcan XC 72R), but only by 25 % for the higher BET surface area support (HSAC) at comparable Pt loading under otherwise identical conditions. These points out the significant role of the BET surface area on the thermal migration/coalescence behavior of particles, as shown in Figure 63.

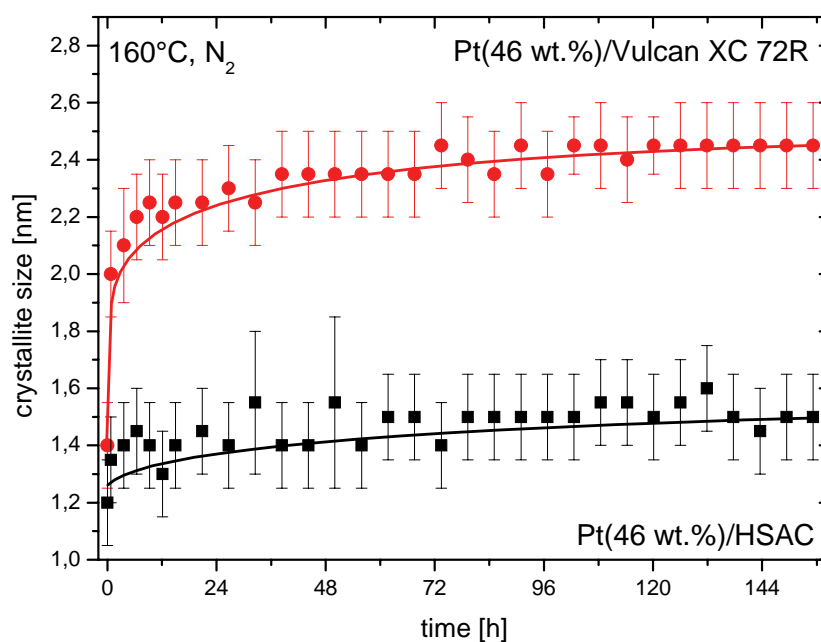


Figure 63 Mean crystallite size of platinum versus holding time at 160 °C for Pt(46 wt.)/Vulcan XC 72R (red circles) and Pt(46 wt.)/HSAC (black squares) nanoparticle catalysts under N₂ atmosphere. The initial mean crystallite size was determined at 30 °C. Reproduced from reference ¹²⁶ by permission of John Wiley and Sons.

We concluded that the crystallite growth is strongly controlled by the BET surface area of the support at high temperature. The crystallite growth mechanism is likely based on thermal diffusion/migration, agglomeration and subsequent coalescence of particles on the carbon surface.

To support our conclusion, time resolved ex situ TEM measurements were performed to investigate the rate of particle size growth. A TEM grid was prepared with a Pt(46 wt.)/Vulcan XC 72 R catalyst. After the initial particle size was determined, the grid was thermally treated in the HT-XRD heating chamber at 160 °C under N₂ atmosphere (see Figure 64).

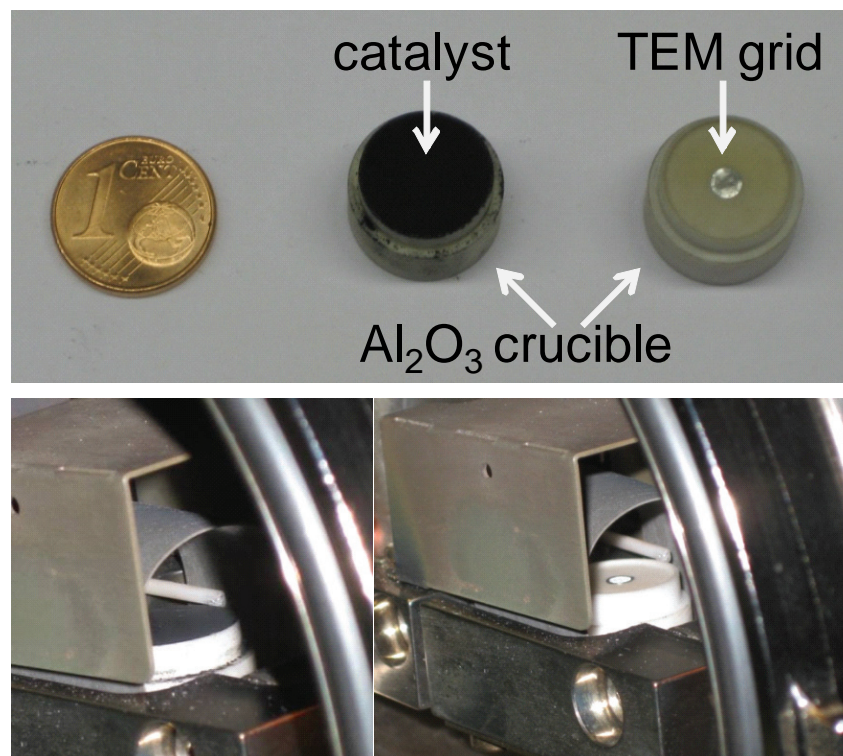


Figure 64 Top: TEM grid versus catalyst sample setup. Bottom: HT-XRD heating chamber setup with Al₂O₃ crucible with catalyst sample (left side) and TEM grid (right side). Reproduced from reference ¹²⁶ by permission of John Wiley and Sons.

After 4 hours, the grid was transferred back and forth between the microscope and heating chamber to determine the particle size. The changes of particle sizes were monitored after 4, 27, and 66 hours at 160 °C. Figure 65 shows the corresponding TEM images and the absolute mean particle sizes obtained from the time resolved ex situ TEM experiments.

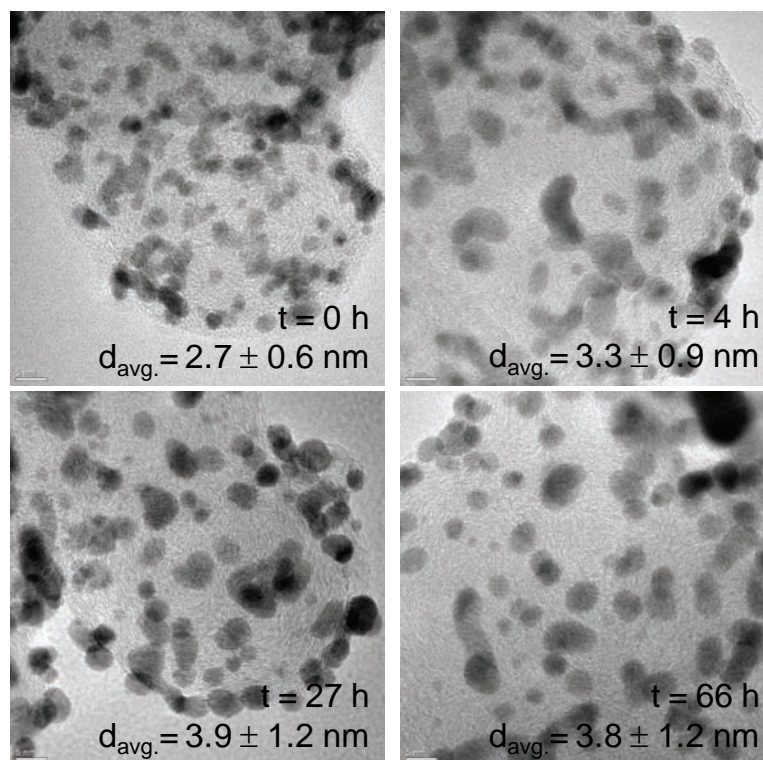


Figure 65 TEM images and mean particle sizes ($d_{\text{avg.}}$) for Pt(46wt.)/Vulcan XC 72R (scale bar of 5 nm) nanoparticle catalyst after thermal treatment at 160 °C in N₂ atmosphere, corresponding to Figure 66. Reproduced from reference ¹²⁶ by permission of John Wiley and Sons.

Figure 66 compares the normalized size growth versus holding time established by the in situ HT-XRD (black squares) and ex situ TEM (red circles) experiments. The thermally induced size growth trajectories reveal similar growth rates. Over 90 % of the total growth occurs after 27 hours thermal treatment at 160 °C in N₂ atmosphere. Figure 66 shows a significant difference between the final and normalized size growth after 66 hour at 160 °C under N₂ atmosphere established by XRD (1.4 ± 0.2 nm to 2.4 ± 0.2 nm, total growth of 68 %) and TEM (2.7 ± 0.6 nm to 3.8 ± 1.2 nm, total growth of 41 %).

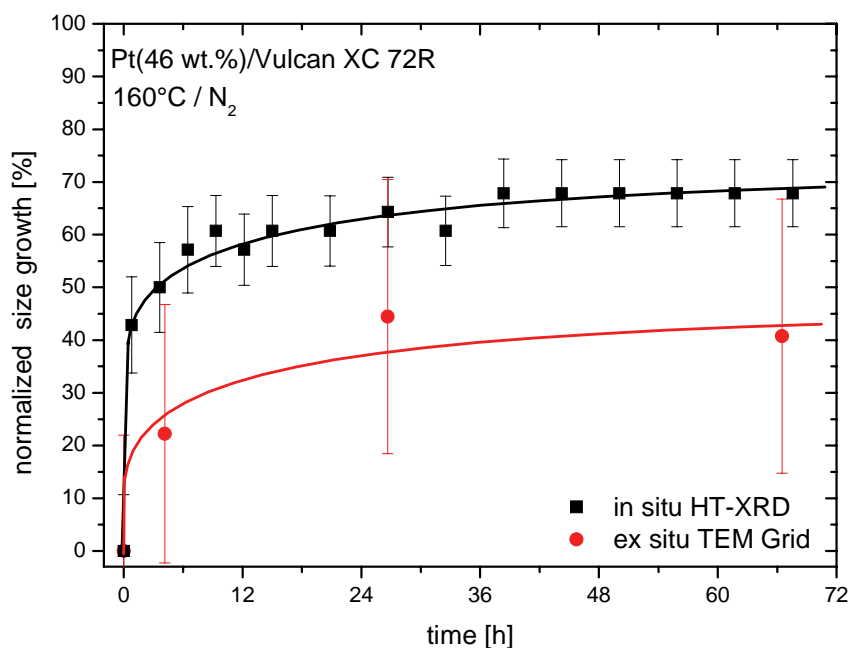


Figure 66 Evolution of the normalized size growth versus holding time at 160 °C for Pt(46 wt.)/Vulcan XC 72R established by in situ HT-XRD (black squares) and ex situ TEM (red circles) experiments. Reproduced from reference ¹²⁶ by permission of John Wiley and Sons.

This can be explained by the various XRD and TEM measurement techniques. Unlike to XRD method, around 400 particles were evaluated from various TEM images to determine statistically the number average particle size. The time resolution for the particle size growth is clearly limited due to the time-consuming number of TEM measurements and low statistic. Furthermore, a significant difference is to find in the sample preparation. The particles of few nano grams are supported and strongly dispersed on the TEM grid, while the catalyst powder of 5 – 10 mg is in the crucible (see Figure 64). For the XRD measurements the relative size error (10% to 15%) of the particle ensemble is based on the experimental setup. Generally, the error values of the crystallite size can be reduced with increasing measurement time, but the information about the dynamic behavior of crystallite size growth gets lost. So, the chosen parameters are a compromise between measurement error and time resolution. In summary, the in situ XRD experiments are more time resolved for an accurate dynamic size growth behavior compared to the ex situ TEM experiments. Due to the inert gas environment during the in situ XRD experiments, we exclude the formation of amorphous Pt oxide.

5.2 Crystallite growth rate in dependence on the platinum loading

The influence of Pt loading on the crystallite growth curves at 10, 20, and 46 wt.% Pt/Vulcan XC 72R was studied at 160 °C under N₂ atmosphere, shown in Figure 67. The corresponding BET surface areas were shown in Table 13. Table 14 sums up the results of mean crystallite size for different Pt/C materials before and after thermal treatment.

Table 14 Mean crystallite size of platinum for different Pt/C materials before and after thermal treatment at 80°C and 160°C for 155 hours under N₂ atmosphere and the interparticle distances (λ). Reproduced from reference ¹²⁶ by permission of John Wiley and Sons.

catalyst	λ [nm]	mean crystallite size [nm]			
		before	after 155 h / 80 °C	before	after 155 h / 160 °C
Pt(10 wt.%)/Vulcan XC 72R	14.4 ± 2.3	--	--	1.9 ± 0.3	2.1 ± 0.3
Pt(20 wt.%)/Vulcan XC 72R	8.5 ± 0.9	--	--	1.9 ± 0.2	2.2 ± 0.2
Pt(46 wt.%)/Vulcan XC 72R	2.1 ± 0.3	1.4 ± 0.2	1.5 ± 0.2	1.4 ± 0.2	2.5 ± 0.2
Pt(46 wt.%)/HSAC	3.6 ± 0.6	1.4 ± 0.2	1.4 ± 0.2	1.2 ± 0.2	1.5 ± 0.2

All observed growth curves show a complex, nonlinear behavior and can be explained by the thermally induced diffusion limited migration, agglomeration and coalescence of individual Pt particles on the surface of the carbon.

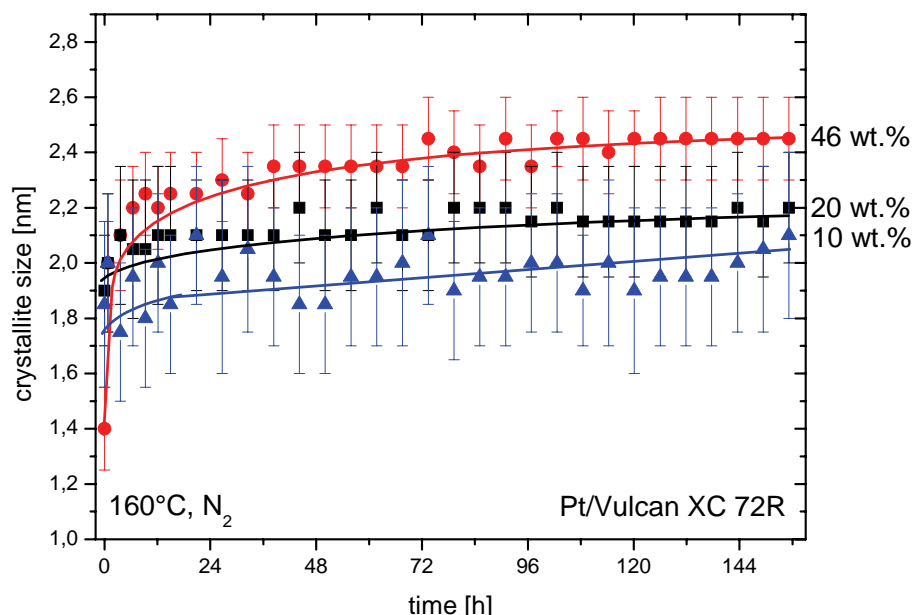


Figure 67 Dependence of the Pt loading with 46 wt.% (red circles), 20 wt.% (black squares), and 10 wt.% (blue triangles) for Pt/Vulcan XC 72R on the mean crystallite size growth during the holding time at 160 °C under N₂ atmosphere. The initial mean crystallite size for each catalyst was determined at 30 °C. Reproduced from reference ¹²⁶ by permission of John Wiley and Sons.

5.3 Effects of the temperature and the interparticle distance

The different growth trajectories can be described as a function of the temperature, the initial particle size, and the interparticle distance (λ). From the experimental results it evidence that a minimum temperature is necessary to initialize the thermal crystallite growth process by given initial particle size. The growth process occurs for small particles earlier than that for large particles. We suggest that the required temperature is in a range from 120 °C and 160 °C for particles below 3 nm. The results are in line with in the literature published values for particles above 3 nm with a minimum temperature of 200 °C – 300 °C¹²⁴. This explains the observation of a critical (quasi stable) particle size (around 3 nm) for Pt(46 wt.)/Vulcan XC 72 R at 160 °C under N₂ atmosphere. Further particle growth is thus excluded by elevated temperature of 160 °C¹²⁴.

We have proposed the interparticle distance (λ) as a controlling parameter for thermal growth. The interparticle distance (λ) represents the distance between two particles for a coalescence which is affected by the control parameters (initial particle size, BET surface area, and metal loading). So, the interparticle distance translates the different control parameters in only one parameter (λ) and allows us to a direct comparison of the various Pt/C materials. We assume for the calculation of λ (see 7.3 *Model for the calculation of the interparticle distance (λ)*) that all particles exhibit a spherical shape. The particles are monodispersed and distributed homogenously on the carbon support (see Figure 68).

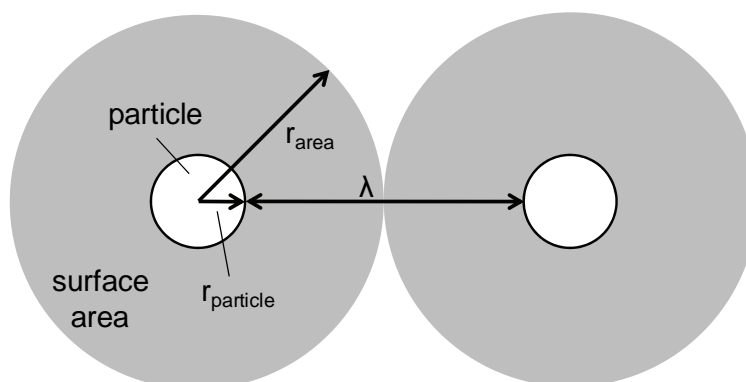


Figure 68 Model for the calculation of the interparticle distance (λ) between two particles. Spherical particles are assumed to be distributed homogeneously on carbon support. Reproduced from reference ¹²⁶ by permission of John Wiley and Sons.

Table 14 reports the estimated values of the interparticle distance (λ) for the different Pt/C materials based on the initial mean crystallite size before thermal treatment at 160 °C (column 6 in Table 14), the BET surface areas, and Pt loadings (see Table 13). Figure 69 illustrates the relative change in crystallite size versus the calculated interparticle distance for various tested Pt/C catalysts after thermal treatment at 160 °C for 155 hours in N₂ atmosphere probed by in situ HT-XRD. The catalysts with low Pt loading (10 wt.% and 20 wt.%) reveal a slight change in crystallite size (increased by 11% and 16%) compared to those at high Pt loading (46 wt.%, increased by 25% and 75%), shown in Table 14. This can be described by the longer interparticle distance of the supported nanoparticles (7 times larger for Pt(10 wt.%)/Vulcan XC 72R compared to that for Pt(46 wt.%)/HSAC) along the carbon support surface at given initial crystallite size. The effect of λ is clear on the thermal stability of supported particles. Generally, an increase of λ leads to a reducing size growth induced by thermal treatment. At low metal loadings, particle diffusion/migration and coalescence require more time to reach the same critical (quasi stable) particle size compared with high metal loadings.

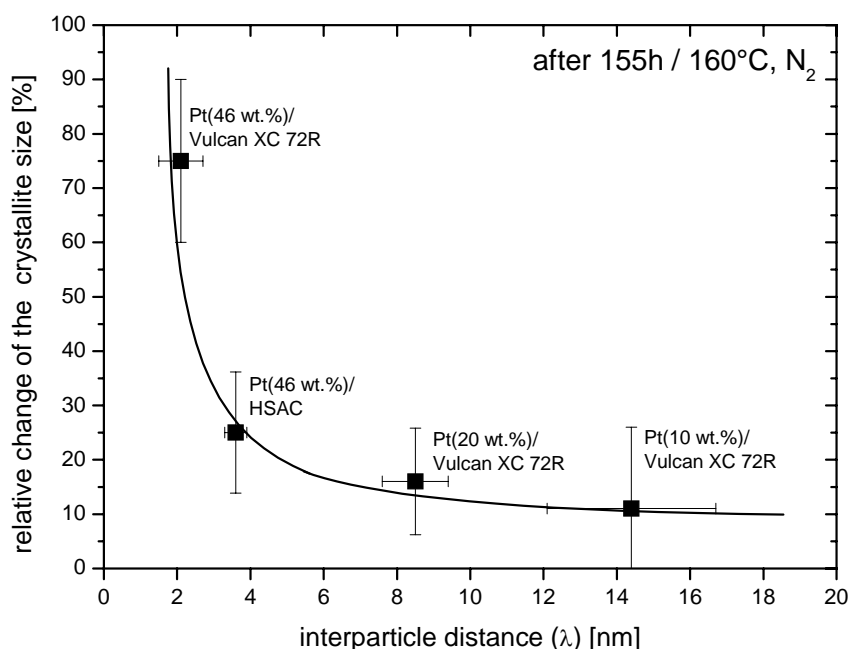


Figure 69 Relative change in crystallite size after thermal treatment at 160 °C in nitrogen atmosphere after 155 hours versus the interparticle distance (λ) for various carbon supported Pt nanoparticle materials. λ represents the ideal distance between the nanoparticles on the support surface. Reproduced from reference¹²⁶ by permission of John Wiley and Sons.

Figure 70 illustrates the particle growth in dependence on the BET surface area with similar metal loading and initial size. Here, the interparticle distance (λ) of the nanoparticles grows with increasing BET surface area or increased corrugated surface and defects ($\lambda_1 < \lambda_2$).

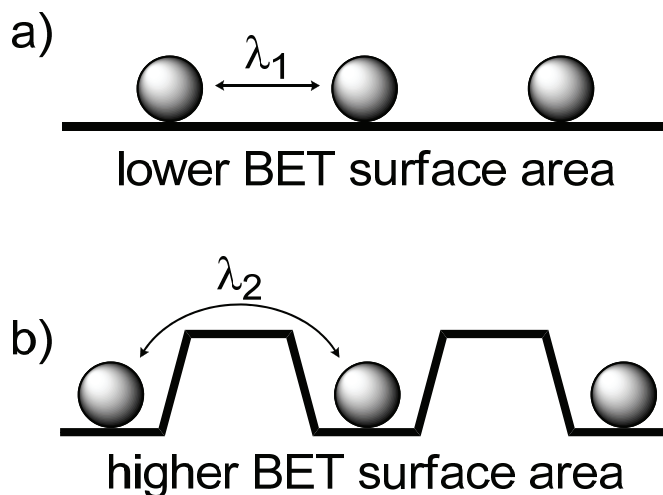


Figure 70 Illustration of Pt particle growth in dependence on BET surface area with similar metal loading and initial size. (a) lower and (b) higher BET surface area. The interparticle distance of the nanoparticles (λ) increases with increasing BET surface area. Reproduced from reference ¹²⁶ by permission of John Wiley and Sons.

The experimental results in Figure 63 in combination with Table 14 underline the predictions of the presented model and the effects of λ on the thermal stability of nanoparticles. The lower BET surface area catalyst with λ_1 exhibits an increased growth rate compared to that of the higher BET surface area catalyst with λ_2 . So, all experimental results are in line with the calculated λ . A higher value of λ increases the thermal particle size stability for supported nanoparticles. The control factors and adjustment values are the particle loading, BET surface area and initial particle size.

5.4 Crystallite growth rate in dependence on the gas phase environment

In addition to the influence of metal loadings and BET surface areas, the effects of gas phase environments were investigated on the particle growth at high temperature. Figure 71 compares the changes in sizes for Pt(46 wt.)/Vulcan XC 72R at 160 °C under pure N₂ and synthetic air (20.5 % O₂ in N₂) atmospheres.

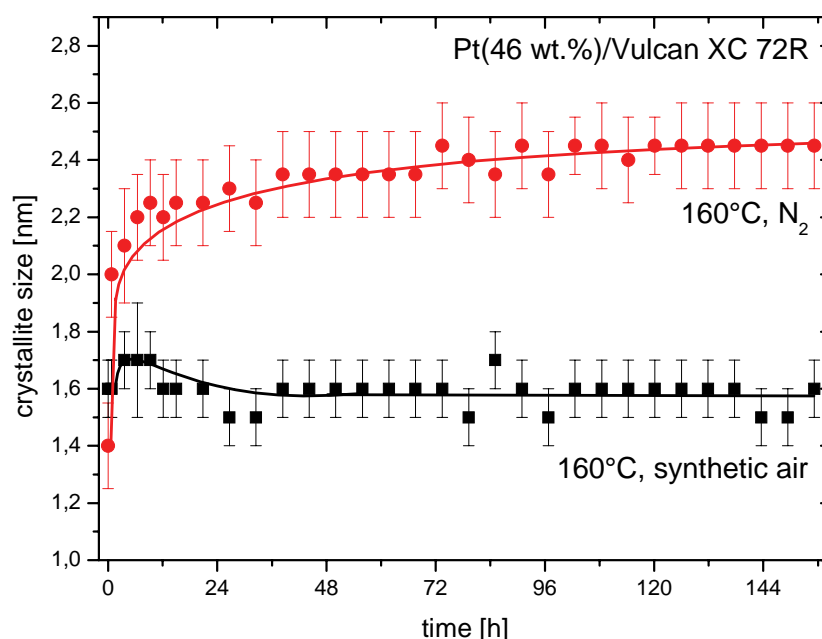


Figure 71 Mean crystallite size of platinum versus thermal treatment time under pure N₂ (red circles) and synthetic air (black squares) atmosphere at 160 °C for Pt(46 wt.)/Vulcan XC 72R. The initial mean crystallite size was determined at 30 °C. Reproduced from reference ¹²⁶ by permission of John Wiley and Sons.

While a typical parabolic curve was observed for the particle growth in a pure N₂ atmosphere at 160 °C (red circles, Figure 71), the HT-XRD measurements in synthetic air showed an unexpected maximum at around 6 hours and subsequently dropping to a constant size plateau after 36 hours. No additional reflections for Pt oxide were observed. The absence of significant growth can be related in two ways. (I) Oxygen may form amorphous Pt oxide layer on the particle surface. This layer may prevent further particle diffusion/migration and coalescence or may disguise particle coalescence. Due to its missing long range order and thickness, the formed amorphous Pt surface oxide is not detectable for the XRD. (II) The reactive gas could oxidize the

carbon surface thereby changing its morphology and slowing down the migration of Pt particles. Insight which mechanism is dominated cannot be achieved by XRD alone. Thus, the use of other techniques, such as transmission electron microscopy¹¹³ (TEM) or small angle X-ray scattering^{112, 127, 128} is required to investigate the morphological and structural change of particles.

In this case, ex situ TEM measurements were performed to verify the results from the in situ HT-XRD study. TEM results show an initial mean particle size of 2.3 ± 0.6 nm. After treatment in N₂ and synthetic air the TEM measurements revealed similar final mean particle sizes for N₂ (2.7 ± 0.6 nm) and synthetic air (2.9 ± 0.6 nm) (see Figure 72).

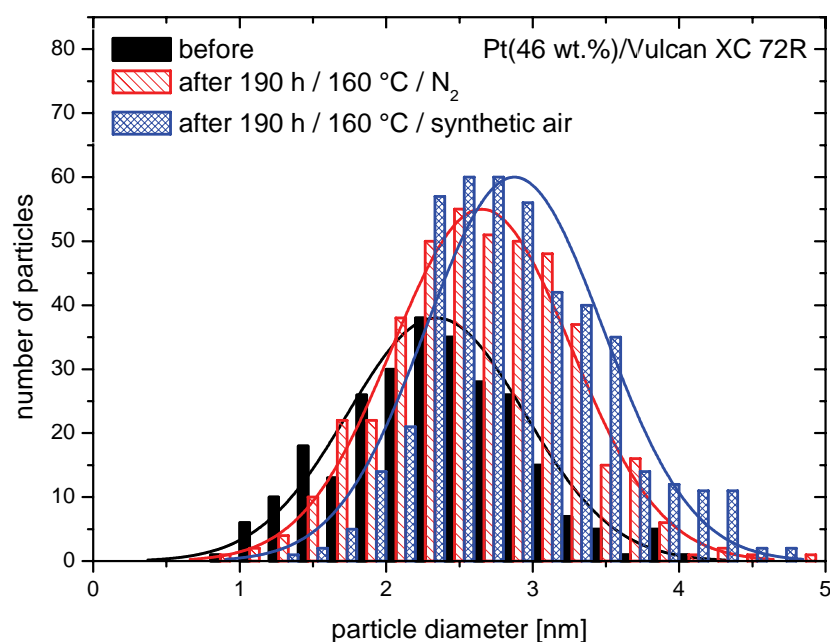


Figure 72 Histograms of particle size distributions for Pt(46 wt.)/HSAC nanoparticle catalyst with x-offset. Black solid bar – initial, red hollow dashed bar – after thermal treatment at 160 °C for 190 hours under N₂ atmosphere and blue hollow crossed bar – after thermal treatment at 160 °C for 190 hours under synthetic air atmosphere. Reproduced from reference¹²⁶ by permission of John Wiley and Sons.

From our TEM micrographs and the size comparison between XRD and TEM we conclude that an amorphous Pt oxide layer formed which due to XRD invisible result in other growth trajectory. The approximated thickness of the oxide layer is in the range of 0.4 – 0.8 nm established by the final XRD measurements at N₂ and synthetic air atmosphere.

5.5 Conclusions

We have performed an in situ parametric study of the structural stability of carbon supported Pt nanoparticles below 3 nm at various Pt loadings, BET surface areas, temperatures, and gas environments using the HT-XRD technique. From our parametric in situ HT-XRD study, a consistent and comprehensive picture is emerging of how factors such as BET surface area value of the support, initial particle size, treatment temperature and metal loadings affect the thermally induced diffusion/coalescence based Pt particle growth. A controlling parameter appears to be the interparticle distance (λ) which is a function of initial particle size, BET surface area, and metal loading. The effect of λ is clear on the thermal stability of supported nanoparticles.

- An increase of the BET surface area leads to improved thermal particle size stability with otherwise identical parameters. The particle growth takes only place for nanoparticles (below 3 nm) supported on lower BET surface area by 160 °C, yet by higher BET surface area the particle size increases only very slightly.
- A reducing of the metal loading leads to improved thermal particle size stability with otherwise identical parameters due to the increasing interparticle distance.
- In contrast to N₂ gas phase environment, synthetic air gas phase leads to a Pt surface oxide layers formation in a thickness to be in the range of 0.4 – 0.8 nm.

Our insight in the parametric dependence of thermally induced particle growth is of general importance and will contribute to develop new strategies for improve long-term catalyst stability and durability with the optimal values in the particle loading, BET surface area, and initial particle size at given reaction conditions for the field of heterogeneous and electrochemical catalysis.

6 Conclusions and Perspectives

In the present thesis, the activity, stability, and degradation mechanisms of platinum and platinum alloy nanoparticle PEM fuel cell electrocatalysts were investigated. The effects of the support material and of the catalytically active component were examined; also, the thermal stability of Pt nanoparticles was established. Together, these results aid in further the understanding of PEM fuel cell electrocatalysts and the design of improved catalysts. The separation and reduction of the complexity of the interaction between support material and active component by changing one material parameter at a time enables to obtain a clearer picture of the structure – activity – stability relationship of supported PEM fuel cell electrocatalysts. This knowledge is helpful to rationally design improved electrocatalysts with predefined designed properties.

Effects of support material. In the first part of the thesis, the effects of the support material were studied. The driving question was how the nature and characteristics of the support material influences the stability and activity of the catalytic metal – support couple. Therefore, platinum nanoparticles were synthesized on several carbon based supports, that varied in their properties like BET surface area, mesoporosity, graphitization or nitrogen doping. The different catalysts were characterized and evaluated for the oxygen reduction reaction. The new materials were compared to benchmark state of the art carbon supported Pt nanoparticles catalysts (Vulcan XC 72R, high surface area carbon). An important overall conclusion was that all materials were suitable as support material for Pt nanoparticles. This is because all materials showed state of the art oxygen reduction reaction activities⁹³. An explicit Pt mass based activity, BET surface area or Pt loading benefit for a support material class was not observed. Due to the similar mean particle size, a particle size effect^{53, 105, 106} could be excluded. Only for Pt/meso-BMP an increased ECSA value was observed, indicating a positive effect of mesoporosity and nitrogen doping on the dispersion of Pt nanoparticles on the support surface. Furthermore, the longterm voltage cycling experiments showed a similar ECSA loss for all tested catalysts. However, only for the Pt/MWNCT catalyst a reduced ECSA loss was

observed. The final mean particle size (3 – 4 nm) is in the same range for all tested catalysts, indicating a similar particle growth behavior during “lifetime” voltage cycling and an independence of the support material. Only the catalyst with the high Pt loading (46 wt.%) shows a slight increased final mean particle size related to the high metal loading. An effect of the BET surface area for the stability in this voltage regime can be excluded. In conclusion, the level of graphitization of the support material is essential to reduce the ECSA loss during voltage cycling. The ECSA loss and final mean particle size of supported Pt nanoparticles is independent of the BET surface area.

Catalytically active component. The middle part of this thesis focused on the catalytically active component of the PEM fuel cell cathode catalysts. Here, several Pt alloy (Pt-Cu, Pt-Co, Pt-Ni) nanoparticle catalysts were synthesized, characterized, evaluated for the oxygen reduction and compared with commercial benchmark pure Pt nanoparticle catalysts. The research was driven by the question, how the catalytically active component affects the stability and ORR activity of PEM fuel cell cathode catalysts. All tested dealloyed Pt alloy nanoparticle catalysts show a significant activity benefit (Pt mass and Pt surface area specific based) compared to pure Pt nanoparticles with similar particle size prior to longterm stability testing. The dealloyed Pt-Cu and Pt-Co nanoparticle catalysts showed a 2 – 3 times higher initial platinum mass based activity, j_{mass} , and a 3 – 4 times higher initial platinum surface area specific based activity, j_{specific} , compared with a commercial pure platinum nanoparticle catalyst. The dealloyed Pt-Ni nanoparticle catalyst exhibited a 7 – 8 fold increase in ORR j_{mass} activity compared to the heat treated Pt catalyst with comparable particle size; and that Pt-Ni showed a 2 – 3 times higher j_{mass} activity than commercial Pt nanoparticles. In terms of their j_{specific} ORR activity, the dealloyed Pt-Ni catalyst showed a 6 – 7 fold and a 5 – 6 fold higher activity compared to pure Pt (HT) and commercial non-annealed pure Pt, respectively.

The voltage cycling RDE experiments were conducted to simulate the longterm behavior of fuel cell electrocatalysts as accelerated degradation tests. Based on the experimental results, an ECSA loss and life cycle degradation model were developed and evaluated. Here, particle coarsening is the dominant

ECSA loss mechanism at early stages of the catalyst life cycle. The nanoparticles (Pt alloy and pure Pt) reach a voltage dependent critical quasi stable mean particle size, D_{critical} , at which the particle size growth rate drops to low values. Once D_{critical} is reached, the ECSA loss is mainly controlled by the carbon corrosion associated with particle detachment. The ECSA loss for Pt alloys during the initial stage is a complex behavior between particle growth and base metal dissolution associated with rearrangement of Pt surface atoms. This is manifested by an initial increase in ECSA followed by a drop in ECSA at a very similar rate like for pure Pt. The concurrent drop in specific activity is likely related to an increase of the Pt shell thickness by redeposition and base metal loss. In the case of corrosive voltage cycling in the “start-up” regime (up to 1.5 V vs. RHE), strong oxidation of carbon and dissolution of Pt become dominant mechanisms for a rapid ECSA loss and accelerated net loss of Pt into the electrolyte. The change in chemical composition of the dealloyed Pt-Cu, Pt-Co and Pt-Ni nanoparticle catalysts is voltage dependent. Under “lifetime” testing (up to 1.0 V vs. RHE) the composition changes only slightly. In contrast, under “start-up” testing the Pt alloys exhibit significant compositional base metal losses.

To confirm this ECSA loss model, a highly active Pt alloy nanoparticle catalyst (Pt-Ni) with a diameter above D_{critical} before of lifetime testing was synthesized and evaluated for oxygen reduction reaction. The experiment showed a drastically reduced ECSA loss and quasi stable mean particle size during voltage cycling. This result verified the above described ECSA loss and life cycle degradation model. Furthermore, the dealloyed Pt-Ni nanoparticle catalyst showed 4 – 5 times and 3 – 4 times higher platinum surface area specific based activities after “lifetime” stability test with 10000 voltage cycles between 0.5 – 1.0 V vs. RHE with a scan rate of 50 mV s^{-1} in deaerated 0.1 M HClO_4 compared to pure Pt (HT) and commercial pure Pt catalysts.

Thermal stability of nanoparticles. The last part of this thesis addressed the thermal stability of carbon supported Pt nanoparticle catalysts at typical PEM fuel cell operating temperature (80 °C and 160 °C). An in situ parametric study of the thermal stability of carbon supported Pt nanoparticles below 3 nm at various Pt loadings, BET surface areas, temperatures, and gas environments using the HT-XRD technique were performed in absence of an electric field and electrolyte. The results from the time-resolved in situ HT-XRD experiments were compared with the ex situ TEM experiments. A simple one parameter model involving the interparticle distance (λ) was developed to estimate the thermal stability of nanoparticle catalysts with different values of BET surface area, metal loading and initial particle size. The model helps to understand, which of the factors, such as BET surface area value of the support, initial particle size, treatment temperature or metal loading significantly controls the thermally induced diffusion/coalescence based Pt particle growth. It was concluded that the particle growth takes only place for nanoparticles below 3 nm supported on lower BET surface area by 160 °C; on higher BET surface area supports, however, the particle size increased only very slightly. An increase of the BET surface area and/or a reducing metal loading led to improved thermal particle size stability with otherwise identical parameters due to the increasing interparticle distance. Based on the experimental results, we assume that during real fuel cell operation, the thermal stability plays a minor role compared to the electrochemical induced degradation.

The present models and experimental results from the effects of the support materials and of the catalytically active components together with the thermal stability of Pt nanoparticles provide guidelines for the design of supported nanoparticle catalysts with improved activity and stability.

Perspectives. Based on the present results, the future perspectives and challenges for further improved PEM fuel cell electrocatalysts are

- The design of corrosion resistant support materials which enable a well dispersion of nanoparticles with high conductivity. For example, structured frameworks with high level of graphitization or non carbon based materials like conductive Ti oxides.
- The improving of the chemical composition stability for Pt alloys during voltage cycling, especially for voltages up to 1.5 V vs. RHE. Pt alloy protecting strategies or intermetallic compounds could be a way.
- The combination of support materials with high level of graphitization, BET surface area and high active Pt alloy nanoparticles with a quasi stable mean particle size before of lifetime voltage testing.
- The transfer/scale-up of the present results established by RDE measurements to single MEA and stack experiments under typical PEM fuel cell conditions (with back pressure, humidity, 80 °C, ...).
- The transfer/scale-up of the synthesis to 50 g batch and more or design a continuous process for example using a rotary tube furnace or fluidized bed reactor.
- The investigation of the present catalyst concepts and/or components for other chemical reactions, for example electrochemical hydrogen peroxide production¹²⁹, carbon dioxide reduction or hydrogenations.

7 Appendix

7.1 Materials and chemicals

Chemical	Supplier	Details
MWCNT	Bayer Material Science	Baytubes C150HP, Lot#E0006AAD08
10 wt.% Pt/Vulcan XC 72R	BASF Fuel Cell Inc.	ID-181
20 wt.% Pt/Vulcan XC 72R	BASF Fuel Cell Inc.	ID-193
28.2 wt.% Pt/HSAC	Tanaka Kikinzoku International	28.2 wt.% Pt, TEC10E30E, Lot#108-0331
45.9 wt.% Pt/HSAC	Tanaka Kikinzoku International	45.9 wt.% Pt, TEC10E50E, Lot#107-2221
46.7 wt.% Pt/Vulcan XC 72R	Tanaka Kikinzoku International	46.7 wt.% Pt, TEC10V50E, Lot#106-2731
$\text{Co}(\text{NO}_3)_2 \cdot 6 \text{H}_2\text{O}$	Alfa Aesar	#010694
$\text{Cu}(\text{NO}_3)_2 \cdot 2.5 \text{H}_2\text{O}$	Sigma-Aldrich	#467855
H_2PtCl_6	Alfa Aesar	20 wt. % platinum, Lot#G19S028
$\text{Ni}(\text{NO}_3)_2 \cdot 6 \text{H}_2\text{O}$	AlfaAesar	#010816
acetone	Sigma-Aldrich	99.5+% A.C.S. Reagenz, #179124
HClO_4	Sigma-Aldrich	70% redistilled, 99.999%, #311421
isopropanol, 2-propanol	Sigma-Aldrich	
Nafion	Sigma-Aldrich	5 wt.% of stock solution, #274704
ultrapure water	Sartorius	18 MOhm at room temperature
O_2	AirLiquide	N48
H_2/Ar	AirLiquide	6 Vol. % H_2 , 94 Vol. % Ar or 4 Vol. % H_2 , 96 Vol. % Ar, quality 5.0
O_2/N_2	AirLiquide	1 Vol.% O_2 (4.5) / 99 Vol.% N_2 (5.0)
synthetic air	AirLiquide	20.5 % O_2 in N_2 , hydrocarbon free, quality 5.0

7.2 Abbreviations and symbols

Symbol	Acceptation
BET	Brunauer-Emmett-Teller
BMP	N-butyl-3-methylpyridine
BMP-dca	N-butyl-3-methylpyridinedicyanamide
CDC	silicon carbide derived carbon
CNT	carbon nanotube
CV	cyclic voltammetry
DoE	U.S. Department of Energy
ECSA	electrochemical active surface area
EDS	energy dispersive X-ray spectroscopy
eq.	equation
fcc	face centered cubic
GC	glassy carbon
HSAC	high surface area carbon
HT	heat treated
HT-XRD	high temperature X-ray diffraction
iR-free	ohmically corrected
LSV	linear sweep voltammetry
M, Me	metal
MEA	membrane electrode assembly
meso	mesoporous
MWCNT	multi walled carbon nanotube
N-	normalized
NHE	normal hydrogen electrode
ORR	oxygen reduction reaction
PDF	reference powder diffraction patterns
PEMFC	proton exchange membrane fuel cell
PSD	position sensitive LynxEye detector
RDE	rotating disk electrode
RHE	reversible hydrogen electrode
TEM	transmission electron microscopy
XRD	X-ray diffraction

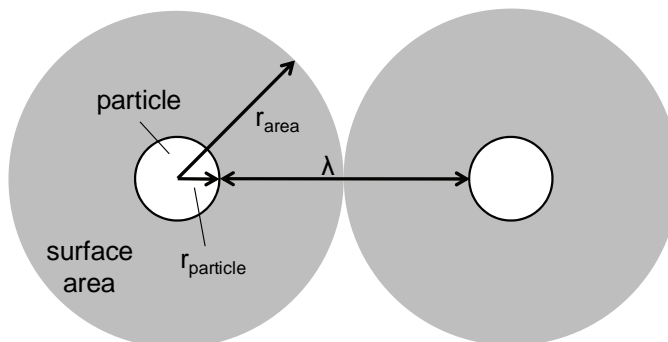
Appendix - Abbreviations and symbols

Symbol	Acceptation	Unit
at.	atomic	%
B	Koutecky – Levich slope	$\text{mA cm}^{-2}_{\text{geo.}} \text{ s}^{1/2}$
BET surface area	Brunauer-Emmett-Teller surface area	$\text{m}^2 \text{ g}^{-1}$
$c(\text{O}_2)$	oxygen solubility	mol l^{-1}
$D(\text{O}_2)$	oxygen diffusivity	$\text{cm}^2 \text{ s}^{-1}$
D_{critical}	quasi stable, critical particle size	nm
E	particle dissolution potential	V
E	voltage	V
$E(0)$	dissolution potential of flat metal surface	V
E_0	standard reduction potential	V
ECSA	platinum electrochemical active surface area	$\text{m}^2 \text{ g}_{\text{Pt}}^{-1}$
F	Faraday constant	C mol^{-1}
G	graphitization extent	%
GOF	goodness-of-fit	--
j	current density	$\text{mA cm}^{-2}_{\text{geo.}}$
$j_{\text{diffusion}}$	diffusion limiting current density	$\text{mA cm}^{-2}_{\text{geo.}}$
j_{kinetic}	kinetic limiting current density	$\text{mA cm}^{-2}_{\text{geo.}}$
j_{mass}	platinum mass based activity	$\text{A mg}^{-1}_{\text{Pt}}$
j_{specific}	platinum surface area specific based activity	$\mu\text{A cm}^{-2}_{\text{Pt}}$
m	mass	g
n	number of transferred electrons	--
ν	kinematic viscosity	$\text{cm}^2 \text{ s}^{-1}$
θ, Θ	angle	°
r	particle radius	nm
R	ideal gas constant	$\text{J mol}^{-1} \text{ K}^{-1}$
R_{exp}	R-expected	--
R_{wp}	R-weighted pattern	--
T	temperature	°C or K
V	volume	L
Vol.	volume	%
ω	rotating rate	U min^{-1}
wt.	weight	%
γ	surface energy	J cm^{-2}
Ω	molar volume	$\text{cm}^3 \text{ mol}^{-1}$

7.3 Model for the calculation of the interparticle distance (λ)

Reproduced from reference ¹²⁶ by permission of John Wiley and Sons.

Assumptions: monodisperse distribution of the particles on the support, particle is an ideal spherical, surrounded from a circular area.



Index: N_x – number of (x), n_x – molar amount of (x) [mol], M_x – molar mass of (x) [g/mol]; N_A – Avogadro constant, d_x – diameter of (x) [nm], r_x – radius of (x) [nm], V_x – volume of (x) [nm³], D_x – dispersion of (x) per area [1/m²], A – area [m²], λ – interparticle distance [nm]

Example: Pt(20 wt. %)/Vulcan XC 72R, BET surface area = 151 [m²/g],
 $d_{\text{particle}} = 1.9$ [nm]

Step 1: number of particles per gram by given wt. %

a) number of Pt atoms: $N_{\text{Pt atom}} = n_{\text{Pt}} * N_A$; $N_{\text{Pt}} = (0.2 \text{ [g]} / 195.09 \text{ [g/mol]}) * 6.02 * 10^{23} \text{ [1/mol]}$; $N_{\text{Pt-atom}} = 6.17 * 10^{20}$

b) volume of Pt atom and volume of particle: $V = 4/3 * \pi * r^3$,
 $V_{\text{Pt atom}} = 0.01 \text{ [nm}^3\text{]}$, $V_{\text{particle}} = 3.59 \text{ [nm}^3\text{]}$

c) number of particles: if $1_{\text{Pt atom}} = V_{\text{Pt atom}}$ then $X_{\text{Pt atom}} = V_{\text{particle}}$;
 $X_{\text{Pt atom}} = 348 \text{ [Pt atoms/particle]}$ and

if $X_{\text{Pt atom}} = 1_{\text{particle}}$ then $N_{\text{Pt atom}} = N_{\text{particle}}$; $N_{\text{particle}} = 1.77 * 10^{18}$

Step 2: area per particle as function of the BET surface area

a) dispersion of the particles at surface area: $D_{\text{particle}} = N_{\text{particle}} / A_{\text{surface area}}$,
 $D_{\text{particle}} = 1.17 * 10^{16} \text{ [particle/m}^2\text{]}$,

b) area which surrounds a particle:

$1/D_{\text{particle}} = A_{\text{surround particle}}$, $A_{\text{surround particle}} = 8.52 * 10^{-17} \text{ [nm}^2\text{/particle]}$

Step 3: interparticle distance (λ)

a) radius of area: $A_{\text{surround particle}} = \pi * r_{\text{area}}^2$, $r_{\text{area}} = 5.2$ [nm],

b) interparticle distance: $\lambda = (2 * r_{\text{area}}) - (2 * r_{\text{particle}})$, $\lambda = 8.5$ [nm]

7.4 Criteria of fit for XRD profiles

Table 15 Criteria of fit using TOPAS. The observed and calculated data at data point are denoted with $Y_{o,m}$ and $Y_{c,m}$ respectively. M is the number of data points and P the number of parameters. w_m the weighting given to data point m which for counting statistics is given by $w_m = 1/\sigma(Y_{o,m})^2$ where $\sigma(Y_{o,m})$ is the error in $Y_{o,m}$ and $I_{o,k}$ and $I_{c,k}$ the “observed” and calculated intensities of the k^{th} reflection.

Criteria of fit	Definition
R – weighted pattern (R_{wp})	$R_{wp} = \sqrt{\frac{\sum w_m (Y_{o,m} - Y_{c,m})^2}{\sum w_m Y_{o,m}^2}}$
R – expected (R_{exp})	$R_{exp} = \sqrt{\frac{\sum M - P}{\sum w_m Y_{o,m}^2}}$
Goodness of fit (GOF)	$GOF = chi^2 = \frac{R_{wp}}{R_{exp}} = \sqrt{\frac{\sum w_m (Y_{o,m} - Y_{c,m})^2}{M - P}}$

8 References

1. Gasteiger, H. A.; Garche, J., Fuel Cells. In *Handbook of Heterogeneous Catalysis*, Wiley-VCH Verlag GmbH & Co. KGaA: 2008.
2. Heinzl, A.; Cappadonia, M.; Stimming, U.; Kordesch, K. V.; de Oliveira, J. C. T., Fuel Cells. In *Ullmann's Encyclopedia of Industrial Chemistry*, Wiley-VCH Verlag GmbH & Co. KGaA: 2000.
3. Krischer, K.; Savinova, E. R., Fundamentals of Electrocatalysis. In *Handbook of Heterogeneous Catalysis*, Wiley-VCH Verlag GmbH & Co. KGaA: 2008.
4. Norskov, J. K.; Rossmeisl, J.; Logadottir, A.; Lindqvist, L.; Kitchin, J. R.; Bligaard, T.; Jónsson, H., Origin of the Overpotential for Oxygen Reduction at a Fuel-Cell Cathode. *The Journal of Physical Chemistry B* **2004**, 108, (46), 17886-17892.
5. Borup, R.; Meyers, J.; Pivovar, B.; Kim, Y. S.; Mukundan, R.; Garland, N.; Myers, D.; Wilson, M.; Garzon, F.; Wood, D.; Zelenay, P.; More, K.; Stroh, K.; Zawodzinski, T.; Boncella, J.; McGrath, J. E.; Inaba, M.; Miyatake, K.; Hori, M.; Ota, K.; Ogumi, Z.; Miyata, S.; Nishikata, A.; Siroma, Z.; Uchimoto, Y.; Yasuda, K.; Kimijima, K.-i.; Iwashita, N., Scientific Aspects of Polymer Electrolyte Fuel Cell Durability and Degradation. *Chemical Reviews* **2007**, 107, (10), 3904-3951.
6. Department of Energy, Table 3.4.12 Technical Targets: Electrocatalysts for Transportation Applications. *Department of Energy - Multi Year Research and Development Plan* **2007**.
7. Zhang, J.; Mo, Y.; Vukmirovic, M. B.; Klie, R.; Sasaki, K.; Adzic, R. R., Platinum Monolayer Electrocatalysts for O₂ Reduction: Pt Monolayer on Pd(111) and on Carbon-Supported Pd Nanoparticles. *The Journal of Physical Chemistry B* **2004**, 108, (30), 10955-10964.
8. Sasaki, K.; Naohara, H.; Cai, Y.; Choi, Y. M.; Liu, P.; Vukmirovic, M. B.; Wang, J. X.; Adzic, R. R., Core-Protected Platinum Monolayer Shell High-Stability Electrocatalysts for Fuel-Cell Cathodes. *Angewandte Chemie International Edition* **2010**, 49, (46), 8602-8607.
9. Stamenkovic, V. R.; Mun, B. S.; Mayrhofer, K. J. J.; Ross, P. N.; Markovic, N. M., Effect of Surface Composition on Electronic Structure, Stability, and Electrocatalytic Properties of Pt-Transition Metal Alloys: Pt-Skin versus Pt-Skeleton Surfaces. *Journal of the American Chemical Society* **2006**, 128, (27), 8813-8819.
10. Stamenkovic, V.; Schmidt, T. J.; Ross, P. N.; Markovic, N. M., Surface Composition Effects in Electrocatalysis: Kinetics of Oxygen Reduction on Well-Defined Pt₃Ni and Pt₃Co Alloy Surfaces. *The Journal of Physical Chemistry B* **2002**, 106, (46), 11970-11979.
11. Toda, T.; Igarashi, H.; Uchida, H.; Watanabe, M., Enhancement of the Electroreduction of Oxygen on Pt Alloys with Fe, Ni, and Co. *Journal of The Electrochemical Society* **1999**, 146, (10), 3750-3756.
12. Gasteiger, H. A.; Markovic, N. M., CHEMISTRY: Just a Dream--or Future Reality? *Science* **2009**, 324, (5923), 48-49.
13. Strasser, P., Dealloyed Core Shell Fuel Cell Electrocatalysts. *Reviews in Chemical Engineering* **2009**, 25, (4), 255.

References

14. Strasser, P.; Koh, S.; Anniyev, T.; Greeley, J.; More, K.; Yu, C.; Liu, Z.; Kaya, S.; Nordlund, D.; Ogasawara, H.; Toney, M. F.; Nilsson, A., Lattice-strain control of the activity in dealloyed core-shell fuel cell catalysts. *Nature Chemistry* **2010**, 2, (6), 454-460.
15. Oezaslan, M.; Strasser, P., Activity of dealloyed PtCo₃ and PtCu₃ nanoparticle electrocatalyst for oxygen reduction reaction in polymer electrolyte membrane fuel cell. *Journal of Power Sources* **2011**, 196, (12), 5240-5249.
16. Oezaslan, M.; Hasché, F.; Strasser, P., Structure-Activity Relationship of Dealloyed PtCo₃ and PtCu₃ Nanoparticle Electrocatalyst for Oxygen Reduction Reaction in PEMFC. *ECS Transactions* **2010**, 33, (1), 333-341.
17. Wang, C.; van der Vliet, D.; More, K. L.; Zaluzec, N. J.; Peng, S.; Sun, S.; Daimon, H.; Wang, G.; Greeley, J.; Pearson, J.; Paulikas, A. P.; Karapetrov, G.; Strmcnik, D.; Markovic, N. M.; Stamenkovic, V. R., Multimetallic Au/FePt₃ Nanoparticles as Highly Durable Electrocatalyst. *Nano Letters* **2010**, 11, (3), 919-926.
18. Srivastava, R.; Mani, P.; Hahn, N.; Strasser, P., Efficient Oxygen Reduction Fuel Cell Electrocatalysis on Voltammetrically Dealloyed Pt-Cu-Co Nanoparticles. *Angewandte Chemie International Edition* **2007**, 46, (47), 8988-8991.
19. Strasser, P.; Koh, S.; Greeley, J., Voltammetric surface dealloying of Pt bimetallic nanoparticles: an experimental and DFT computational analysis. *Physical Chemistry Chemical Physics* **2008**, 10, (25), 3670-3683.
20. Paulus, U. A.; Wokaun, A.; Scherer, G. G.; Schmidt, T. J.; Stamenkovic, V.; Markovic, N. M.; Ross, P. N., Oxygen reduction on high surface area Pt-based alloy catalysts in comparison to well defined smooth bulk alloy electrodes. *Electrochimica Acta* **2002**, 47, (22-23), 3787-3798.
21. Paulus, U. A.; Wokaun, A.; Scherer, G. G.; Schmidt, T. J.; Stamenkovic, V.; Radmilovic, V.; Markovic, N. M.; Ross, P. N., Oxygen Reduction on Carbon-Supported Pt-Ni and Pt-Co Alloy Catalysts. *The Journal of Physical Chemistry B* **2002**, 106, (16), 4181-4191.
22. Mukerjee, S.; Srinivasan, S., Enhanced electrocatalysis of oxygen reduction on platinum alloys in proton exchange membrane fuel cells. *Journal of Electroanalytical Chemistry* **1993**, 357, (1-2), 201-224.
23. Yang, H.; Vogel, W.; Lamy, C.; Alonso-Vante, N., Structure and Electrocatalytic Activity of Carbon-Supported Pt-Ni Alloy Nanoparticles Toward the Oxygen Reduction Reaction. *The Journal of Physical Chemistry B* **2004**, 108, (30), 11024-11034.
24. Wakabayashi, N.; Takeichi, M.; Uchida, H.; Watanabe, M., Temperature Dependence of Oxygen Reduction Activity at Pt-Fe, Pt-Co, and Pt-Ni Alloy Electrodes. *The Journal of Physical Chemistry B* **2005**, 109, (12), 5836-5841.
25. Antolini, E.; Salgado, J. R. C.; Gonzalez, E. R., The stability of Pt-M (M = first row transition metal) alloy catalysts and its effect on the activity in low temperature fuel cells: A literature review and tests on a Pt-Co catalyst. *Journal of Power Sources* **2006**, 160, (2), 957-968.

References

26. Zignani, S. C.; Antolini, E.; Gonzalez, E. R., Stability of Pt-Ni/C (1:1) and Pt/C electrocatalysts as cathode materials for polymer electrolyte fuel cells: Effect of ageing tests. *Journal of Power Sources* **2009**, 191, (2), 344-350.
27. Oezaslan, M.; Hasché, F.; Strasser, P., In Situ Observation of Bimetallic Alloy Nanoparticle Formation and Growth Using High-Temperature XRD. *Chemistry of Materials* **2011**, 23, (8), 2159-2165.
28. Stamenkovic, V. R.; Fowler, B.; Mun, B. S.; Wang, G.; Ross, P. N.; Lucas, C. A.; Markovic, N. M., Improved Oxygen Reduction Activity on Pt₃Ni(111) via Increased Surface Site Availability. *Science* **2007**, 315, (5811), 493-497.
29. Wagner, F. T.; Lakshmanan, B.; Mathias, M. F., Electrochemistry and the Future of the Automobile. *The Journal of Physical Chemistry Letters* **2010**, 1, (14), 2204-2219.
30. Adzic, R.; Zhang, J.; Sasaki, K.; Vukmirovic, M.; Shao, M.; Wang, J.; Nilekar, A.; Mavrikakis, M.; Valerio, J.; Uribe, F., Platinum Monolayer Fuel Cell Electrocatalysts. *Topics in Catalysis* **2007**, 46, (3), 249-262.
31. Nilekar, A.; Xu, Y.; Zhang, J.; Vukmirovic, M.; Sasaki, K.; Adzic, R.; Mavrikakis, M., Bimetallic and Ternary Alloys for Improved Oxygen Reduction Catalysis. *Topics in Catalysis* **2007**, 46, (3), 276-284.
32. Mani, P.; Srivastava, R.; Strasser, P., Dealloyed binary PtM₃ (M = Cu, Co, Ni) and ternary PtNi₃M (M = Cu, Co, Fe, Cr) electrocatalysts for the oxygen reduction reaction: Performance in polymer electrolyte membrane fuel cells. *Journal of Power Sources* **2011**, 196, (2), 666-673.
33. Yang, H., Platinum-Based Electrocatalysts with Core-Shell Nanostructures. *Angewandte Chemie International Edition* **2011**, 50, (12), 2674-2676.
34. Koh, S.; Yu, C.; Mani, P.; Srivastava, R.; Strasser, P., Activity of ordered and disordered Pt-Co alloy phases for the electroreduction of oxygen in catalysts with multiple coexisting phases. *Journal of Power Sources* **2007**, 172, (1), 50-56.
35. Neyerlin, K. C.; Srivastava, R.; Yu, C.; Strasser, P., Electrochemical activity and stability of dealloyed Pt-Cu and Pt-Cu-Co electrocatalysts for the oxygen reduction reaction (ORR). *Journal of Power Sources* **2009**, 186, (2), 261-267.
36. Hasché, F.; Oezaslan, M.; Strasser, P., Activity, Stability, and Degradation Mechanisms of Dealloyed PtCu₃ and PtCo₃ Nanoparticle Fuel Cell Catalysts. *ChemCatChem* **2011**, 3, (11), 1805-1813.
37. Debe, M. K.; Steinbach, A. J.; Vernstrom, G. D.; Hendricks, S. M.; Kurkowsky, M. J.; Atanasoski, R. T.; Kadera, P.; Stevens, D. A.; Sanderson, R. J.; Marvel, E.; Dahn, J. R., Extraordinary Oxygen Reduction Activity of Pt₃Ni₇. *Journal of The Electrochemical Society* **2011**, 158, (8), B910-B918.
38. Stevens, D. A.; Mehrotra, R.; Sanderson, R. J.; Vernstrom, G. D.; Atanasoski, R. T.; Debe, M. K.; Dahn, J. R., Dissolution of Ni from High Ni Content Pt_{1-x}Ni_x Alloys. *Journal of The Electrochemical Society* **2011**, 158, (8), B905-B909.

39. Wang, C.; Chi, M.; Wang, G.; van der Vliet, D.; Li, D.; More, K.; Wang, H.-H.; Schlueter, J. A.; Markovic, N. M.; Stamenkovic, V. R., Correlation Between Surface Chemistry and Electrocatalytic Properties of Monodisperse Pt_xNi_{1-x} Nanoparticles. *Advanced Functional Materials* **2011**, 21, (1), 147-152.
40. Loukrakpam, R.; Luo, J.; He, T.; Chen, Y.; Xu, Z.; Njoki, P. N.; Wanjala, B. N.; Fang, B.; Mott, D.; Yin, J.; Klar, J.; Powell, B.; Zhong, C.-J., Nanoengineered PtCo and PtNi Catalysts for Oxygen Reduction Reaction: An Assessment of the Structural and Electrocatalytic Properties. *The Journal of Physical Chemistry C* **2011**, 115, (5), 1682-1694.
41. Kim, J.; Lee, S. W.; Carlton, C.; Shao-Horn, Y., Oxygen Reduction Activity of Pt_xNi_{1-x} Alloy Nanoparticles on Multiwall Carbon Nanotubes. *Electrochemical and Solid-State Letters* **2011**, 14, (10), B110-B113.
42. Stamenkovic, V. R.; Mun, B. S.; Arenz, M.; Mayrhofer, K. J. J.; Lucas, C. A.; Wang, G.; Ross, P. N.; Markovic, N. M., Trends in electrocatalysis on extended and nanoscale Pt-bimetallic alloy surfaces. *Nat Mater* **2007**, 6, (3), 241-247.
43. Matanovic, I.; Garzon, F. H.; Henson, N. J., Theoretical Study of Electrochemical Processes on Pt-Ni Alloys. *The Journal of Physical Chemistry C* **2011**, 115, (21), 10640-10650.
44. Stamenkovic, V.; Mun, B. S.; Mayrhofer, K. J. J.; Ross, P. N.; Markovic, N. M.; Rossmeisl, J.; Greeley, J.; Nørskov, J. K., Changing the Activity of Electrocatalysts for Oxygen Reduction by Tuning the Surface Electronic Structure. *Angewandte Chemie International Edition* **2006**, 45, (18), 2897-2901.
45. Calle-Vallejo, F.; Martinez, J. I.; Rossmeisl, J., Density functional studies of functionalized graphitic materials with late transition metals for oxygen reduction reactions. *Physical Chemistry Chemical Physics* **2011**, 13, 15639-15643.
46. Greeley, J.; Stephens, I. E. L.; Bondarenko, A. S.; Johansson, T. P.; Hansen, H. A.; Jaramillo, T. F.; Rossmeisl, J.; Chorkendorff, I.; Nørskov, J. K., Alloys of platinum and early transition metals as oxygen reduction electrocatalysts. *Nat Chem* **2009**, 1, (7), 552-556.
47. Ferreira, P. J.; la O, G. J.; Shao-Horn, Y.; Morgan, D.; Makharia, R.; Kocha, S.; Gasteiger, H. A., Instability of Pt/C Electrocatalysts in Proton Exchange Membrane Fuel Cells. *Journal of The Electrochemical Society* **2005**, 152, (11), A2256-A2271.
48. Shao-Horn, Y.; Sheng, W.; Chen, S.; Ferreira, P.; Holby, E.; Morgan, D., Instability of Supported Platinum Nanoparticles in Low-Temperature Fuel Cells. *Topics in Catalysis* **2007**, 46, (3), 285-305.
49. Holby, E. F.; Sheng, W.; Shao-Horn, Y.; Morgan, D., Pt nanoparticle stability in PEM fuel cells: influence of particle size distribution and crossover hydrogen. *Energy & Environmental Science* **2009**, 2, (8), 865-871.
50. Thiel, P. A.; Shen, M.; Liu, D.-J.; Evans, J. W., Coarsening of Two-Dimensional Nanoclusters on Metal Surfaces. *The Journal of Physical Chemistry C* **2009**, 113, (13), 5047-5067.

References

51. Schmittinger, W.; Vahidi, A., A review of the main parameters influencing long-term performance and durability of PEM fuel cells. *Journal of Power Sources* **2008**, 180, (1), 1-14.
52. Hasché, F.; Oezaslan, M.; Strasser, P., Activity, stability and degradation of multi walled carbon nanotube (MWCNT) supported Pt fuel cell electrocatalysts. *Physical Chemistry Chemical Physics* **2010**, 12, (46), 15251-15258.
53. Mukerjee, S., Particle size and structural effects in platinum electrocatalysis. *Journal of Applied Electrochemistry* **1990**, 20, (4), 537-548.
54. Tang, L.; Han, B.; Persson, K.; Friesen, C.; He, T.; Sieradzki, K.; Ceder, G., Electrochemical Stability of Nanometer-Scale Pt Particles in Acidic Environments. *Journal of the American Chemical Society* **2009**, 132, (2), 596-600.
55. Rinaldo, S. G.; Stumper, J. r.; Eikerling, M., Physical Theory of Platinum Nanoparticle Dissolution in Polymer Electrolyte Fuel Cells. *The Journal of Physical Chemistry C* **2010**, 114, (13), 5773-5785.
56. Yousfi-Steiner, N.; Moçotéguy, P.; Candusso, D.; Hissel, D., A review on polymer electrolyte membrane fuel cell catalyst degradation and starvation issues: Causes, consequences and diagnostic for mitigation. *Journal of Power Sources* **2009**, 194, (1), 130-145.
57. Lin, J. F.; Adame, A.; Kannan, A. M., Development of Durable Platinum Nanocatalyst on Carbon Nanotubes for Proton Exchange Membrane Fuel Cells. *Journal of The Electrochemical Society* **2010**, 157, (6), B846-B851.
58. Zhang, S.; Yuan, X.-Z.; Hin, J. N. C.; Wang, H.; Friedrich, K. A.; Schulze, M., A review of platinum-based catalyst layer degradation in proton exchange membrane fuel cells. *Journal of Power Sources* **2009**, 194, (2), 588-600.
59. Wang, J.; Yin, G.; Shao, Y.; Wang, Z.; Gao, Y., Investigation of Further Improvement of Platinum Catalyst Durability with Highly Graphitized Carbon Nanotubes Support. *The Journal of Physical Chemistry C* **2008**, 112, (15), 5784-5789.
60. Mark F. Mathais, R. M., Hubert A. Gasteiger, Jason J. Conley, Timothy J. Fuller, Craig J. Gittleman, Shyam S. Kocha, Daniel P. Miller, Corky K. Mittelsteadt, Tao Xie, Susan G. Yan, Paul T. Yu, Two Fuel Cell Cars in Every Garage? *The Electrochemical Society INTERFACE Fall* **2005**, 14, (3), 24-35.
61. Gallagher, K. G.; Fuller, T. F., Kinetic model of the electrochemical oxidation of graphitic carbon in acidic environments. *Physical Chemistry Chemical Physics* **2009**, 11, (48), 11557-11567.
62. Borchardt, L.; Hasché, F.; Lohe, M. R.; Oschatz, M.; Schmidt, F.; Kockrick, E.; Ziegler, C.; Lescouet, T.; Bachmatiuk, A.; Büchner, B.; Farrusseng, D.; Strasser, P.; Kaskel, S., Transition metal loaded silicon carbide-derived carbons with enhanced catalytic properties. *Carbon* **2012**, 50, (5), 1861-1870.
63. Fang, B.; Kim, J. H.; Kim, M.; Kim, M.; Yu, J.-S., Hierarchical nanostructured hollow spherical carbon with mesoporous shell as a unique cathode catalyst support in proton exchange membrane fuel cell. *Physical Chemistry Chemical Physics* **2009**, 11, (9), 1380-1387.

References

64. Hasché, F.; Fellingner, T.-P.; Oezaslan, M.; Paraknowitsch, J. P.; Antonietti, M.; Strasser, P., Mesoporous Nitrogen Doped Carbon Supported Platinum PEM Fuel Cell Electrocatalyst Made From Ionic Liquids. *ChemCatChem* **2012**, 4, (4), 479-483.
65. Zhou, Y.; Neyerlin, K.; Olson, T. S.; Pylypenko, S.; Bult, J.; Dinh, H. N.; Gennett, T.; Shao, Z.; O'Hayre, R., Enhancement of Pt and Pt-alloy fuel cell catalyst activity and durability via nitrogen-modified carbon supports. *Energy & Environmental Science* **2010**, 3, (10), 1437-1446.
66. Yin, S.; Mu, S.; Pan, M.; Fu, Z., A highly stable TiB₂-supported Pt catalyst for polymer electrolyte membrane fuel cells. *Journal of Power Sources* **2011**, 196, (19), 7931-7936.
67. Jiang, Z.-Z.; Wang, Z.-B.; Chu, Y.-Y.; Gu, D.-M.; Yin, G.-P., Carbon riveted microcapsule Pt/MWCNTs-TiO₂ catalyst prepared by in situ carbonized glucose with ultrahigh stability for proton exchange membrane fuel cell. *Energy & Environmental Science* **2011**, 4, (7), 2558-2566.
68. Jiang, Z.-Z.; Wang, Z.-B.; Chu, Y.-Y.; Gu, D.-M.; Yin, G.-P., Ultrahigh stable carbon riveted Pt/TiO₂-C catalyst prepared by in situ carbonized glucose for proton exchange membrane fuel cell. *Energy & Environmental Science* **2011**, 4, (3), 728-735.
69. Datta, K. K. R.; Balasubramanian, V. V.; Ariga, K.; Mori, T.; Vinu, A., Highly Crystalline and Conductive Nitrogen-Doped Mesoporous Carbon with Graphitic Walls and Its Electrochemical Performance. *Chemistry – A European Journal* **2011**, 17, (12), 3390-3397.
70. Leonard, N. D.; Nallathambi, V.; Barton, S. C., Carbon Supports for Non-Precious Metal Proton Exchange Membrane Fuel Cells. *ECS Transactions* **2011**, 41, (1), 1175-1181.
71. Nallathambi, V.; Leonard, N.; Kothandaraman, R.; Barton, S. C., Nitrogen Precursor Effects in Iron-Nitrogen-Carbon Oxygen Reduction Catalysts. *Electrochemical and Solid-State Letters* **2011**, 14, (6), B55-B58.
72. Jaouen, F.; Herranz, J.; Lefevre, M.; Dodelet, J.-P.; Kramm, U. I.; Herrmann, I.; Bogdanoff, P.; Maruyama, J.; Nagaoka, T.; Garsuch, A.; Dahn, J. R.; Olson, T.; Pylypenko, S.; Atanassov, P.; Ustinov, E. A., Cross-Laboratory Experimental Study of Non-Noble-Metal Electrocatalysts for the Oxygen Reduction Reaction. *ACS Applied Materials & Interfaces* **2009**, 1, (8), 1623-1639.
73. Lefevre, M.; Proietti, E.; Jaouen, F.; Dodelet, J.-P., Iron-Based Catalysts with Improved Oxygen Reduction Activity in Polymer Electrolyte Fuel Cells. *Science* **2009**, 324, (5923), 71-74.
74. Bashyam, R.; Zelenay, P., A class of non-precious metal composite catalysts for fuel cells. *Nature* **2006**, 443, (7107), 63-66.
75. Wu, G.; More, K. L.; Johnston, C. M.; Zelenay, P., High-Performance Electrocatalysts for Oxygen Reduction Derived from Polyaniline, Iron, and Cobalt. *Science* **2011**, 332, (6028), 443-447.
76. Yuan, X.; Zeng, X.; Zhang, H.-J.; Ma, Z.-F.; Wang, C.-Y., Improved Performance of Proton Exchange Membrane Fuel Cells with p-Toluenesulfonic Acid-Doped Co-PPy/C as Cathode Electrocatalyst. *Journal of the American Chemical Society* **2010**, 132, (6), 1754-1755.

References

77. Yang, W.; Fellingner, T.-P.; Antonietti, M., Efficient Metal-Free Oxygen Reduction in Alkaline Medium on High-Surface-Area Mesoporous Nitrogen-Doped Carbons Made from Ionic Liquids and Nucleobases. *Journal of the American Chemical Society* **2011**, 133, (2), 206-209.
78. Darling, R. M.; Meyers, J. P., Mathematical Model of Platinum Movement in PEM Fuel Cells. *Journal of The Electrochemical Society* **2005**, 152, (1), A242-A247.
79. Meyers, J. P.; Darling, R. M., Model of Carbon Corrosion in PEM Fuel Cells. *Journal of The Electrochemical Society* **2006**, 153, (8), A1432-A1442.
80. Ball, S. C.; Hudson, S. L.; Thompsett, D.; Theobald, B., An investigation into factors affecting the stability of carbons and carbon supported platinum and platinum/cobalt alloy catalysts during 1.2 V potentiostatic hold regimes at a range of temperatures. *Journal of Power Sources* **2007**, 171, (1), 18-25.
81. Borup, R. L.; Davey, J. R.; Garzon, F. H.; Wood, D. L.; Inbody, M. A., PEM fuel cell electrocatalyst durability measurements. *Journal of Power Sources* **2006**, 163, (1), 76-81.
82. Dumesic, J. A.; Huber, G. W.; Boudart, M., Principles of Heterogeneous Catalysis. In *Handbook of Heterogeneous Catalysis*, Wiley-VCH Verlag GmbH & Co. KGaA: 2008.
83. Schmidt, T. J.; Baurmeister, J., Properties of high-temperature PEFC Celtec®-P 1000 MEAs in start/stop operation mode. *Journal of Power Sources* **2008**, 176, (2), 428-434.
84. Laue, M. v., *Z. Kristallogr.* **1926**, 64, 115.
85. Schmidt, T. J.; Gasteiger, H. A.; Stab, G. D.; Urban, P. M.; Kolb, D. M.; Behm, R. J., Characterization of High-Surface-Area Electrocatalysts Using a Rotating Disk Electrode Configuration. *Journal of The Electrochemical Society* **1998**, 145, (7), 2354-2358.
86. Paulus, U. A.; Schmidt, T. J.; Gasteiger, H. A.; Behm, R. J., Oxygen reduction on a high-surface area Pt/Vulcan carbon catalyst: a thin-film rotating ring-disk electrode study. *Journal of Electroanalytical Chemistry* **2001**, 495, (2), 134-145.
87. ICDD, Powder Diffraction File (PDF) 2 Data CD, <http://www.icdd.com>. *International Center for Diffraction Data* **2002**.
88. Yu, P. T.; Gu, W.; Makharia, R.; Wagner, F. T.; Gasteiger, H. A., The Impact of Carbon Stability on PEM Fuel Cell Startup and Shutdown Voltage Degradation. *ECS Transactions* **2006**, 3, (1), 797-809.
89. Srivastava, R.; Strasser, P., Oxygen Evolution Co-Catalysts at Fuel Cell Cathodes for Degradation Mitigation during Simulated Start-up Shut-down Cycles. *ECS Transactions* **2009**, 25, (1), 565-571.
90. Reiser, C. A.; Bregoli, L.; Patterson, T. W.; Yi, J. S.; Yang, J. D.; Perry, M. L.; Jarvi, T. D., A Reverse-Current Decay Mechanism for Fuel Cells. *Electrochemical and Solid-State Letters* **2005**, 8, (6), A273-A276.
91. Darling, R. M.; Meyers, J. P., Kinetic Model of Platinum Dissolution in PEMFCs. *Journal of The Electrochemical Society* **2003**, 150, (11), A1523-A1527.

References

92. Neyerlin, K. C.; Srivastava, R.; Strasser, P., Electrochemical Stability of PtCu and PtCuCo Core-Shell Oxygen Reduction Reaction Electrocatalysts in Liquid Electrolyte. *ECS Transactions* **2008**, 16, (2), 509-514.
93. Gasteiger, H. A.; Kocha, S. S.; Sompalli, B.; Wagner, F. T., Activity benchmarks and requirements for Pt, Pt-alloy, and non-Pt oxygen reduction catalysts for PEMFCs. *Applied Catalysis B: Environmental* **2005**, 56, (1-2), 9-35.
94. Yu, C.; Yang, R.; Toney, M.; Holby, E.; Morgan, D.; Strasser, P., **2010**, in preparation.
95. Yu, C.; Yang, R.; Toney, M.; Strasser, P., **2010**, in preparation.
96. Paraknowitsch, J. P.; Zhang, J.; Su, D.; Thomas, A.; Antonietti, M., Ionic Liquids as Precursors for Nitrogen-Doped Graphitic Carbon. *Advanced Materials* **2010**, 22, (1), 87-92.
97. Paraknowitsch, J. P.; Thomas, A.; Antonietti, M., A detailed view on the polycondensation of ionic liquid monomers towards nitrogen doped carbon materials. *Journal of Materials Chemistry* **2010**, 20, (32), 6746-6758.
98. Hasché, F.; Oezaslan, M.; Strasser, P., Activity and Structure of Dealloyed PtNi₃ Nanoparticle Electrocatalyst for Oxygen Reduction Reaction in PEMFC. *ECS Transactions* **2011**, 41, (1), 1079-1088.
99. Oezaslan, M.; Hasché, F.; Strasser, P., Oxygen Electroreduction on Pt_xCo_{1-x} and Pt_xCu_{1-x} Alloy Nanoparticles for Basic and Acidic PEM Fuel Cell. *ECS Transactions* **2011**, 41, (1), 1659-1668.
100. Hamann, C. H.; Hamnett, A.; Vielstich, W., Electrochemistry. *Electrochemistry, Wiley-VCH* **2007**.
101. Bard, A. J.; Stratmann, M., Encyclopedia of Electrochemistry. *Encyclopedia of Electrochemistry, Wiley-VCH* **2007**.
102. Markovic, N. M.; Gasteiger, H. A.; Grgur, B. N.; Ross, P. N., Oxygen reduction reaction on Pt(111): effects of bromide. *Journal of Electroanalytical Chemistry* **1999**, 467, (1-2), 157-163.
103. Mayrhofer, K. J. J.; Strmcnik, D.; Blizanac, B. B.; Stamenkovic, V.; Arenz, M.; Markovic, N. M., Measurement of oxygen reduction activities via the rotating disc electrode method: From Pt model surfaces to carbon-supported high surface area catalysts. *Electrochimica Acta* **2008**, 53, (7), 3181-3188.
104. Hasché, F.; Oezaslan, M.; Strasser, P., Activity, Structure and Degradation of Dealloyed PtNi₃ Nanoparticle Electrocatalyst for the Oxygen Reduction Reaction in PEMFC. *Journal of The Electrochemical Society* **2012**, 159, (1), B25-B34.
105. Kinoshita, K., Particle Size Effects for Oxygen Reduction on Highly Dispersed Platinum in Acid Electrolytes. *Journal of The Electrochemical Society* **1990**, 137, (3), 845-848.
106. Nesselberger, M.; Ashton, S.; Meier, J. C.; Katsounaros, I.; Mayrhofer, K. J. J.; Arenz, M., The Particle Size Effect on the Oxygen Reduction Reaction Activity of Pt Catalysts: Influence of Electrolyte and Relation to Single Crystal Models. *Journal of the American Chemical Society* **2011**, 133, (43), 17428-17433.
107. Mayrhofer, K. J. J.; Meier, J. C.; Ashton, S. J.; Wiberg, G. K. H.; Kraus, F.; Hanzlik, M.; Arenz, M., Fuel cell catalyst degradation on the nanoscale. *Electrochemistry Communications* **2008**, 10, (8), 1144-1147.

108. Hartl, K.; Hanzlik, M.; Arenz, M., IL-TEM investigations on the degradation mechanism of Pt/C electrocatalysts with different carbon supports. *Energy & Environmental Science* **2011**, 4, (1), 234-238.
109. Colón-Mercado, H. R.; Popov, B. N., Stability of platinum based alloy cathode catalysts in PEM fuel cells. *Journal of Power Sources* **2006**, 155, (2), 253-263.
110. Chen, S.; Gasteiger, H. A.; Hayakawa, K.; Tada, T.; Shao-Horn, Y., Platinum-Alloy Cathode Catalyst Degradation in Proton Exchange Membrane Fuel Cells: Nanometer-Scale Compositional and Morphological Changes. *Journal of The Electrochemical Society* **2010**, 157, (1), A82-A97.
111. Mayrhofer, K. J. J.; Blizanac, B. B.; Arenz, M.; Stamenkovic, V. R.; Ross, P. N.; Markovic, N. M., The Impact of Geometric and Surface Electronic Properties of Pt-Catalysts on the Particle Size Effect in Electrocatalysis. *The Journal of Physical Chemistry B* **2005**, 109, (30), 14433-14440.
112. Ingham, B.; Lim, T. H.; Dotzler, C. J.; Henning, A.; Toney, M. F.; Tilley, R. D., How Nanoparticles Coalesce: An in Situ Study of Au Nanoparticle Aggregation and Grain Growth. *Chemistry of Materials* **2011**, 23, (14), 3312-3317.
113. Asoro, M. A.; Kovar, D.; Shao-Horn, Y.; Allard, L. F.; Ferreira, P. J., Coalescence and sintering of Pt nanoparticles: in situ observation by aberration-corrected HAADF STEM. *Nanotechnology* **2010**, 21, (2), 025701.
114. Oezaslan, M.; Heggen, M.; Strasser, P., Size-Dependent Morphology of Dealloyed Bimetallic Catalysts: Linking the Nano to the Macro Scale. *Journal of the American Chemical Society* **2012**, 134, (1), 514-524.
115. Li, L.; Zhan, Y.; Zheng, Q.; Zheng, Y.; Chen, C.; She, Y.; Lin, X.; Wei, K., Water-Gas Shift Reaction over CuO/CeO₂ Catalysts: Effect of the Thermal Stability and Oxygen Vacancies of CeO₂ Supports Previously Prepared by Different Methods. *Catalysis Letters* **2009**, 130, (3), 532-540.
116. Kaneeda, M.; Iizuka, H.; Hiratsuka, T.; Shinotsuka, N.; Arai, M., Improvement of thermal stability of NO oxidation Pt/Al₂O₃ catalyst by addition of Pd. *Applied Catalysis B: Environmental* **2009**, 90, (3-4), 564-569.
117. Lu, A.-H.; Nitz, J.-J.; Comotti, M.; Weidenthaler, C.; Schlichte, K.; Lehmann, C. W.; Terasaki, O.; Schüth, F., Spatially and Size Selective Synthesis of Fe-Based Nanoparticles on Ordered Mesoporous Supports as Highly Active and Stable Catalysts for Ammonia Decomposition. *Journal of the American Chemical Society* **2010**, 132, (40), 14152-14162.
118. Cho, A.; Koh, J. H.; Lee, S. I.; Moon, S. H., Activity and thermal stability of sonochemically synthesized MoS₂ and Ni-promoted MoS₂ catalysts. *Catalysis Today* **2010**, 149, (1-2), 47-51.
119. Yaccato, K.; Carhart, R.; Hagemeyer, A.; Lesik, A.; Strasser, P.; Volpe Jr, A. F.; Turner, H.; Weinberg, H.; Grasselli, R. K.; Brooks, C., Competitive CO and CO₂ methanation over supported noble metal catalysts in high throughput scanning mass spectrometer. *Applied Catalysis A: General* **2005**, 296, (1), 30-48.

120. Dau, H.; Limberg, C.; Reier, T.; Risch, M.; Roggan, S.; Strasser, P., The Mechanism of Water Oxidation: From Electrolysis via Homogeneous to Biological Catalysis. *ChemCatChem* **2010**, 2, (7), 724-761.
121. Chhina, H.; Campbell, S.; Kesler, O., Thermal and electrochemical stability of tungsten carbide catalyst supports. *Journal of Power Sources* **2007**, 164, (2), 431-440.
122. Kulikovskiy, A. A., Thermal stability of the catalyst layer operation in a fuel cell. *Journal of Electroanalytical Chemistry* **2011**, 652, (1-2), 66-70.
123. Xia, B. Y.; Wang, J. N.; Teng, S. J.; Wang, X. X., Durability Improvement of a Pt Catalyst with the Use of a Graphitic Carbon Support. *Chemistry – A European Journal* **2010**, 16, (28), 8268-8274.
124. Sellin, R.; Grolleau, C.; Arrii-Clacens, S.; Pronier, S.; Clacens, J.-M.; Coutanceau, C.; Léger, J.-M., Effects of Temperature and Atmosphere on Carbon-Supported Platinum Fuel Cell Catalysts. *The Journal of Physical Chemistry C* **2009**, 113, (52), 21735-21744.
125. Koh, S.; Hahn, N.; Yu, C.; Strasser, P., Effects of Composition and Annealing Conditions on Catalytic Activities of Dealloyed Pt-Cu Nanoparticle Electrocatalysts for PEMFC. *Journal of The Electrochemical Society* **2008**, 155, (12), B1281-B1288.
126. Hasché, F.; Oezaslan, M.; Strasser, P., In Situ Observation of the Thermally Induced Growth of Platinum-Nanoparticle Catalysts Using High-Temperature X-ray Diffraction. *ChemPhysChem* **2012**, 13, (3), 828-834.
127. Yu, C.; Koh, S.; Leisch, J. E.; Toney, M. F.; Strasser, P., Size and composition distribution dynamics of alloy nanoparticle electrocatalysts probed by anomalous small angle X-ray scattering (ASAXS). *Faraday Discussions* **2009**, 140, 283-296.
128. Tuaeov, X.; Strasser, P., Small angle X-ray scattering (SAXS) techniques for polymer electrolyte membrane fuel cell characterisation. *Woodhead Publishing Series in Energy, London* **2011**, Vol. II - chapter 4 (Eds.: C. Hartnig, C. Roth), in press.
129. Fellingner, T.-P.; Hasché, F.; Strasser, P.; Antonietti, M., Mesoporous Nitrogen-Doped Carbon for the Electrocatalytic Synthesis of Hydrogen Peroxide. *Journal of the American Chemical Society* **2012**, 134, (9), 4072-4075.